Lawrence Berkeley National Laboratory
LBL Publications

Title
Deep Borehole Field Test Research Activities at LBNL:

Permalink
https://escholarship.org/uc/item/2w38r4cs

Authors
Dobson, Patrick
Tsang, Chin-Fu
Kneafsey, Timothy
et al.

Publication Date
2016-08-19

Deep Borehole Field Test Research Activities at LBNL

Fuel Cycle Technology

Patrick Dobson, Chin-Fu Tsang, Timothy Kneafsey, Sharon Borglin, Yvette Piceno, Gary Andersen, Seiji Nakagawa, Kurt Nihei, Jonny Rutqvist, Christine Doughty, Matthew Reagan

Lawrence Berkeley National Laboratory

August 2016

<div align="right">
Revision 2
12/20/2012
</div>

<h1 align="center" style="color:green">APPENDIX E</h1>

<h1 align="center" style="color:green">FCT DOCUMENT COVER SHEET [1]</h1>

Name/Title of Deliverable/Milestone/Revision No.	Deep Borehole Field Test Research Activities at LBNL
Work Package Title and Number	Deep Borehole Field Test – LBNL FT-16LB08030803
Work Package WBS Number	1.02.08.03.08
Responsible Work Package Manager	Jens Birkholzer (signature on file)
	(Name/Signature)

Date Submitted   08/19/2016

Quality Rigor Level for Deliverable/Milestone	☒ QRL-3	☐ QRL-2	QRL-1 ☐ Nuclear Data	☐ Lab/Participant QA Program (no additional FCT QA requirements)

This deliverable was prepared in accordance with   Lawrence Berkeley National Laboratory
_____
(Participant/National Laboratory Name)

QA program which meets the requirements of
☒ DOE Order 414.1   ☐ NQA-1-2000   ☐ Other

This Deliverable was subjected to:

☒ Technical Review   ☐ Peer Review

Technical Review (TR)   **Peer Review (PR)**

Review Documentation Provided   **Review Documentation Provided**

☐ Signed TR Report or,   ☐ Signed PR Report or,

☐ Signed TR Concurrence Sheet or,   ☐ Signed PR Concurrence Sheet or,

☒ Signature of TR Reviewer(s) below   ☐ Signature of PR Reviewer(s) below

Name and Signature of Reviewers

Liange Zheng   (signature on file)   Boris Faybishenko   (signature on file)
_____   _____

Quanlin Zhou   (signature on file)
_____   _____

Kunhwi Kim   (signature on file)
_____   _____

NOTE 1: *Appendix E should be filled out and submitted with the deliverable. Or, if the PICS:NE system permits, completely enter all applicable information in the PICS:NE Deliverable Form. The requirement is to ensure that all applicable information is entered either in the PICS:NE system or by using the FCT Document Cover Sheet.*

NOTE 2: *In some cases there may be a milestone where an item is being fabricated, maintenance is being performed on a facility, or a document is being issued through a formal document control process where it specifically calls out a formal review of the document. In these cases, documentation (e.g., inspection report, maintenance request, work planning package documentation or the documented review of the issued document through the document control process) of the completion of the activity along with the Document Cover Sheet is sufficient to demonstrate achieving the milestone. If QRL 1, 2, or 3 is not assigned, then the Lab/Participant QA Program (no additional FCT QA requirements box must be checked, and the work is understood to be performed, and any deliverable developed, in conformance with the respective National Laboratory/Participant, DOE- or NNSA-approved QA Program.*

SUMMARY

The goal of the U.S. Department of Energy Used Fuel Disposition's (UFD) Deep Borehole Field Test is to drill two 5 km large-diameter boreholes: a characterization borehole with a bottom-hole diameter of 8.5 inches and a field test borehole with a bottom-hole diameter of 17 inches. These boreholes will be used to demonstrate the ability to drill such holes in crystalline rocks, effectively characterize the bedrock repository system using geophysical, geochemical, and hydrological techniques, and emplace and retrieve test waste packages. These studies will be used to test the deep borehole disposal concept, which requires a hydrologically isolated environment characterized by low permeability, stable fluid density, reducing fluid chemistry conditions, and an effective borehole seal.

During FY16, Lawrence Berkeley National Laboratory scientists conducted a number of research studies to support the UFD Deep Borehole Field Test effort. This work included providing supporting data for the Los Alamos National Laboratory geologic framework model for the proposed deep borehole site, conducting an analog study using an extensive suite of geoscience data and samples from a deep (2.5 km) research borehole in Sweden, conducting laboratory experiments and coupled process modeling related to borehole seals, and developing a suite of potential techniques that could be applied to the characterization and monitoring of the deep borehole environment. The results of these studies are presented in this report.

TABLE OF CONTENTS

LIST OF FIGURES

LIST OF TABLES

ACRONYMS

AE	Acoustic Emission
API	American Petroleum Institute
COSC	Collisional Orogeny in the Scandinavian Caledonides
DNA	Deoxyribonucleic Acid
DOE	U.S. Department of Energy
DTS	Distributed Temperature Sensing
FEC	Fluid Electric Conductivity
FFEC	Flowing Fluid Electric Conductivity
GIS	Geographical Information System
GTK	Geological Survey of Finland
HMC	Hydrological-Mechanical-Chemical
ID	Inner Diameter
LANL	Los Alamos National Laboratory
LBNL	Lawrence Berkeley National Laboratory
OTU	Operational Taxonomic Unit
RNA	Ribonucleic Acid
SGR	Spectral Gamma Ray
TH	Thermal-Hydrological
THM	Thermal-Hydrological-Mechanical
THMC	Thermal-Hydrological-Mechanical-Chemical
UC	University of California
UFD	Used Fuel Disposition
URL	Underground Research Laboratory
VSP	Vertical Seismic Profiling
XRF	X-ray Fluorescence

DEEP BOREHOLE FIELD TEST RESEARCH ACTIVITIES AT LBNL

1.   INTRODUCTION

Lawrence Berkeley National Laboratory's research contributions to the deep borehole field test project consist of a broad scope of activities. **Section 2** of this report describes the contributions made by our team to assist Los Alamos National Laboratory in collecting relevant subsurface geoscience data that could be used to create a geologic framework model for the deep characterization borehole once a site had been selected and finalized.

Section 3 describes our work with members of the science team of the "Collisional Orogeny in the Scandinavian Caledonides" (COSC) project, which drilled and characterized a 2.5 km scientific borehole (COSC-1) in central Sweden, to obtain key insights on deep borehole characterization techniques. We were able to obtain hydraulic characterization data from flowing fluid electric conductivity (FFEC) logs that were repeatedly run in this well, along with fluid and core samples. Detailed modeling of the FFEC logging data was performed to estimate fracture transmissivities, inflow water salinities, and the hydraulic heads of each inflow zone. Laboratory testing of fractured core samples associated with flow zones identified with the FFEC logging was performed to see how measured fracture permeability values compared with those obtained from the FFEC modeling results. We also conducted geochemical analyses of downhole water samples as well as characterization of the microbiological communities found at different depths, with the goal to see if distinct biologic and geochemical zones might suggest hydraulic isolation of the deep borehole environment.

Section 4 summarizes the FY16 modeling results associated with borehole seals. This work reviews field observations on stress and permeability at depth and observations of damaged and disturbed zone around tunnels and boreholes, followed by initial thermal-hydrological (TH) modeling of deep borehole disposal focusing on thermally driven fluid pressurization and potential upflow along an assumed disturbed zone. This section also describes modeling plans for FY17, which will include Thermal-Hydrological-Mechanical (THM) and Thermal-Hydrological-Mechanical-Chemical (THMC) analysis of the deep borehole system, with a focus on the performance of seals and plugs within the borehole.

Section 5 describes an investigation of borehole seal integrity through designing and conducting preliminary laboratory borehole breakout experiments under high stress (>100 MPa). During FY16, the LBNL team developed experimental setups for examining the impact of drilling-induced damage (borehole breakout) around a deep borehole within a crystalline rock in the laboratory. Because the uniform and homogeneous, ultra-fine-grain rock (novaculite) that was selected for the laboratory experiment exhibited extremely high compressive strength, we have not successfully induced breakout in our samples thus far, even after heating the sample. Three possible follow-up experiments in FY17 currently under consideration include: (1) reducing the rock strength further by introducing water into the thermally induced microcracks, (2) increasing the maximum principal stress (around the borehole) by using the Z-axis loading frame in that direction, and (3) using the block sample to conduct the experiment.

Section 6 describes potential techniques that could be applied to the characterization of the deep borehole environment. The focus in FY16 was on the near-well geophysical detection and

characterization of fractures using a variety of techniques, including vertical seismic profiling (VSP), single well seismic imaging, and near-field dynamic strain sensing. Another approach that will be developed in FY17 is the LBNL deep borehole multilevel characterization system, which would include fluid flow testing, *in situ* pressure and temperature measurements, integrated fiber optics for VSP and Distributed Temperature Sensing (DTS) measurements, and a U-tube fluid sampler for tracer testing and geochemical sampling.

2.   LBNL DEVELOPMENT OF GEOLOGIC FRAMEWORK MODEL SUPPORT

2.1   Introduction

During FY16, LBNL played a supporting role to LANL's effort to develop a 3D geologic framework model for the site selected for the deep characterization borehole. There are several components to this task that the LBNL team originally envisioned contributing to during FY16, provided that a site was selected and finalized:

- **Selection of a geologic modeling tool**. Three different geologic modeling packages were considered and tested by LANL - Jewel Suite, Rockworks, and Leapfrog. Selection of the Rockworks package by LANL was based on software capabilities to capture key geologic features using map, geophysical, and borehole data, compatibility with THMC modeling systems that will use the geologic model, and cost.
- **Development of a 3D geologic model** using the selected software through evaluation of geologic data sets identified by the selected site consortium. Key geologic inputs for the geologic model include the stratigraphy and structures (e.g., faults, fractures, and folds) of the selected area, with a focus on the depth to the crystalline basement, rock mineralogy and textures, identification of aquifers and permeable zones, regional stress regime, physical rock properties, and the degree of heterogeneity within rock units. Once incorporated within a Geographical Information System (GIS) database (e.g., Perry et al. 2015) and geologic framework model, the data were to be reviewed and used to extract key inputs for THMC modeling efforts.
- **Selection of THMC simulator(s)** based on desired modeling capabilities and compatibility with geologic modeling tool. Using input from geologic model, develop THMC model that captures *in situ* conditions of selected site. Coupled process modeling can be used to constrain borehole stability (based on rock properties and stress regime), expected thermal gradient, and the degree of hydraulic isolation of the crystalline basement section. (For FY16, this topic was to be about the selection of simulator, not the actual model development).
- **Provide guidance for drilling** based on results of geologic framework model

In January of 2016, DOE announced that a Battelle Memorial Institute-led team was selected to drill a deep (5 km) characterization borehole into a crystalline basement rock formation in Pierce County, North Dakota, near the town of Rugby. However, this team encountered local opposition to their project. Another attempt was made by the Battelle group to relocate the project to a geologically similar site in Spink County, South Dakota. This site also met with local opposition (Kelley 2016), so DOE is currently considering issuing a new request for proposal for the deep borehole project. Due to the lack of an actual site, the LBNL team had only a modest level of effort during FY16 in support of LANL's development of an actual 3D geologic model. The section below describes some of the work that LBNL did in support of this effort. More details on other aspects of this project that were conducted by the LANL team will be presented in Milestone: M4FT-16LA080308021, Geologic Site Model for Deep Borehole Field Test.

2.2   LBNL Contributions to the LANL Geologic Framework Model Effort

LBNL's participation in this effort during FY16 focused on identifying and obtaining relevant geologic once the deep characterization borehole site was announced. When the site near Rugby, ND was initially selected, our team started looking for nearby deep well data that could help constrain the geology of this region. Web searches resulted in finding relevant data on the North Dakota Department of Mineral Resources and the North Dakota Geological Survey websites. We were able to obtain American Petroleum Institute (API) numbers for all of the wells near the target area, and found stratigraphic

summaries for a number of wells on the site map provided by LANL (Figure 2.2.1), including one deep well (632 - API 33-005-00004) located about 20 km east of the proposed site that encountered granite at a depth of 5142 feet (Carlson, 1955b). We found a number of reports that contain detailed stratigraphic information on wells in the vicinity of the proposed site, including wells 557 (API 33-069-00006) (Carlson 1955a), 538 (API 33-069-00005) (Carlson 1955c), and 149 (API#33-069-00010) (Hansen, 1956). Hansen (1958) provided a regional stratigraphic overview of North Dakota, with a focus on the Jurassic-Cretaceous boundary (Figure 2.2.2). A study of the geology of Pierce County (Carlson and Freers 1975), where the proposed well site is located, shows that the contact with the Precambrian basement rocks in this area is located at a depth of around 5500 feet (Figure 2.2.3), thus complying with the requirement for the deep borehole project that the basement depths be less than 2 km from the surface. Deep wells throughout the state were used by Heck (1988) to create a Precambrian basement map for North Dakota (Figure 2.2.4).
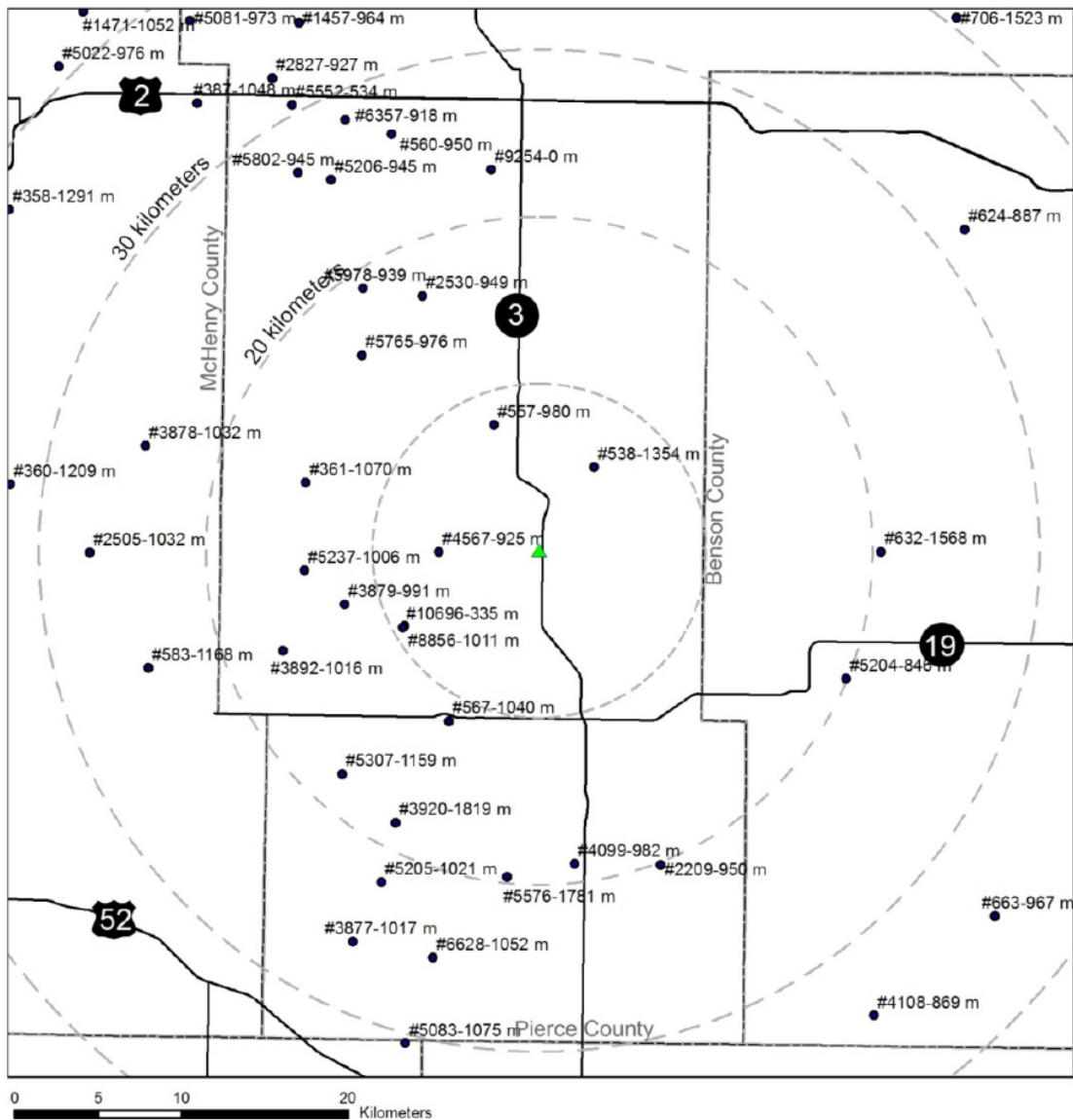
Figure 2.2.1. Location map of the proposed deep characterization borehole in Pierce County, ND. Dots indicate locations of oil and gas wells, with well numbers and total depths. Dashed lines indicate radial distance away from the proposed site.
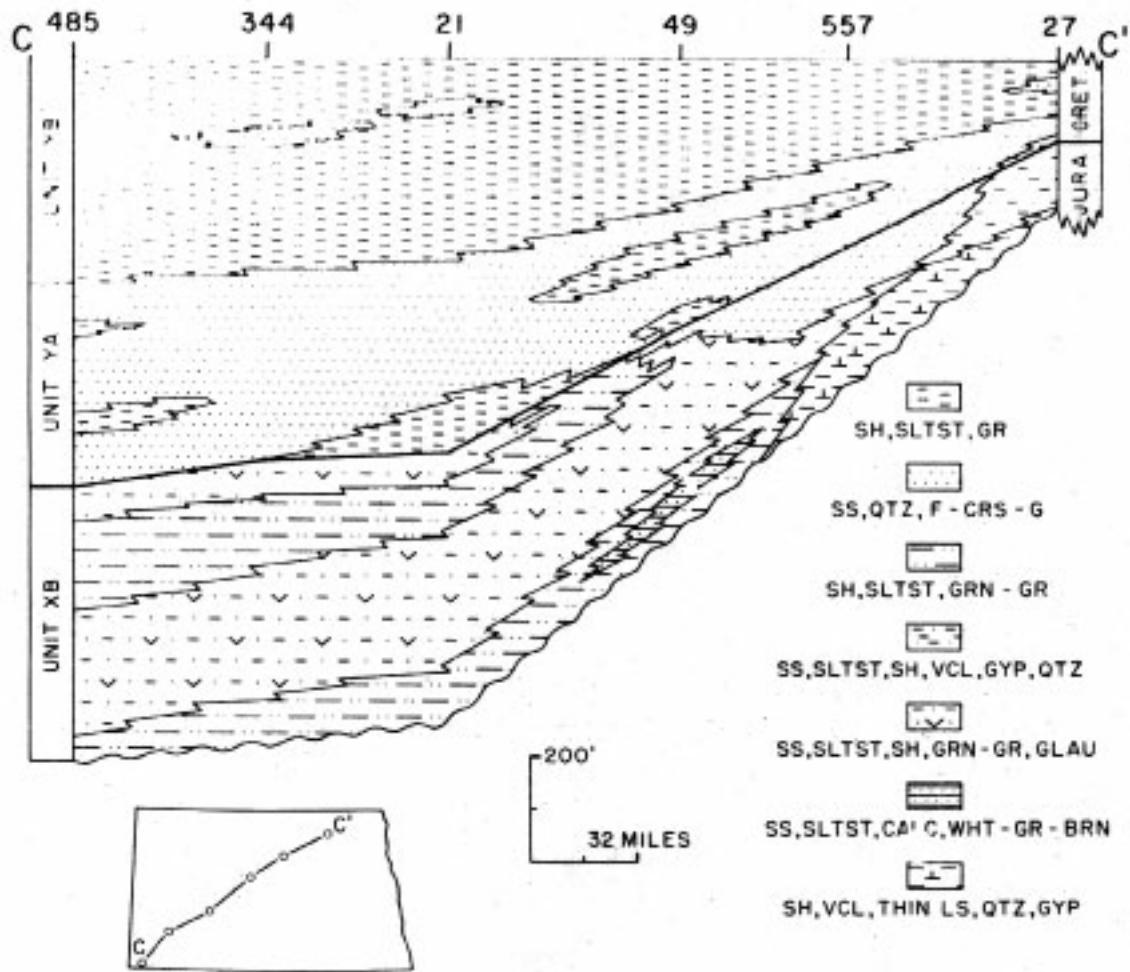
Figure 2.2.2. NE-SW regional cross section depicting the Jurassic-Cretaceous boundary. Well 557 is located just north of the proposed deep characterization borehole site near Rugby. The Jurassic unit (Unit XB) in NE North Dakota consists of nonmarine sediments such as shales, siltstones, thin limestones, and very fine-grained, calcareous sandstones (Hansen 1958).
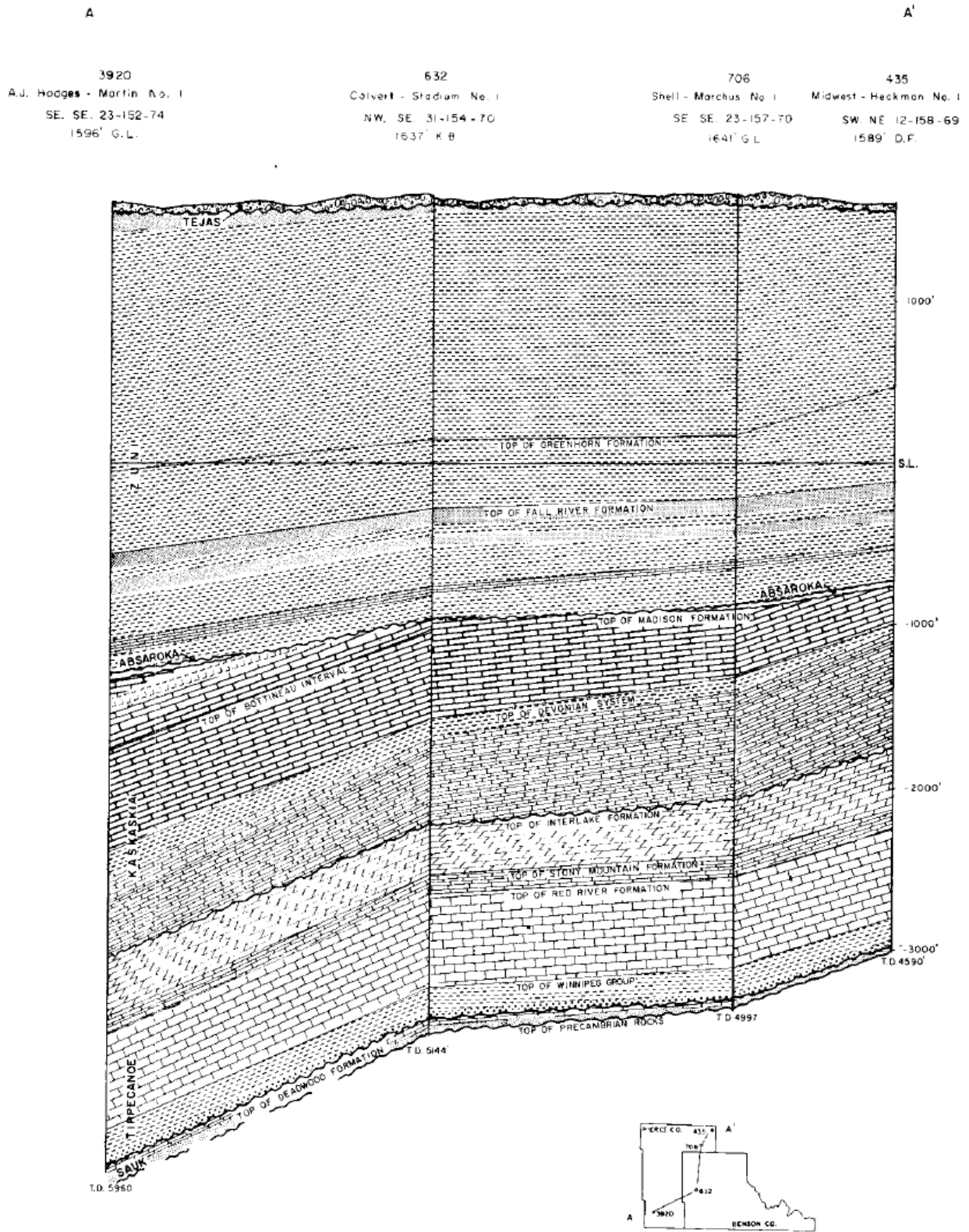
Figure 2.2.3. Subsurface stratigraphy of Pierce and Benson counties based on well logs from four deep wells (Carlson and Freers, 1975). The depth to the Precambrian basement varies from around 4600 feet to the NE down to about 5950 feet to the southwest.
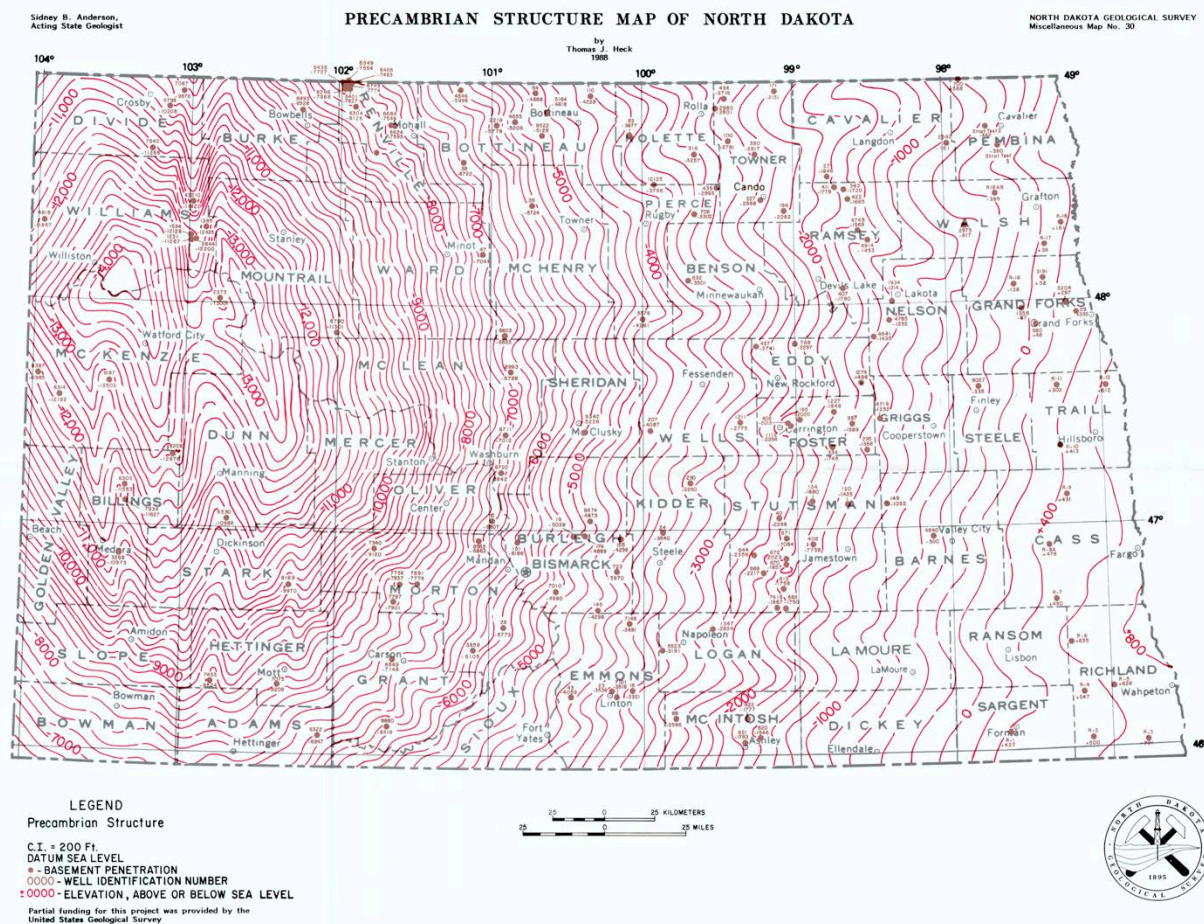
Figure 2.2.4 Precambrian structure map for North Dakota, with contours depicting the top of the crystalline basement relative to sea level in feet (Heck, 1988). The prospective deep borehole characterization site is located in Pierce County south of Rugby. Red dots mark well control points.

Our group also identified GIS data available from the North Dakota Geological Survey for various Cretaceous-aged units, such as the Inyan Kara, Mowry, and Greenhorn Formations (Anderson and Juenker 2006a,b; 2007) – these data could be used to populate the LANL GIS and geologic framework models for this area (Perry and Kelley 2016).

Our team also looked into the availability of spec seismic data for the region. We found that there is a 2D E/W line (SRB-9) located 6 miles to the north, between state route 3 and state route 30, as well as several N/S lines (SRD-14A and SRD-17) on the same interval that end about 6 miles north of the target. All of these seismic datasets are 1980s vintage with vibroseis and explosive sources: ~24 fold for the vibe, 8 fold for the dynamite. We passed all of this information along to the LANL team.

Shortly after identifying all of this information for the Rugby site, we were notified by DOE that due to local opposition to the project, North Dakota would no longer be considered as a prospective site for this project. As a result, we suspended our work on this part of the project for the remainder of FY16.

2.3   Future Activities for FY17

Our team is currently awaiting the selection of a new site by DOE for the deep characterization borehole field test. Once a site has been selected and wins local acceptance by the community where it will be located, our group at LBNL will continue to provide technical assistance to the LANL team, which is leading the geologic framework model development for the deep borehole project.

2.4   References

Anderson, F.J., and Juenker, B.J. (2006a) Preliminary Structure Contour Map on top of the Cretaceous Greenhorn Formation in North Dakota, North Dakota Geological Survey Geologic Investigations 31.

Anderson, F.J., and Juenker, B.J. (2006b) Preliminary Structure Contour Map on top of the Cretaceous Mowry Formation in North Dakota, North Dakota Geological Survey Geologic Investigations 37.

Anderson, F.J., and Juenker, B.J. (2007) Preliminary Structure Contour Map on top of the Cretaceous Inyan Kara Formation in North Dakota, North Dakota Geological Survey Geologic Investigations 38.

Carlson, C. (1955a) A Summary of the J. P. Owens - Rosie Schann #1, Pierce County, North Dakota, North Dakota Geological Survey Circular No. 116.

Carlson, C. (1955b) Summary of the Calvert Exploration Co. - National Bulk Carriers - Stadum #1, Benson County, North Dakota, North Dakota Geological Survey Circular No. 119.

Carlson, C. (1955c) Summary of the Calvert Exploration Co. - Cyrus & Joseph Ranberg #1, Pierce County, North Dakota, North Dakota Geological Survey Circular No. 123.

Carlson, C.G., and Freers TF (1975) Geology of Benson and Pierce Counties, North Dakota. North Dakota Geological Survey Bulletin 59, Part 1, and North Dakota State Water Commission County Ground Water Studies 18, Part 1, 32 p.

Hansen, D.E. (1956) Summary of the Shell Oil Company Gifford Marchus No. 1. North Dakota Geological Survey Circular No. 149.

Hansen, D.E. (1958) The Jurassic-Cretaceous boundary in North Dakota. Second Williston Basin Symposium, 47-54.

Heck, T.J. (1988) Precambrian structure map for North Dakota. North Dakota Geological Survey Miscellaneous Map No. 30.

Kelley, M. (2016) Observations from the first year of the deep borehole field test. Geological Society of America *Abstracts with Programs.* Vol. 48, No. 7, doi: 10.1130/abs/2016AM-285771

Perry, F.V., Arnold, B.W., and Kelley, R.E. (2015) A GIS database to support siting of a deep borehole field test. International High-Level Radioactive Waste Management Conference, Charleston, SC, April 12-16, 2015, American Nuclear Society, 632-637.

Perry, F., and Kelley, R.E. (2016) Use of GIS and geologic framework models to support site evaluation and site characterization for a deep borehole field test in crystalline rock. Geological Society of America *Abstracts with Programs.* Vol. 48, No. 7 doi: 10.1130/abs/2016AM-280690

3.   SWEDISH BOREHOLE ANALOG STUDY

3.1   Introduction/Overview

The "Collisional Orogeny in the Scandinavian Caledonides" (COSC) project is a scientific deep drilling project in Sweden whose objective is to gain insights into the tectonic evolution of the area, characterize present and past deep fluid circulation patterns, determine current heat flow to constrain climate modeling, and characterize the deep biosphere. Another objective of this project is to calibrate high quality surface geophysics through deep drilling. The project is centered on the drilling of two deep boreholes (each to depth of ~2.5 km) into crystalline rock in Sweden.

The first hole (COSC-1) was completed on August 26, 2014 to a depth of 2495.8 m: core recovery was greater than 99%. The COSC-1 borehole was drilled though the Seve Nappe, which contains high grade metamorphic rocks indicative of deep (100 km) crustal levels (Figure 3.1.1). The main lithologies encountered consist of felsic, amphibolite, and calc-silicate gneisses, amphibolite, migmatites, garnet mica schist, with discrete zones of mylonite and microkarst. There is a transition from gneiss into lower grade metasedimentary rocks that occurs between 2345 and 2360 m, which likely marks a structural boundary between different nappes. In addition to drilling the well and collecting core, the research team also conducted pre-drilling and post-drilling seismic and other geophysical surveys, borehole geophysical logs, conducted on-site measurement on recovered cores, carried out systematic X-ray fluorescence (XRF) measurement on all cores at 10 cm intervals for key chemical compositions, and performed downhole spectral gamma ray (SGR) logging to determine U, Th and K contents all along the borehole. Lorenz et al. (2015a,b) summarize the early results of this project.
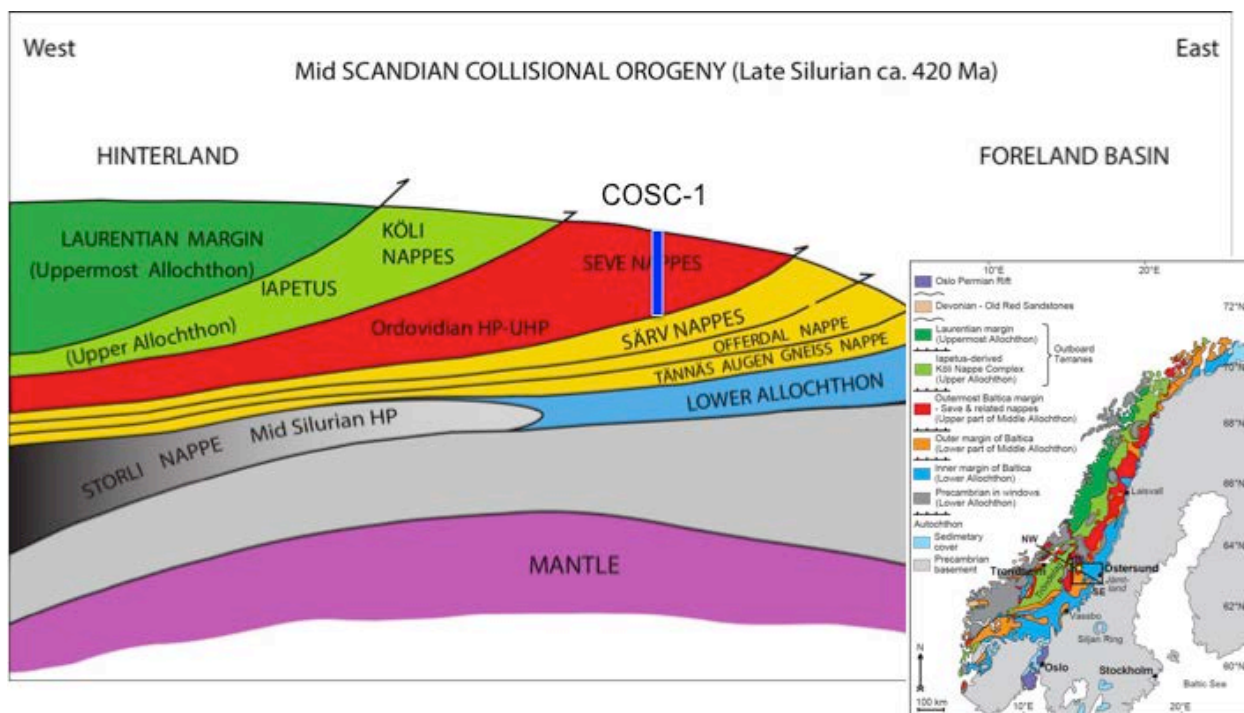
Figure 3.1.1. Location of COSC-1 deep borehole (Gee et al. 2013; Lorenz et al. 2015a)

LBNL became aware of the COSC project through Dr. Chin-Fu Tsang, who worked for many years in the Earth Sciences Division at LBNL and was active in the DOE's nuclear waste program from the Stripa project in Sweden to the Yucca Mountain Project in Nevada. Chin-Fu is currently affiliated with LBNL

Energy Geosciences Division as an LBNL Senior Scientist Emeritus, and he is currently a Visiting Professor at the Department of Earth Sciences at Uppsala University in Sweden. He serves as the Principal Investigator for Hydrogeology in the COSC project.

One of Chin-Fu's main activities for the COSC project was to run the flowing fluid electrical conductivity (FFEC) log, which had previously been developed at LBNL (Tsang and Doughty, 2003). The FFEC logs can be used to identify locations of hydraulically active zones at decimeter (10-cm) resolution in the borehole.

The main objective of this project is analyze and understand data from the COSC-1 borehole as a case study for deep borehole characterization, with the goal to develop a better understanding of what information can be obtained from core and borehole measurements and what is the deep subsurface environment in granitic and other crystalline rocks in the context of nuclear waste disposal. This consists of the following activities:

(a) Support additional field testing at the COSC-1 site to obtain more FFEC logging results and also collect formation fluid samples from hydraulically active zones that have been previously identified in the borehole.
(b) Conduct laboratory tests at LBNL on selected COSC-1 cores and downhole water samples.
(c) Analyze and integrate fluid logging data, laboratory data, together with other COSC-1 project data to arrive at an understanding and evaluation of the deep borehole environment in the context of nuclear waste disposal.

The LBNL team met with members of the COSC project team at LBNL in December 2015. A summary of this informal workshop is included as Appendix A.

This section of the deep borehole report summarizes the work that has been conducted at LBNL and our collaborators from the COSC project during FY16. The main activities include FFEC logging and modeling, hydraulic characterization of core samples, downhole water sampling and geochemical analysis, and microbial characterization of water samples. The motivation for these studies was to address how to determine whether or not the deep borehole environment was hydraulically isolated. Tests to identify and characterize flow zones within the COSC-1 well, and to determine whether or not the deep zones of the borehole were chemically and biologically distinct from shallow aquifers could help provide insights on how to design appropriate hydrologic characterization tests for the DOE deep borehole project.

3.2 FFEC logging

Flowing Fluid Electric Conductivity (FFEC) logging is a technique that uses contrasts in wellbore and formation fluid salinities to identify permeable inflow zones in a wellbore. To run the test, the borehole is first flushed with a low salinity fluid, the hydraulic head is lowered by pumping to induce inward fluid flow from the formation along permeable fractures, and a conductivity log is run into the borehole to detect zones with increased conductivity. Runs conducted using different drawdowns and at different times can be used to determine not only where the permeable inflow zones are located, but also estimate inflow salinities and transmissivities using the relation:

$$A = q \times C \times \Delta t$$

where A is the area under the conductivity curve for a particular inflow zone, q is the inflow rate for that zone, C is the salinity of the inflow water, and Δt is the elapsed time since the start of the inflow into the

borehole. More details on this can be found in Section 3.3 and in Tsang and Doughty (2003). An illustration of this process can be seen in Figure 3.2.1.
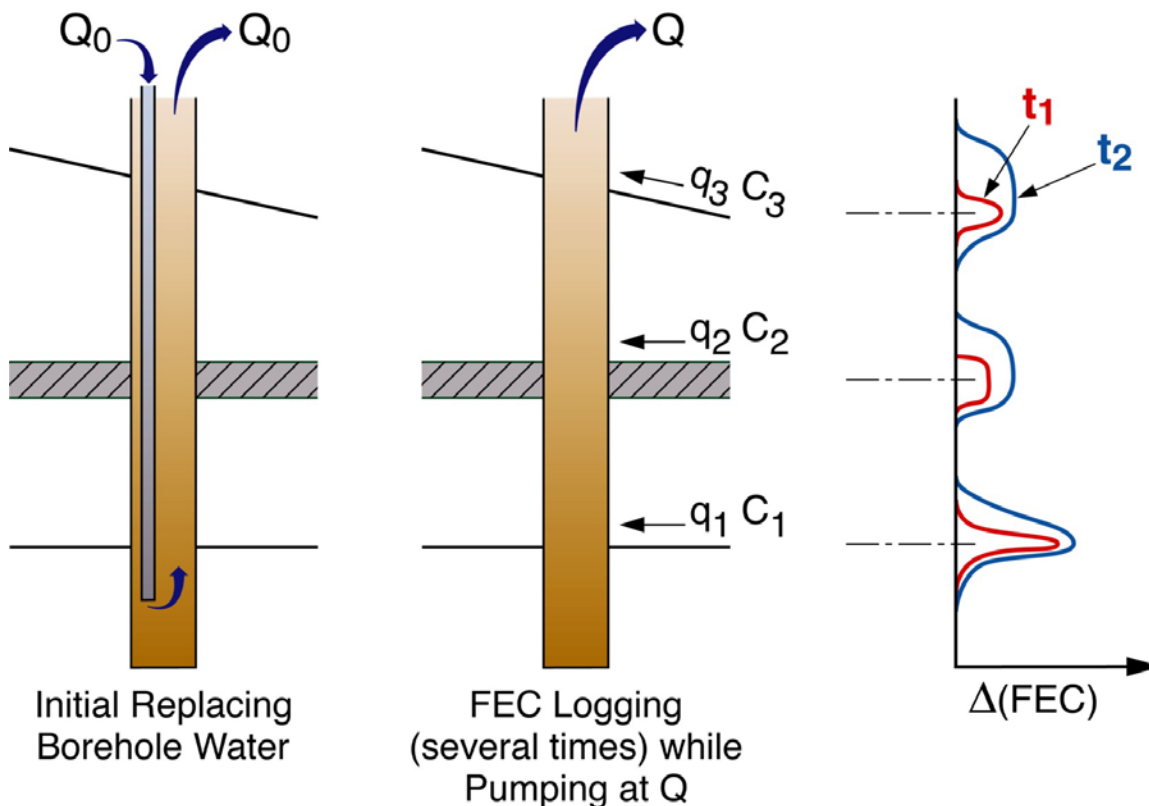
Figure 3.2.1. Schematic for FFEC logging method. Borehole is first flushed with low-salinity fluid, water level of well is lowered to induce flow into borehole along permeable fractures, and conductivity log is run to identify regions with increased salinity corresponding to inflow zones. Q represents the pump flow rate, Δ(FEC) is the change in electrical conductivity at time intervals t, q is the inflow rate and C is the salinity of the formation water associated with each flow zone (Tsang et al. 2016).

A series of FFEC logs were run in 2014 during and shortly following drilling, and again in 2015 (Tsang et al. 2016). For the initial suite of tests, these logging runs took advantage of the day off from drilling to flush the well, then run an electrical conductivity tool in the well to detect inflow zones that had contrasts in fluid salinity from the wellbore fluid. The 2014 tests ranged in duration from 8 hours to a day, and had well drawdowns varying from 33 to 70 m. During this first suite of FFEC logs, a total of eight inflow zones were identified in the COSC-1 borehole, with depths of 339, 507, 554, 696, 1214, 1245, 2300, and 2380 m (Tsang et al. 2016) (Figure 3.2.2). These inflow zones can be directly correlated with open fractures identified in the core samples (Figure 3.2.3). The evaluation of selected fractured core intervals is presented in Section 3.4.
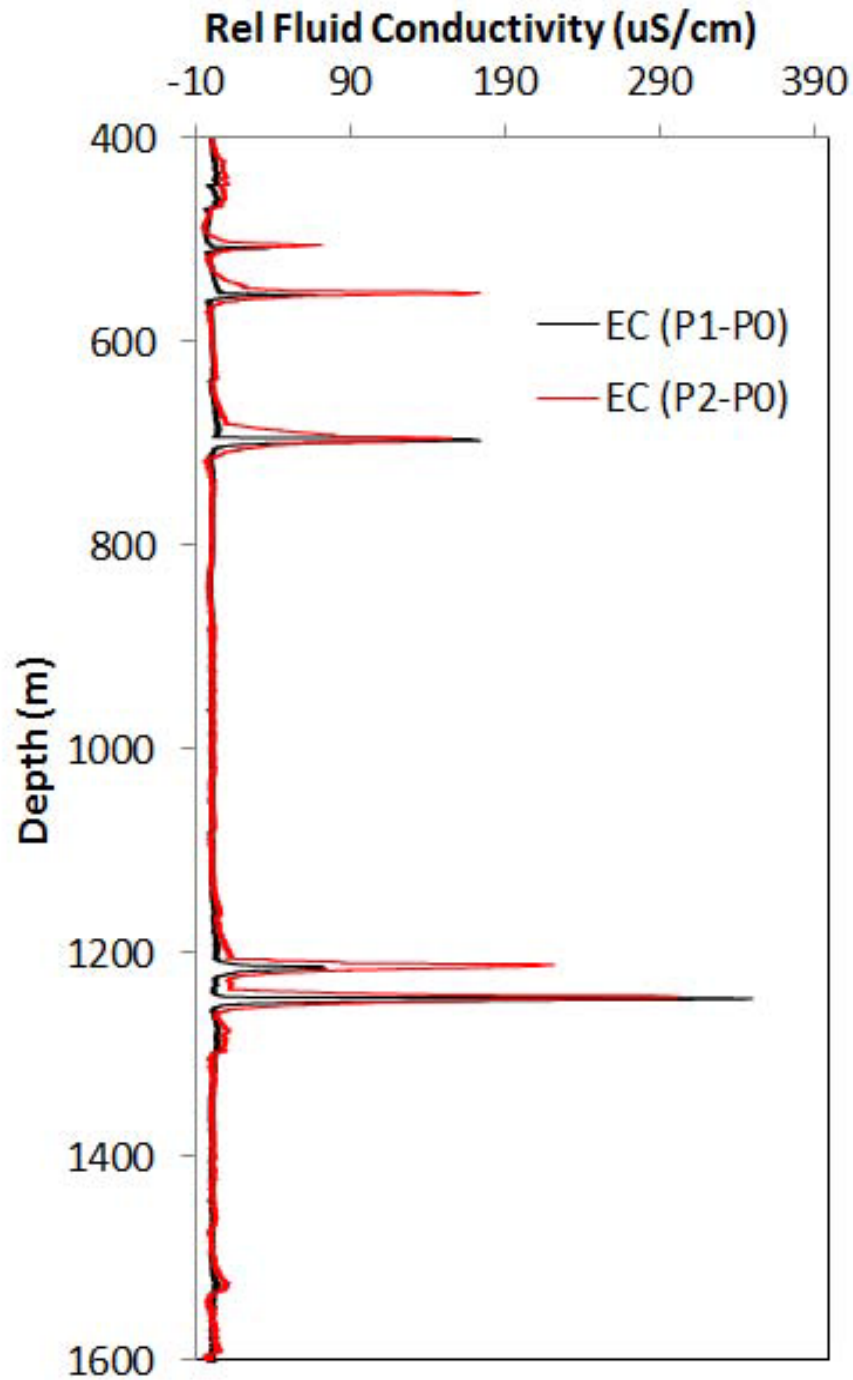
Figure 3.2.2. Examples of FFEC logging results from the COSC-1 conducted in 2014. The two curves indicate profiles P1 and P2 obtained during pumping after the background profile P0 has been subtracted (Tsang et al. 2016).
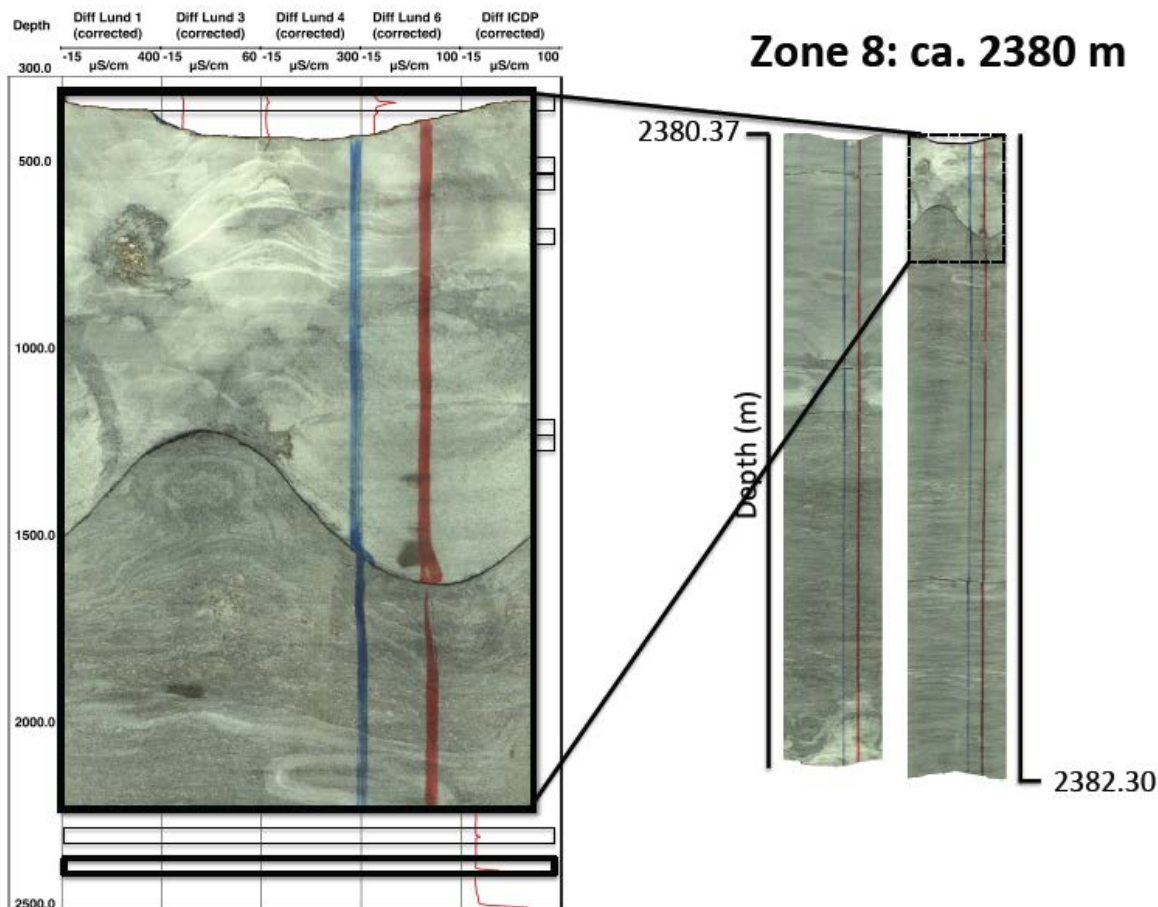
Figure 3.2.3. Open fracture in COSC-1 core that corresponds to fluid inflow zone identified by FFEC logging at 2380 m depth.

The logging runs conducted in 2015 encountered some difficulties in replacing the wellbore fluid, so the borehole background FEC remained high. Two pumping rates resulted in different drawdowns; the first was -50 m (3 logs taken), and the second had -10 m drawdown (10 logs taken). The low drawdown from the second test resulted in minimal fracture fluid flow, as most of the fractures have negative head. From these logs, the depth of hydraulically active fractures can be determined, as well as their transmissivity, fluid salinity, and initial pressure head. More details on the logging results can be found in Tsang et al. (2016); modeling and interpretation of these results are presented in Section 3.3.

3.3   Modeling of FFEC logging

3.3.1   Introduction

To understand the hydrogeology of the deep subsurface, information is required on the spatial distribution (locations and extent) of hydraulically conductive zones, their hydraulic transmissivities, as well as their hydraulic heads, temperature, and water salinity or other chemical characteristics. These flow zones often arise from hydraulically conductive fractures or faults. Direct data on these conductive fractures can be obtained through downhole tests in deep boreholes. For example, fluid production or injection tests can be conducted at selected depths in the borehole bracketed by two packers and in these bracketed intervals fluid samples can also be collected. Such tests are time-consuming, so they are mainly carried out after drilling is completed. Additionally, the depths of potential hydraulically conductive zones, especially zones with low transmissivities, are often not known a priority, making optimal packer placement

difficult. Borehole televiewer logging can show fractures intercepted by the borehole. However the majority of these fractures are usually not hydraulically conductive. For example, at the Laxemar and Forsmark sites in Sweden, detailed fracture investigations were conducted on cores from several tens of boreholes down to over 1000 m, and it was found that only about 10% of the nearly 100,000 fractures inspected were characterized as open or partly open and then only 2-3% of all fractures had measurable transmissivity (Rhén et al. 2008, Follin 2008; Follin et al. 2014).

One of the very effective ways to specifically study hydraulically conductive fractures intercepted by a borehole is the FFEC logging method (Tsang et al. 1990; Tsang and Doughty 2003; Doughty and Tsang 2005; West and Odling 2007; Doughty et al. 2013; Moir et al. 2014), illustrated schematically in Figure 3.3.1. The method, which will be described in more detail in the next section, is based on firstly replacing borehole water by fresh water or water with salinity distinctly different from that of the formation water. Then, with the borehole pumped at a low flow rate, the change in salinity or electric conductivity of borehole water as a function of depth is measured with a moving electric conductivity/temperature (EC/T) probe. Profiles of fluid electric conductivity (FEC) versus depth at different times after the start of pumping can be analyzed to obtain the depths of conducting fractures, their transmissivity, salinity or FEC of the fracture water, and the hydraulic heads in these fractures. Typically the logging is done over a period of several days or a week in an existing borehole, i.e., after the borehole drilling is finished.
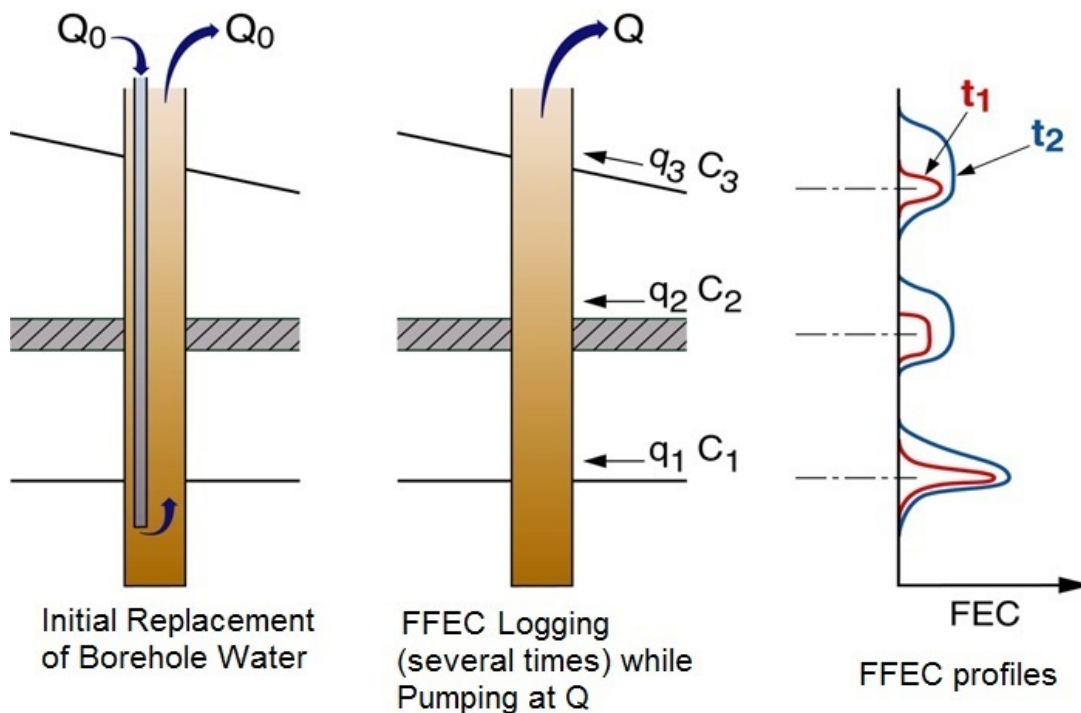
Figure 3.3.1. Schematic of FFEC logging.

Tsang et al. (2016) proposed the use of FFEC logging during the drilling of a deep borehole without first replacing borehole water with fresh water. This is based on two factors. First, the drilling fluid used can have very low electric conductivity, not much higher than that of fresh water. Second, the normal drilling schedule often includes breaks, where one day per week is used for the drill crew to rest or for other operational needs. Further, an EC/T probe and a downhole pump are normal equipment available on a drill site for monitoring drilling fluid. Thus, FFEC logging can be done in the one-day breaks with minimum extra trouble and with no impact on drilling schedule. This provides a new approach to hydraulic testing during drilling. Tsang et al. (2016) demonstrated that this can be done by applying the

method to the drilling of the 2500-m COSC-1 borehole at Åre, Sweden as part of the Swedish Deep Drilling Program (Gee et al. 2010; Lorenz et al. 2015). The COSC-1 borehole was drilled though the Seve Nappe, which contains low permeability, high grade metamorphic rocks (mostly felsic gneisses) indicative of deep (100 km) crustal levels. HQ core was collected from 102 m to 1616 m, and NQ core was obtained from 1616 m to the bottom hole depth of 2496 m; core recovery was excellent. Based on test data from a one-day break during the four months of drilling, referred to as Test 1 below, Tsang et al. (2016) were able to identify six hydraulically conductive fractures between the depths of 300 and 1600 m and estimate their transmissivity and water salinity or FEC. These hydraulically conductive zones correspond to open fractures observed in the recovered core samples.

The focus of Tsang et al. (2016) is on introducing the concept of using FFEC logging for hydraulic testing during drilling and on demonstrating by a practical case that important and useful hydrologic information can be obtained. Subsequent to the one-day test during drilling (Test 1) and its data analysis as reported in Tsang et al. (2016), an additional one-day FFEC logging (Test 2) was conducted a week after drilling was completed, using a different pumping rate and water-level drawdown. This enables the estimation of the hydraulic head of each of the conducting fractures (Tsang and Doughty 2003). The fracture hydraulic heads are very useful information to understand the hydraulic structure and condition of the deep subsurface. The present paper includes a description of both Test 1 and Test 2, re-analysis of Test 1 data independently of earlier analysis, analysis of Test 2 data, and a joint analysis of Test 1 and Test 2 data to calculate the hydraulic heads of all the conductive fractures identified in the borehole. Two confirmatory FFEC logging tests, Test 3 and Test 4, were performed about one year after the borehole was drilled. These were also analyzed to supplement and confirm results from Test 1 and Test 2 and constrain the uncertainty ranges of the estimated parameters. Furthermore, since all these tests did not include the initial step of borehole water replacement (Figure 3.3.1), the impact of baseline salinity in the borehole on data analysis is also discussed, including the usefulness of FFEC logging under such conditions to constrain estimates of the salinity of conductive zones.

This report is organized as follows. In the next subsection, the FFEC logging method is described, together with analysis methods that have been developed for obtaining hydrologic parameters from the logging data. This is followed by a discussion of the impact on data analysis of baseline salinity in the borehole, which may vary because borehole water was not replaced by fresh water during this series of FFEC logging tests. The following subsections present the application of the FFEC method to two one-day tests (Test 1 and Test 2) conducted during and shortly after the four-month drilling period of the 2500-m COSC-1 borehole. Two subsequent tests (Test 3 and Test 4), conducted about one year after drilling, are then described and analyzed. After presenting the results from the analyses of the four tests, the paper concludes by discussing the issues that arise from conducting FFEC logging during drilling.

3.3.2   The FFEC Logging and Data Analysis Methods

In the FFEC logging method proposed by Tsang et al. (1990), the wellbore water is first replaced by water of a constant salinity significantly different from that of the formation water. This may be accomplished by injecting water with a salinity distinct from that of the formation water, such as municipal tap water, low TDS water from a river or shallow water well, or de-ionized water, through a tube to the bottom of the wellbore at a constant low rate, while simultaneously pumping from near the top of the well at the same rate. In this way, the wellbore water is replaced by injected water without a large change in wellbore hydraulic head, so that neither is the injected water pushed out into the formation nor is the formation water drawn into the well. The fluid electric conductivity (FEC) of the effluent is monitored at the wellhead until a low, stable FEC value is reached, which typically takes about half a day or overnight for a deep (1-2 km) well.

If the final stable effluent FEC is substantially different from the FEC of the injected replacement water, it indicates that native fluid has entered the wellbore during the borehole water replacement phase. This may occur because wellbore hydraulic head could have unintentionally dropped during borehole water replacement, or if natural regional groundwater flow is intercepted by the well. It can also occur if different hydraulically conductive features intercepted by the wellbore have different hydraulic heads, which sets up an internal wellbore flow, with formation water entering the wellbore through the features with higher hydraulic head and borehole water exiting to the formation through features with lower hydraulic head.

After the wellbore water is replaced by water of salinity distinct from that of the formation water, a baseline FEC profile is collected by moving an electric conductivity- temperature (EC/T) probe up and down the wellbore. Then the well is pumped at a constant rate and formation water enters the wellbore and mixes with wellbore water at the inflow depths. FFEC profiles are measured along the wellbore at a series of times after the start of pumping (Figure 3.3.1). The pump and a pressure sensor are emplaced at the shallow part of the well below the anticipated drawdown of the water table. The FFEC profiles thus obtained will display higher-salinity peaks in FEC values at depths where water enters into the well. The peaks will spread around the inflow points in the wellbore because of the moving probe and solute diffusion. However such spreading is typically of the order of the borehole diameter (which is 9.6 cm from 103 to 1616 m and 7.6 cm from 1616 m to TD in the COSC-1 well) and hence the position of the inflow zones can be determined with accuracy of the order of 10 cm.

The height of each peak at any time depends on the product qC, where q is the inflow rate and C is the salinity of the formation water, from the particular flow zone. Here C can be expressed in NaCl ionic concentration in g/L, or in terms of its fluid electric conductivity (FEC) with units of μS/cm. In the FEC profile, the peaks are skewed in the direction of water flow at their locations in the borehole. The degree of skewness is dependent on the local vertical flow rate along the borehole, which is the sum of all inflow rates for feed points located below that point. Hence when a peak grows and shows skewing, it is possible to infer q and C independently, but for early times or small flow rates, when the peak grows symmetrically, only the product qC can be determined.

A convenient method for determining the qC product is the so-called Mass Integral Analysis, wherein the area under each peak is calculated as a function of time, with the slope of the resulting line giving qC (Doughty et al. 2008).

A simple code BORE II (Doughty and Tsang 2000) has been developed to solve the one-dimensional advection-dispersion equation for flow up the wellbore, with sources and sinks used to represent inflow and outflow zones. Matching the FEC profiles calculated by BORE II to the profiles collected in the field involves choosing values of q and C for each peak by trial and error until an acceptable match to all the FFEC profiles is obtained. The parameter to describe vertical "dispersion" (the sum of diffusion and mixing due to probe movement) along the wellbore is also adjusted to obtain the best fit.

The inflow rates q and the water-level drawdown h_D (a positive number) in the borehole due to the constant-rate pumping during logging may be used in the Thiem (1906) equation to calculate the transmissivity values T of the inflow zones. For each inflow zone

$$q = \frac{2\pi T}{\ln\left(\frac{r_{out}}{r_{wb}}\right)}(h + h_D) \qquad (3.3.2.1)$$

where r_{wb} is well bore radius, r_{out} is an assumed outer radius where the pressure response to pumping drops to zero, and h is the hydraulic head of the inflow zone with reference to the initial hydraulic head of the wellbore with no pumping (i.e., the average hydraulic head of all flow zones intercepting the borehole). If the hydraulic heads of all the flow zones intersecting the borehole are assumed to be equal, then they are simply equal to the initial hydraulic head in the borehole, and $h = 0$ in Equation (3.3.2.1). Under these conditions, T for each inflow zone can be determined from Equation (3.3.2.1) using the q for that inflow zone obtained by fitting FFEC profiles from a single test. Note that the method does not require a specialized probe, but just a typical EC/T probe, a pressure sensor, and a downhole pump, all generally available at a drill site.

If the logging procedure is repeated using one (or two) more higher or lower pumping rates at the top of the well, Multi-Rate Analysis of the data yields the hydraulic heads h of the flow zones at the different depths, which could be different from one another (Tsang and Doughty 2003). Let us assume that two pumping rates are used with two water-level drawdown values h_{D1} and h_{D2} (positive numbers), and separate analyses of the FFEC logs give inflow rates q_1 and q_2 respectively, for an inflow zone at a particular depth with a hydraulic head h.

Subtracting Equation (3.3.2.1) for the first test from Equation (3.3.2.1) for the second test and solving for T yield

$$T = \frac{(q_1 - q_2)\ln\left(\frac{r_{out}}{r_{wb}}\right)}{(h_{D1} - h_{D2})2\pi}. \tag{3.3.2.2}$$

Dividing Equation (3.3.2.1) for the first test by Equation (3.3.2.1) for the second test and solving for h yields

$$h = \frac{q_2 h_{D1} - q_1 h_{D2}}{q_1 - q_2}. \tag{3.3.2.3}$$

Equations (3.3.2.2) and (3.3.2.3) are a significant improvement over the original method for determining T and h using the Multi-Rate Analysis method (Tsang and Doughty 2003), which involved comparing q_1 and q_2 for one peak with the total wellbore responses (the sums of the flow rates for all peaks, which ideally are equal to the well pumping rates Q_1 and Q_2). However, if there are any non-analyzable peaks or inflow from a non-logged portion of the well, then $\Sigma q \neq Q$, and the method cannot be used. In contrast, Equations (3.3.2.2) and (3.3.2.3) just treat one peak at a time, making it possible to glean information from such non-ideal tests.

Recall that h is defined as the hydraulic head of a flow zone relative to the initial (non-pumping) hydraulic head in the wellbore. Thus under non-pumped conditions, for zones with positive h values there is a driving force for fluid flow from the formation into the borehole, and for zones with negative h values there is a driving force for fluid flow from the borehole into the formation, and there could be internal flow in the wellbore between different zones. Figure 3.3.2 is a schematic diagram showing pumped and non-pumped conditions for three inflow zones with different h values. For pumped conditions, the drawdown h_D is sufficient to pull fluid into the borehole from all zones. In contrast, for non-pumped conditions, fluid flows into the borehole for $h > 0$ and out of the borehole for $h < 0$. This internal flow has important implications for the baseline FEC profile, which may show discrete peaks or step changes at zones with positive h. Internal flow also impacts FFEC profiles subsequently obtained while pumping, in that zones with negative h may not show peaks right away, as low-salinity wellbore fluid entered those zones before pumping began and is the first fluid to be produced at the outset of pumping.

The Multi-Rate Analysis procedure typically lasts for a few days to a week, with five or six FEC profiles collected at each of two or three pumping rates, and has proved to be an effective method to yield estimates of transmissivity, water salinity, and hydraulic head of the inflow zones all along the borehole (Doughty et al. 2005, 2008, and 2013).
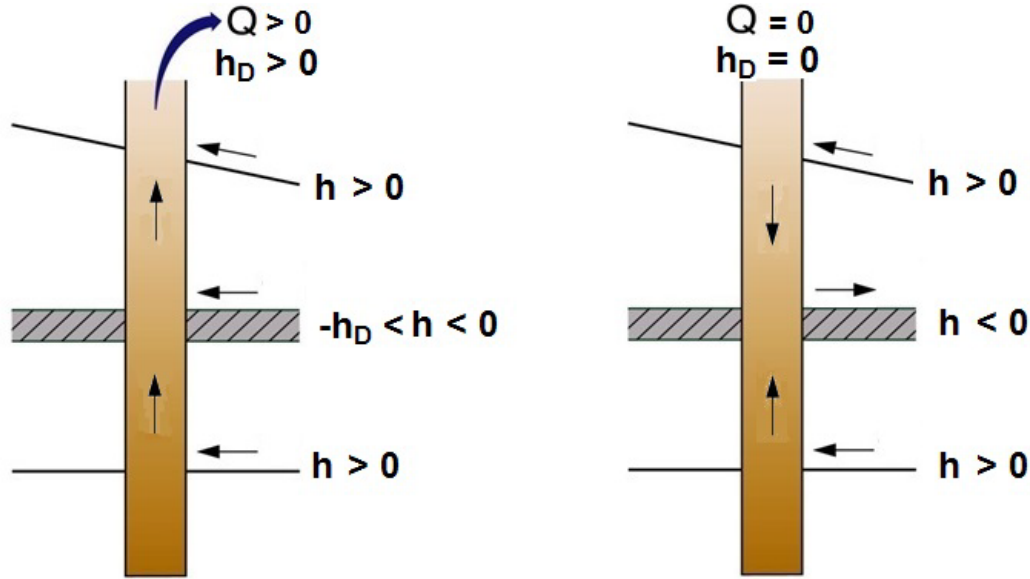
Figure 3.3.2. Schematic of inflow, outflow, and wellbore flow for pumped (left) and non-pumped (right) conditions, when flow zones have different hydraulic head values.

3.3.3   Impact of Baseline Salinity on FFEC Logging Data Analysis

The present report is concerned with FFEC logging conducted during drilling, with data obtained in just one day, without a prior controlled borehole water replacement period. In such cases, it is likely that the baseline FEC levels before logging begins will vary from one test to another. While this complicates some aspects of the analysis, such as precluding application of the Mass Integral Analysis, it can provide useful information. Simple mixing rules may be used to estimate peak height relative to baseline level (i.e., how much of a peak is visible) at steady-state. Assume there are two tests with baseline levels C_{01} and C_{02}, an isolated flow zone with salinity C and inflow rates for the two tests of q_1 and q_2, and upflow from below the flow zone for the two tests of q_{up1} and q_{up2} (i.e., q_{up} is the sum of the inflow rates below the zone of interest). At steady-state, the peak heights observed for the first and second tests would be

$$C_1 = \frac{Cq_1 + C_{01}q_{up1}}{q_1 + q_{up1}} \tag{3.3.3.1}$$

$$C_2 = \frac{Cq_2 + C_{02}q_{up2}}{q_2 + q_{up2}}. \tag{3.3.3.2}$$

If C_{rel} is defined as peak height relative to baseline, and C_{rat} is defined as the ratio of C_{rel} for the two tests, then at steady-state

$$C_{rat} = \frac{C_{rel2}}{C_{rel1}} = \frac{C_2 - C_{02}}{C_1 - C_{01}} = \frac{\left(\frac{Cq_2 + C_{02}q_{up2}}{q_2 + q_{up2}}\right) - C_{02}}{\left(\frac{Cq_1 + C_{01}q_{up1}}{q_1 + q_{up1}}\right) - C_{01}}. \tag{3.3.3.3}$$

Simple algebra yields

$$C_{rat} = \left(\frac{C-C_{02}}{C-C_{01}}\right)\left(\frac{q_2}{q_1}\right)\left(\frac{q_1+q_{up1}}{q_2+q_{up2}}\right). \tag{3.3.3.4}$$

For short-term logging periods with low inflow rates, the observed peaks are nowhere near steady state, and BORE II modeling shows that early-time C_{rat} can be much smaller than steady-state C_{rat}. Thus, Equation (3.3.3.4) provides an upper limit for the observed C_{rat}.

If C is large compared to C_{01} and C_{02}, then the first term in parentheses will be near one, and C_{rat} will just depend on inflow rates. But if $C_{02} > C_{01}$, and C is not much bigger than C_{02}, then the first term could be quite small, greatly decreasing C_{rat}. Hence analyzing tests with different baseline levels can provide information on C values. For peaks that do not show skewing, this is a powerful addition to the analysis method. If baseline concentration is not uniform with depth, then the C_0 value just below the peak of interest could be used in Equation (3.3.3.4) for an approximate analysis. The second term shows the expected direct dependence of C_{rat} on q_1 and q_2. The third term shows how a large upflow from below can decrease peak height above baseline.

3.3.4   Test 1 and Test 2 Data

Over the four months of drilling of the 2500-m COSC-1 borehole, it was noticed that the drillers would carry out the drilling six days a week and then take a break of one day before resuming drilling the following week. Before the break, the drill string was pulled and the well flushed out. The water in the well, and actually the drilling fluid also, turned out to have a low salinity value corresponding to an electric conductivity of ~ 200 µS/cm. This means that at the beginning of the one-day break the borehole is already at a condition corresponding to the point between the first and second of the three-step process for FFEC logging shown in Figure 3.3.1, and thus no replacement of borehole water would be needed for a FFEC logging operation. Once this was recognized, a decision was made to conduct a FFEC logging test during this one-day period, using a downhole pump, a pressure sensor, and an EC/T probe, which were standard equipment already available on the drill site.

One-day tests were performed when the drilling of COSC-1 borehole reached depths of 1600 m and 2500 m, and are denoted Test 1 and Test 2, respectively. The pump and pressure sensor were emplaced 70 m below the water table, which was close to the land surface. The EC/T probe was initially set below the pump depth with its cable guided through tubing attached to the side of the pump. In this way the EC/T probe could be lowered to scan the borehole from about 100 m depth (the extent of the cased part of the borehole below which the borehole was uncased) to the borehole bottom. Because of the design of the EC/T probe, only the FEC data recorded during the downward scan of the probe were used in subsequent data analysis. The downward speed of the probe was about 10 m/min, and the return of the probe back to the top of borehole was at a higher speed about 20 m/min. This means that it took about 3.75 hours to complete each logging scan from 100 m to 1600 m and back during Test 1. For Test 2, the logging tool scanned from 100 m to 2000 m (the maximum depth the tool was rated for), with a 4.75 hour round trip. In each of the one-day FFEC logging operations, three FFEC versus depth profiles were obtained.

For Test 1, a number of field problems were encountered which were unrelated to the FFEC method, such as accidental sliding of the pump in the borehole by 2 m, entangling of pump and logging cables, and interruption of electric power supply at the drill site. Also, the initial estimate of pump rate was too high so that the water level drawdown reached the depth of the pump, resulting in a fluctuating pumping rate. Nevertheless, an average flow rate of 3.5 L/min out of the borehole was obtained during logging at a drawdown of 70 m. For the second test, the drawdown was set at 50 m, but pumping was also interrupted several times due to operational problems, and flow rate out of the borehole was highly variable,

averaging 2.5 L/min during logging. Figure 3.3.3 and Figure 3.3.4 show wellbore pressure and pumping rate for Test 1 and Test 2, respectively.
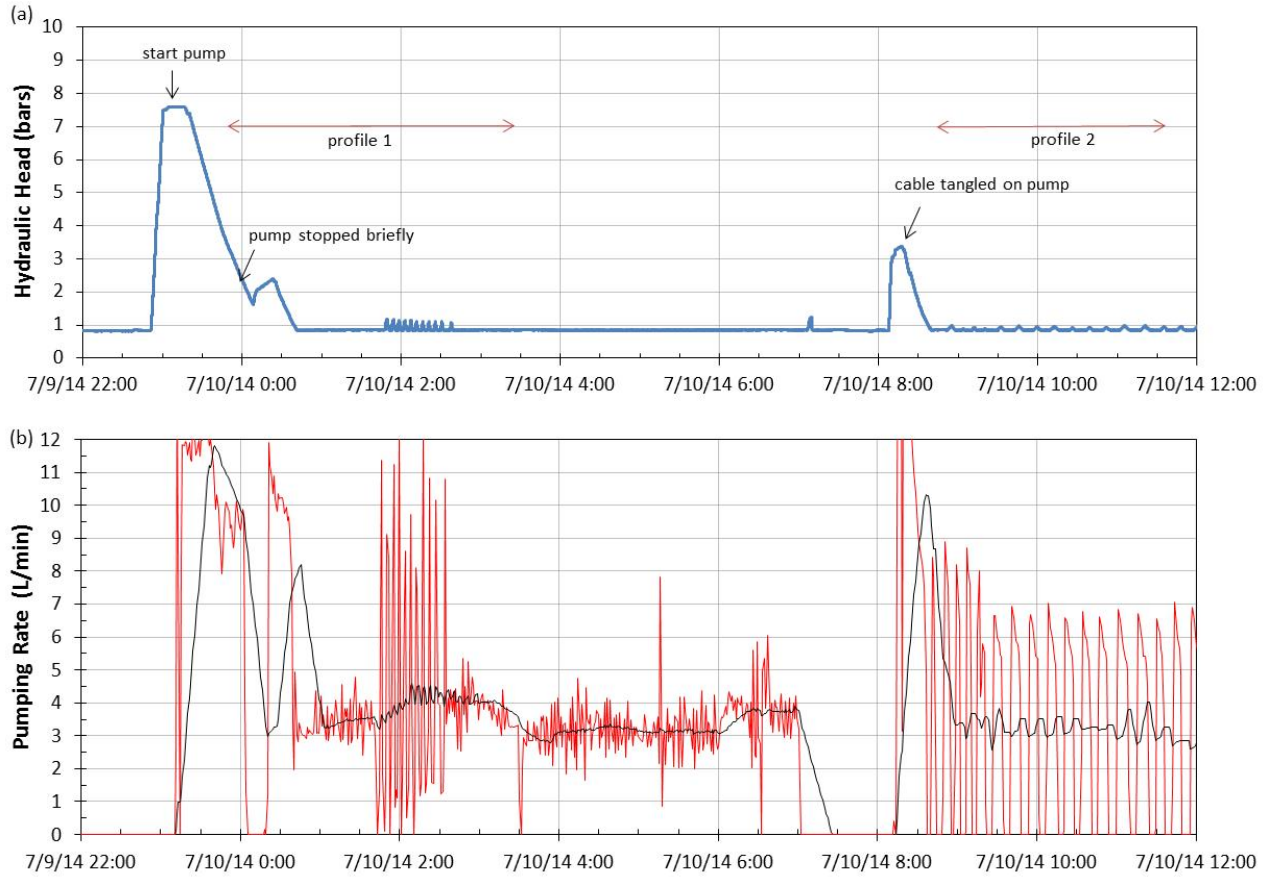
Figure 3.3.3. Test 1 operating conditions: (a) wellbore hydraulic head, with logging periods shown, and (b) pumping rate, with 25-minute moving average shown.
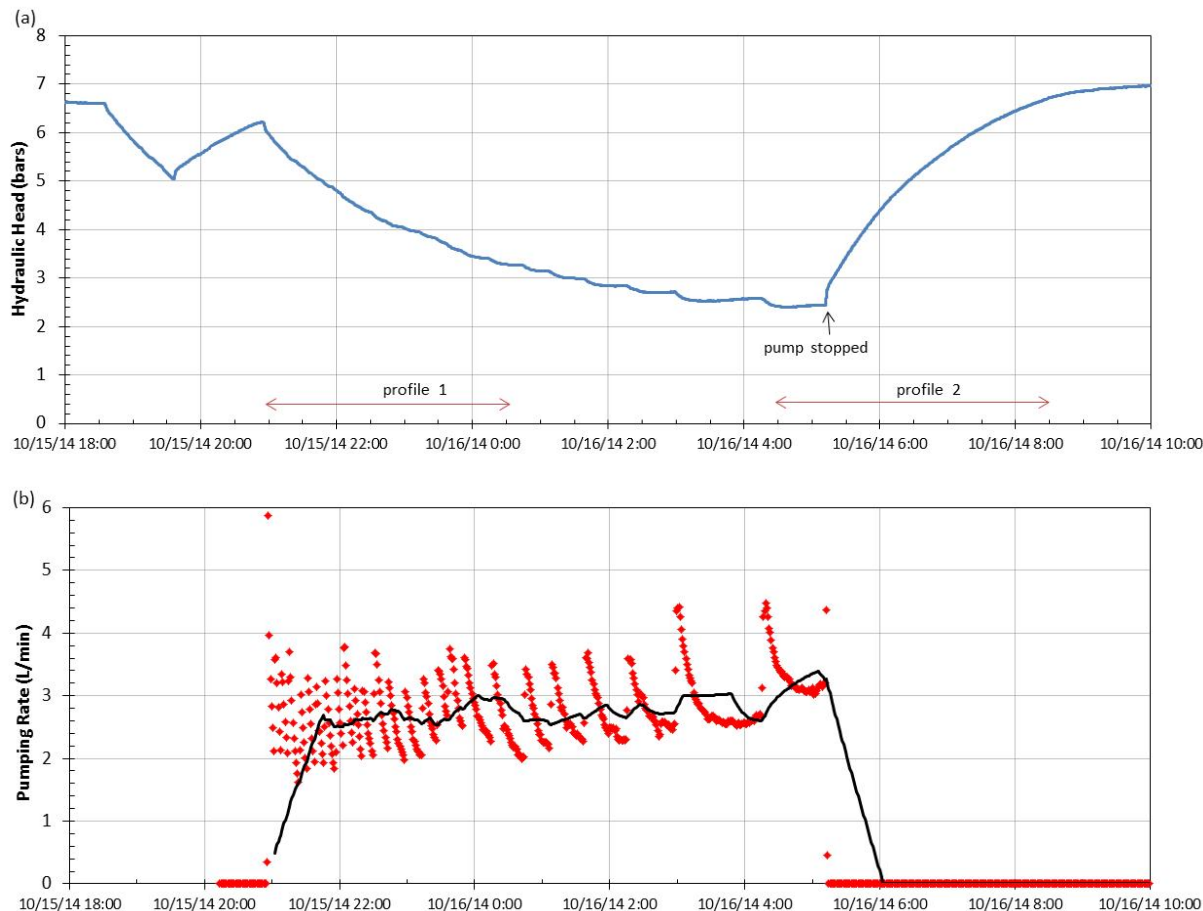
Figure 3.3.4. Test 2 operating conditions: (a) wellbore hydraulic head, with logging periods shown, and (b) pumping rate, with 50-minute moving average shown.

For both tests, a baseline FFEC logging profile was obtained under non-pumped conditions, then two more profiles were obtained during pumping, at about 3 and 11 hours after pumping started. Figure 3.3.5 and Figure 3.3.6 present the FFEC logs for Test 1 and Test 2, respectively. In these plots the FEC values have been corrected to 20°C-equivalent values (Tsang et al. 1990) using temperature along the borehole (T_b) measured at the same time with the EC/T probe:

$$\text{FEC}(20^\text{o}\text{C}) = \text{FEC}(T_b)/[1 + S(T_b - 20^\text{o}\text{C})] \qquad (3.3.4.1)$$

where $S = 0.024 \ ^\text{o}\text{C}^{-1}$.

The FEC values in these plots can be related to salinity or NaCl concentration C through an approximate formula (Tsang et al. 1990) valid for the range of FEC values encountered in this paper:

$$1 \text{ FEC } (\mu\text{S/cm}) \approx 1870 \ C \text{ (g/L)} \qquad (3.3.4.2)$$

In this paper, C and FEC values are used interchangeably with this conversion in mind.
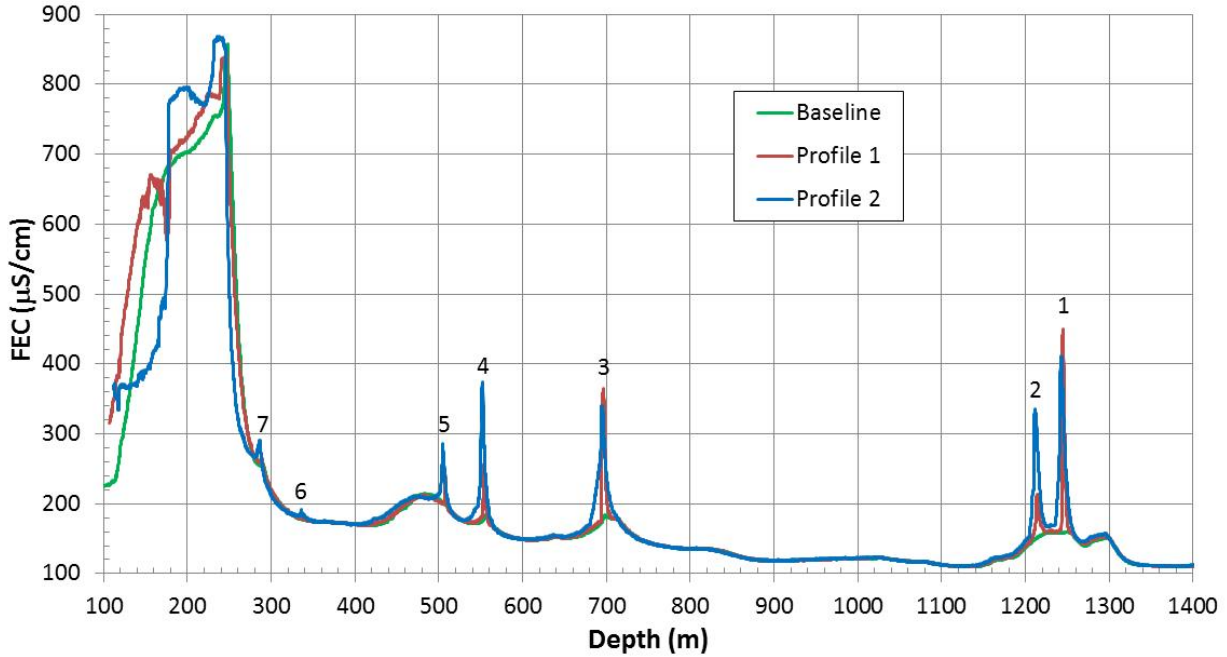
Figure 3.3.5. FFEC profiles measured during Test 1. Peaks are identified by number, from deep to shallow.
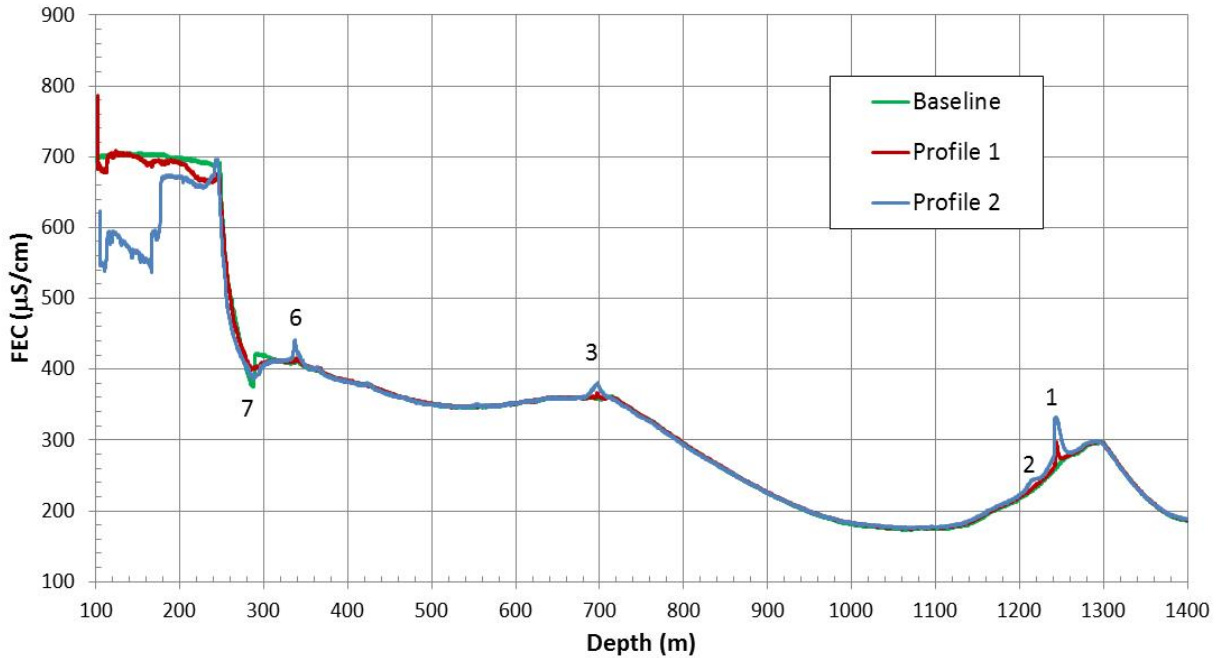
Figure 3.3.6. FFEC profiles measured during Test 2.

Figure 3.3.5 and Figure 3.3.6 show that the FFEC data are erratic at depths above 250 m, which correspond to the part affected by afore-mentioned unrelated operational problems. From 250 m down to 1600 m, the Test 1 FFEC profiles show distinct peaks at seven locations indicating inflows at depths of 288, 338, 508, 553, 697, 1214, and 1243 m. Thus, this simple one-day test already yields very useful information; i.e., the identification of the depths at a high resolution of hydraulically conductive zones

with both large and small flow rates. It is at these depths where post-drilling double packer tests and water sampling should be done. All of the peaks look symmetric, indicating that inflow rates are too small to produce significant skewing of peaks up the wellbore within the one-day period allocated for FFEC logging during drilling.

- No additional peaks were identified between depths of 1600 m and 2000 m during Test 2. Comparison of the FFEC profiles for Test 2 (Figure 3.3.6) and Test 1 (Figure 3.3.5) show the following important differences.
- The baseline FEC profile is much higher in Test 2 than in Test 1, which precludes use of the Mass Integral Analysis for determining the qC product for each peak. Thus, a detailed fit using BORE II must be done, as is described in the next section.
- For Test 2, Peaks 1-3 (at depths of 697, 1214, and 1243 m) are much smaller than the corresponding Test 1 peaks, and Peak 4 (553 m) and Peak 5 (508 m) have disappeared entirely, suggesting that the h values of these flow zones are negative (Equation 3).
- Peak 6 (338 m) shows a larger peak for Test 2 than for Test 1 ($C_{rat} > 1$ in Equation 3.3.3.4), consistent with inflows for Peaks 1-5 being much smaller for Test 2 than for Test 1 (i.e., $q_{up2} \ll q_{up1}$ in Equation 3.3.3.4), and a positive h value for this flow zone (i.e., $q_2 \sim q_1$ in Equation 3.3.3.4).
- At a depth of 288 m, the small Peak 7 in Test 1 has become a local minimum in Test 2, suggesting that the C value for this zone is in between the baseline values for the two tests, C_{01} and C_{02}.

All of these features are amenable to analysis with BORE II and will be described in the following section.

3.3.5   BORE II Analysis of Test 1 and Test 2

The baseline FEC profiles are used as the initial conditions for the BORE II calculations. The baseline FEC profiles were measured over the course of several hours prior to the start of pumping, but to use them as the initial condition assumes that they were measured instantaneously at $t = 0$, when the pump was turned on. This is a reasonable assumption if the baseline FEC profile represents steady-state conditions in the wellbore, which is supported for depths below 250 m by the subsequent FFEC profiles, which change in time only at the discrete flow zones.

Normally, when the baseline profiles represent the result of a careful borehole water replacement operation, local minima and maxima are interpreted as representing flow zones with positive h values and relatively low and high C values, respectively. However, for the present tests, the baseline profiles follow the washing out of the borehole, which was done under unknown conditions, making this interpretation uncertain, as evidenced by the variability between the baseline profiles for Test 1 and Test 2.

3.3.5.1   Analysis of Test 1

The first step of the BORE II analysis is to match the FFEC profiles for Test 1 by picking q and C values for each peak by trial and error. Because of the lack of skewing and consequent difficulty of determining q and C independently, this fitting exercise is done twice, using two different approaches. In the first approach, a low value of C is used as the starting guess for each peak, which tends to make the corresponding q large, and C is kept as small as possible during the fitting process. In the second

approach, high values of C are used as the starting guesses, which tend to make the corresponding q values small, and C values are kept as large as possible during the fitting process.

The dispersion coefficient and t_0, the time at which formation fluid begins to flow into the wellbore for each peak, are also chosen by trial and error, and these are the same for the Low-C and High-C approaches. Two peaks do not show normal growth: at Peak 1 at a depth of 1243 m and at Peak 3 at a depth of 697 m, the three-hour peak is just as high as the 11-hour peak, which is attributed to the highly variable pumping rate. No t_0 can be determined for these peaks, and just the late-time peak is matched.

Figure 3.3.7 shows the match for the Low-C approach (the High-C approach yields a comparable match). All the peaks can be matched reasonably well. At two depths in the profiles, skewing provides independent information on q: at the sharp upslope just above Peak 7 and at the gradual downslope between Peak 5 and Peak 6. Matching the skewing constrains the sum of the q values for all the peaks below that point. Table 3.3.1 shows the q, C, and t_0 values obtained for both approaches. Note that the sum of the q values, 110-127 ml/min, is far less than the rate at which the well is being pumped, ~3.5 L/min, indicating that the seven feed points between 250 and 1600 m do not represent the only inflow to the borehole. This is consistent with the large FEC values obtained for the 100-250 m depth range, but as mentioned before, operational problems precludes analysis of this data. The differences in q and C between the Low-C and High-C approaches provide a measure of the uncertainty associated with these parameters, which is illustrated in Figure 3.3.8.
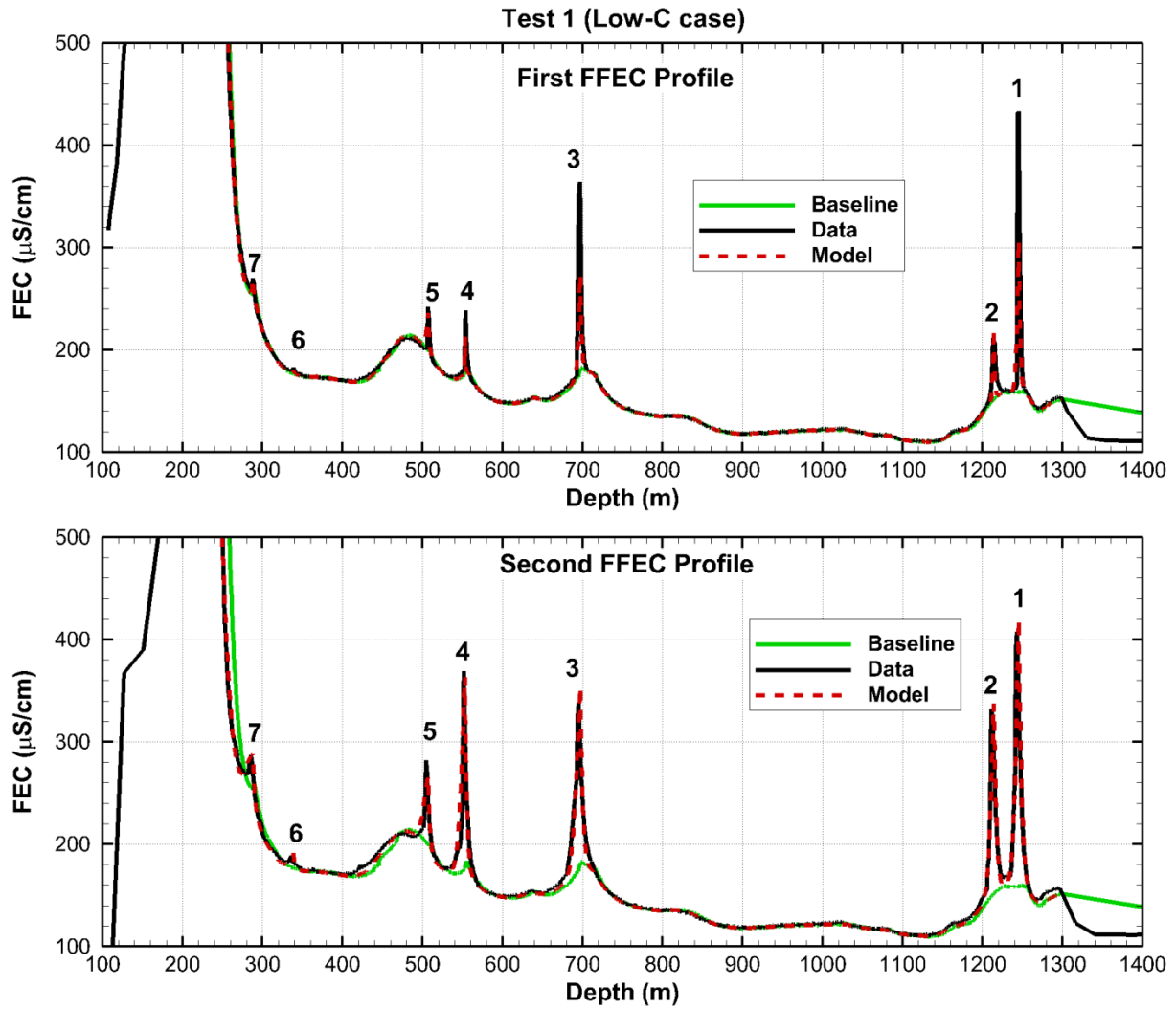
Figure 3.3.7. BORE II fit to the FFEC profiles for Test 1, using the Low-*C* approach.

Table 3.3.1. Parameters obtained for each hydraulically conductive zone from BORE II fitting of Test 1 FFEC data using the Low-C and High-C approaches: depth, flow rate (q1), starting time for formation flow (t01), and salinity (C). Values of q1, t01, and C obtained by an independent analysis (Tsang et al. 2016) are also shown.

Peak No.	Depth (m)	Low-C Approach			High-C Approach			Independent Analysis		
		q_1 (mL/min)	t_{01} (hr)	C (μS/cm)	q_1 (mL/min)	t_{01} (hr)	C (μS/cm)	q_1 (mL/min)	t_{01} (hr)	C (μS/cm)
1	1243	14	0	1700	11	0	2200	10	0	2244
2	1214	18	2.3	1150	41	2.3	620	28	1.67	935
3	697	21	0	1000	14	0	1400	22	0	1309
4	553	13	2.0	1800	7.7	2.0	2900	19	1.16	1122
5	508	4.8	0	1800	3.5	0	2800	5	1.1	1496
6	338	1.7*	1.5	1200	0.55**	1.5	2900	3	0.67	748
7	288	55	1.0	380	54	1.0	380			
Sum		127.5			109.9			87		

*increased to 2.7 for Multi-Rate Analysis
**increased to 0.85 for Multi-Rate Analysis

Table 3.3.1 also shows the q, t_0, and C values obtained by an independent analysis of the Test 1 FFEC data (Tsang et al. 2016). For the three deepest peaks, the q and C values for the independent analysis are close to or within the range of the Low-C and High-C approaches, but for the shallowest three peaks, C values are lower and q values are higher than that range (Figure 3.3.8). This result is not surprising for two reasons. First, the shallower three peaks are smaller, so the signal-to-noise ratio is smaller, making it easier to accept matches with a range of q and C values. Second, it is common when doing FFEC analysis that as one moves up the borehole, the matching procedure becomes less certain, as any errors introduced by imperfect matches for deeper peaks are propagated up the borehole.

As mentioned earlier, when little skewing of peaks is visible, the qC product for a peak can usually be determined with more certainty than can q and C individually. This finding holds true for the Test 1 analysis, as shown in Figure 3.3.8 where the spread among values of the qC product is smaller than the spread among q or C values for all peaks except Peak 3.
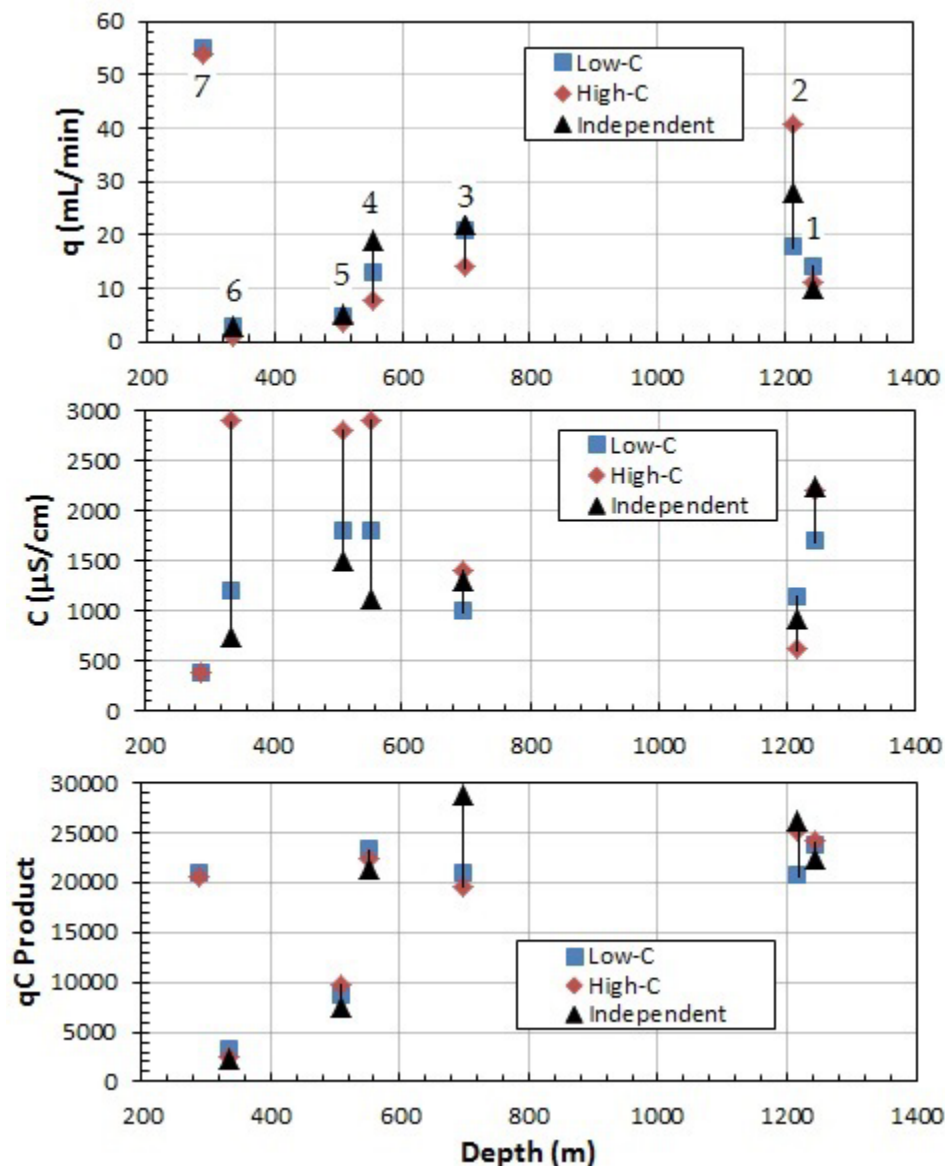
Figure 3.3.8. Comparison of results for Test 1 for Low-*C* approach, High-*C* approach, and independent analysis of Tsang et al. (2016), for *q* (top frame), *C* (middle frame), and *qC* product (bottom frame).

3.3.5.2   *Analysis of Test 2*

The same matching procedure is used for Test 2, except that the *C* values and dispersion coefficient are fixed at the values determined by the Test 1 fit. Figure 3.3.9 shows the match for the Low-*C* approach (the High-*C* approach yields a comparable match). As before, all the peaks can be matched reasonably well. Table 3.3.2 shows the *q* and t_0 values obtained for Test 2. Note that Peak 4 and Peak 5 have disappeared (i.e., $q \le 0$) but Peak 6 has a larger *q* value than for Test 1. These features will be discussed further in the Multi-Rate Analysis described below.

What was Peak 7 at 288 m in Test 1 is now a minimum in all the Test 2 profiles. It is hypothesized that the *C* value for this peak is ~380 µS/cm, which is higher than the Test 1 baseline value at that depth (so produces a peak) but lower than the Test 2 baseline value (so produces a minimum). Subsequent FFEC logging at this borehole in Test 3 and Test 4 (described below) with even larger baseline FEC values

produces FFEC profiles that persist in showing a minimum at 288 m, supporting this hypothesis. Unfortunately, the Test 2 profiles do not show the development of a negative peak at 288 m in a manner that can be matched with BORE II, so the *q* value for Peak 7 is very uncertain.
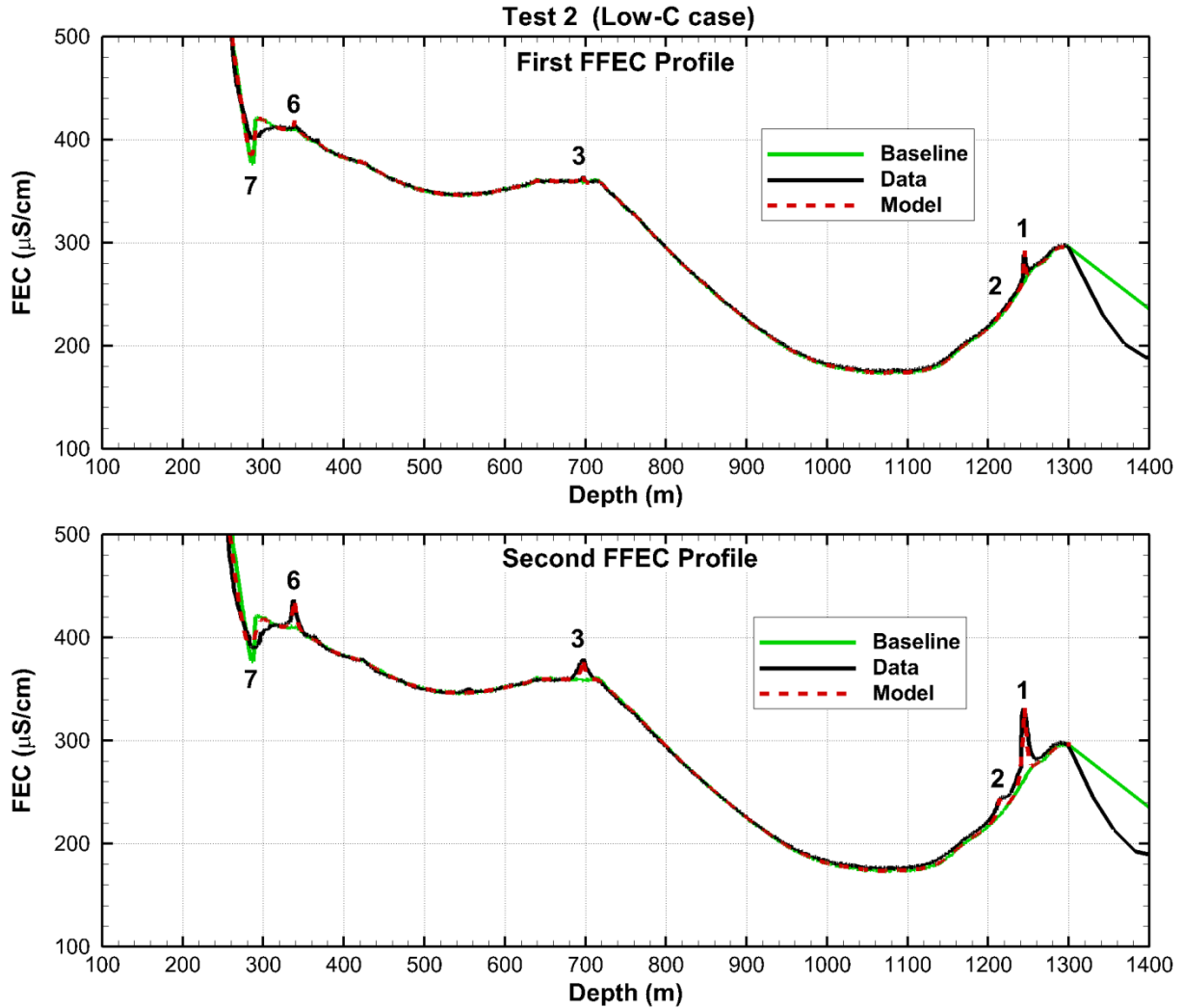
Figure 3.3.9. BORE II fit to the FFEC profiles for Test 2, using the Low-*C* approach.

Table 3.3.2. Parameters obtained for each hydraulically conductive zone from BORE II fitting of Test 2 FFEC data using the Low-C and High-C approaches: depth, flow rate (q_2), starting time for formation flow (t_{02}), and salinity (C).

Peak No.	Depth (m)	Low-C Approach			High-C Approach		
		q_2 (mL/min)	t_{02} (hr)	C (μS/cm)	q_2 (mL/min)	t_{02} (hr)	C (μS/cm)
1	1243	4.0	1.5	1700	3.1	1.5	2200
2	1214	1.4	1.5	1150	3.6	1.5	620
3	697	2.9	1.5	1000	1.9	1.5	1400
4	553	0*	0	1800	0*	0	2900
5	508	0*	0	1800	0*	0	2800
6	338	3.2**	1.0	1200	1.1***	1.0	2900
7	288	40	0	380	40	0	380
Sum		56.8			48.7		

*upper limit
**decreased to 1.9 for Multi-Rate Analysis
***decreased to 0.61 for Multi-Rate Analysis

3.3.5.3   *Multi-Rate Analysis of Test 1 and Test 2*

Next, the q values from Test 1 and Test 2 are used in Equation (3.3.2.2) to calculate T and Equation (3.3.2.3) to calculate h for each hydraulically conductive zone. For the T calculation, $r_{wb} = 0.048$ m (corresponding to a wellbore diameter of 9.6 cm) and $r_{out} = 48$ m, which is an estimate used by Tsang et al. (2016). Table 3.3.3 shows the results of the Multi-Rate Analysis. For all peaks, nearly the same h values are obtained for the Low-C and High-C approaches, which greatly increases confidence in the results, given all the limitations of one-day logging, including no controlled borehole water replacement, highly variable pumping rate, few FFEC profiles obtained, and minimal skewing observed.

Table 3.3.3. Parameters obtained from the Multi-Rate Analysis of Test 1 ($h_{D1} = 70$ m) and Test 2 ($h_{D2} = 50$ m) using the Low-C and High-C approaches: transmissivity T (from Equation 2) and hydraulic head h (from Equation 3) for each hydraulically conductive zone. The range of C values from the Low-C and High-C approaches is also shown.

Peak No.	Depth (m)	T (m^2/s)	h (m)	C (μS/cm)	C (g/L)
1	1243	7E-9 - 9E-9	-42	1700 - 2200	0.9 - 1.2
2	1214	2E-8 – 3E-8	-48	620 - 1150	0.3 - 0.6
3	697	1E-8 - 2E-8	-47	1000 - 1400	0.5 - 0.7
4	553	7E-9 - 1E-8	-50*	1800 - 2900	1.0 - 1.6
5	508	3E-9 – 4E-9	-50*	1800 - 2800	1.0 - 1.5
6	338	2E-10 - 7E-10**	0**	1200 - 2900	0.6 - 1.6
7	288	1E-8***	3 – 7***	380	0.2

*Upper limit
**Placeholder result
***Very uncertain

Note that the h values for Peaks 1-3 are all negative, and have magnitudes close to $h_{D2} = 50$ m. Thus, for Test 2 there is little driving force for flow from the hydraulically conductive zone into the wellbore,

resulting in small peaks. For Peak 4 and Peak 5, which are absent in Test 2, $q = 0$ is assumed, and Equation (3.3.2.3) yields $|h| = h_{D2} = 50$ m. This is actually an upper limit for h, which could be anywhere between -70 m and -50 m (h must be greater than -70 m because these zones produced peaks in Test 1, for which $h_{D1} = 70$ m). If $h < -50$, then there will be outflow from the wellbore to the flow zone during Test 2. The q and h values for Peaks 4 and 5 will be determined more accurately when Test 3 and Test 4 data are analyzed below.

For the simple steady-state flow presumed in the derivation of Equation (3), the q value for a peak cannot increase when h_D decreases, as is obtained for Peak 6 from the individual fits to Test 1 and Test 2. Thus, some goodness of fit is sacrificed and a slightly larger q value is assigned for Test 1 (q_1), and a slightly smaller q value is assigned for Test 2 (q_2), such that $q_1 > q_2$. To maintain the best fit possible, the ratio q_2/q_1 should be as large as possible, but if q_2/q_1 is too close to 1, the value of h determined by Equation (3.3.2.3) will be unreasonably large. A conservative assumption is to take $q_2/q_1 = h_{D2}/h_{D1} = 50/70$, which yields $h = 0$. The h value for Peak 6 will be determined more accurately when Test 3 and Test 4 data are analyzed below.

This assumption of $h = 0$ for Peak 6 can be checked for consistency with Equation (3.3.3.4) for C_{rat}, the ratio of steady-state peak heights relative to baseline for Test 1 and Test 2. For Peak 6, Figure 3.3.5 and Figure 3.3.6 show that at the final logging times, the Test 2 peak height above baseline is 2.5 times bigger than that for Test 1, which provides a lower bound for steady-state C_{rat}. Table 3.3.4 summarizes the three multiplicative terms in Equation (3.3.3.4) that determine C_{rat}, for four C values. The middle two C values are the Peak 6 values obtained from the Low-C and High-C fitting approaches. The lowest and highest C values are included to illustrate the dependence of C_{rat} on a larger range of C. The key requirements for obtaining $C_{rat} > 1$ are $C \gg C_{01}$ and $C \gg C_{02}$, so that the first term of Equation (3.3.3.4) is not too small; $q_2 \sim q_1$ so that the second term is not too small; and $q_{up2} \ll q_{up1}$, $q_2 \ll q_{up2}$, and $q_1 \ll q_{up1}$ so that the third term is large. The large decrease in the height of Peaks 1-5 between Test 1 and Test 2 ensures that $q_{up2} \ll q_{up1}$, and the small size of Peak 6 means the q_{up} terms dominate the third term. Table 3.3.4 indicates that for the Low-C and High-C approaches, steady-state C_{rat} values are 4.0 and 5.5, respectively, both greater than the observed C_{rat} of 2.5, verifying that it is indeed plausible for Peak 6 to be larger in Test 2 than in Test 1 for the assumed C and h values.

Table 3.3.4. Terms in Equation (3.3.3.4) for steady-state C_{rat} for Peak 6 are shown in bold face, using baseline values $C_{01} = 178$ µS/cm and $C_{02} = 408$ µS/cm, from Figure 3.3.5 and Figure 3.3.6, respectively, and assuming that $q_2/q_1 = h_{D2}/h_{D1} = 0.71$. The C_{rat} value observed in the field for Test 1 and Test 2 is about 2.5 – the steady-state C_{rat} shown in the bottom row must be larger than that.

		Low-*C* Approach	High-*C* Approach	
C (µS/cm)	500	1200	2900	5000
$(C$-$C_{02})/(C$-$C_{01})$	0.29	0.77	0.92	0.95
q_1 (mL/min)	4.0	2.7	0.85	0.20
q_2 (mL/min)	2.9	1.9	0. 61	0.14
q_2/q_1	0.71	0.71	0.71	0.71
q_{up1} (mL/min)	71	71	77	77
q_{up2} (mL/min)	8.3	8.3	8.6	8.6
q_{up1}/q_{up2}	8.5	8.5	8.9	8.9
$(q_1$+$q_{up1})/(q_2$+$q_{up2})$	6.7	7.2	8.4	8.8
Steady-state C_{rat}	1.4	4.0	5.5	6.0

Additional results for smaller (500 µS/cm) and larger (5000 µS/cm) values of *C* are also given in Table 3.3.4, to provide insight into the impact of *C* on C_{rat}. For $C = 500$ µS/cm, not much bigger than C_{02} (408 µS/cm), the first term in Equation (3.3.3.4) becomes quite small (0.29), producing too small a value of C_{rat} (1.4). In contrast, a very large value of $C = 5000$ µS/cm does not increase the first term appreciably (0.95 compared to 0.92), so C_{rat} does not change much (6.0 compared to 5.5). Thus, for estimating *C* for Peak 6, values of $C \leq 500$ µS/cm can be eliminated from consideration, and there is no need to hypothesize very high values of $C \geq 5000$ µS/cm to produce the 2.5 times larger peak observed in Test 2 compared to Test 1.

As described in the previous section, the Test-2 q value obtained for Peak 7 is very uncertain. Hence, the corresponding *T* and *h* values are very uncertain too.

Normally, the *h* values obtained with the Multi-Rate Analysis are compared to the t_0 values obtained from the individual fits as a consistency check: large t_0 values should be associated with negative *h* values because low-salinity wellbore fluid flowed into the formation during borehole water replacement. This relationship holds for the peaks for which a t_0 could be obtained, but the highly variable pumping rate means that not much significance can be associated with this result.

3.3.6   Test 3 and Test 4 Data and Qualitative Analysis

Test 3 and Test 4 were conducted about one year after the drilling the COSC-1 borehole was completed. For Test 3, the drawdown was set at 50 m, and for Test 4 drawdown was set at 10 m. As shown in Figure 3.3.10, these water levels were reasonably well maintained during logging, but the pumping rate still fluctuated. Average flow rates out of the borehole were about 2.5 L/min and 0.75 L/min for Test 3 and Test 4, respectively.
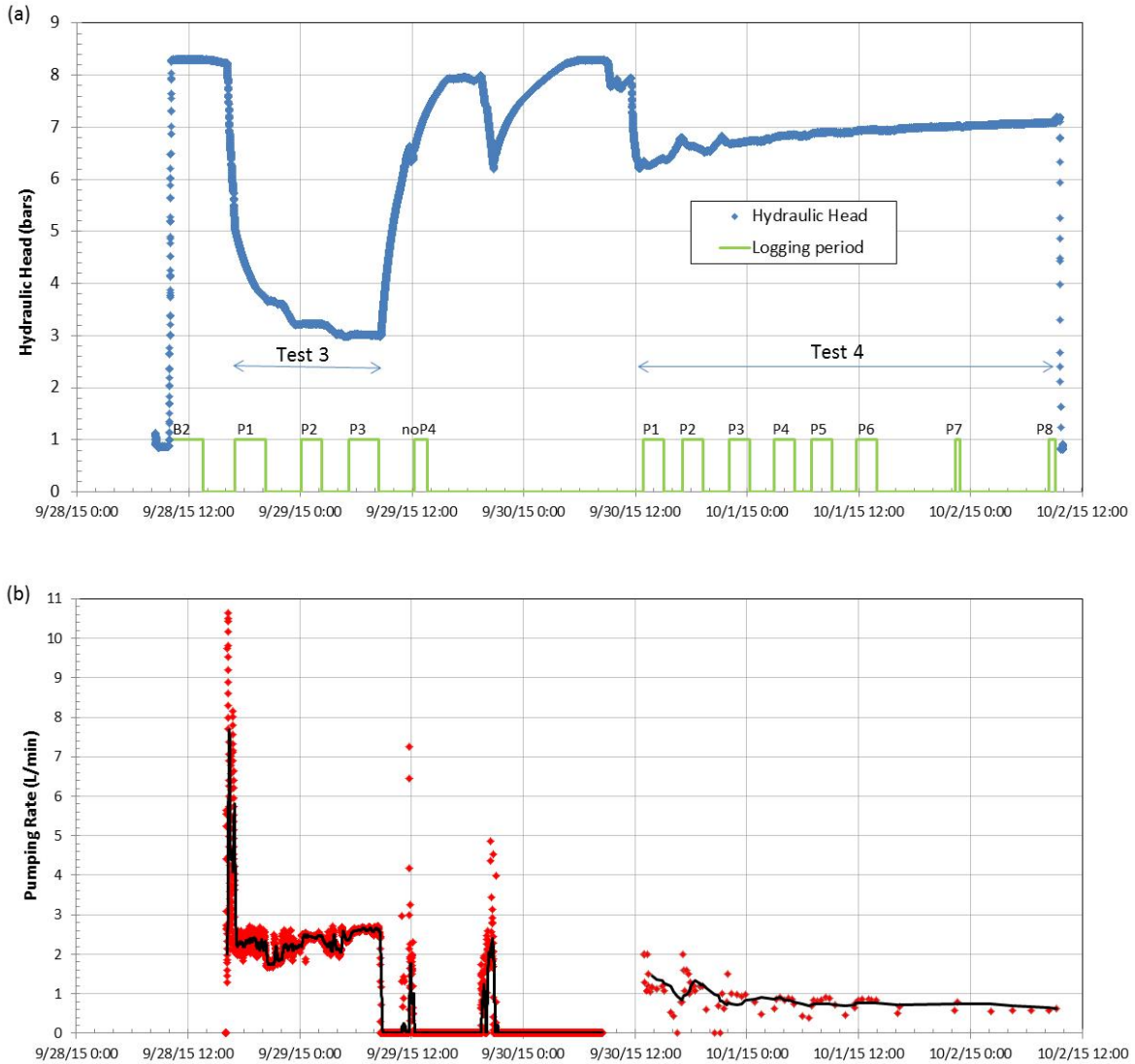
Figure 3.3.10. Test 3 and Test 4 operating conditions: (a) wellbore hydraulic head, with logging periods shown, and (b) pumping rate, with 10-minute moving average shown.

Operational problems precluded doing borehole water replacement prior to logging, so baseline FEC levels were even higher than for Test 2. Figures 3.3.11 and 3.3.12 present the FFEC logs for Test 3 and Test 4, respectively. For Test 3, there is a baseline log, three logs obtained during pumping, and a log obtained after the pump was turned off (not shown). For Test 4, eight logs were obtained during pumping, but the final two only went to a depth of 400 m.
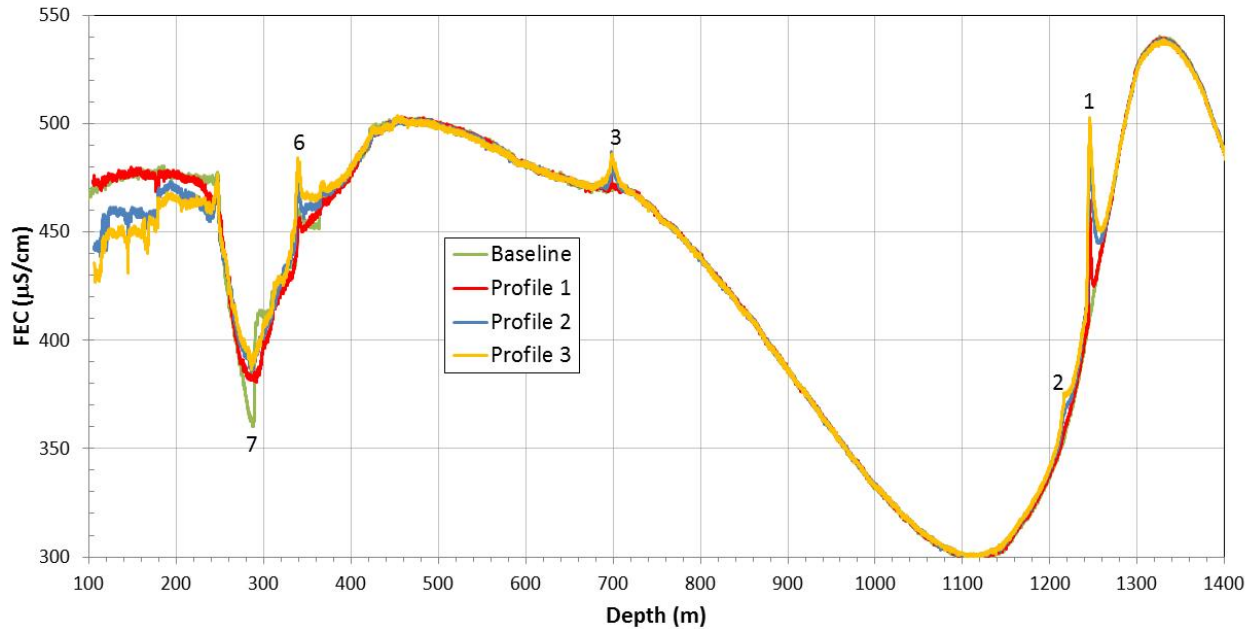
Figure 3.3.11. FFEC profiles measured during Test 3.
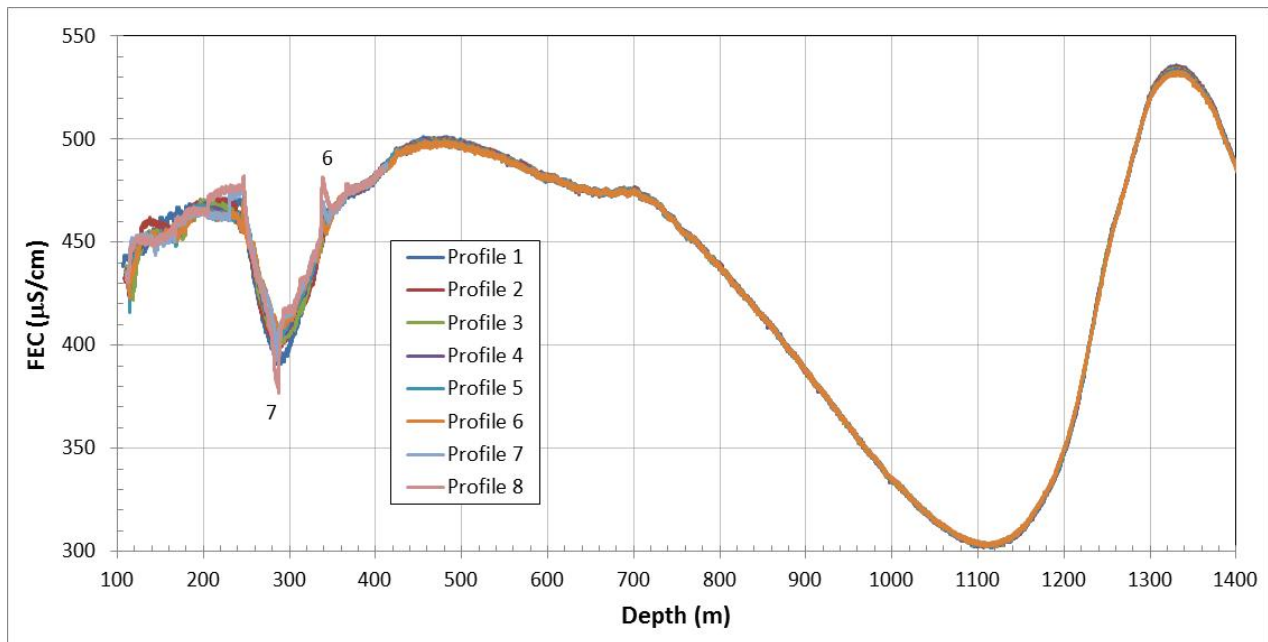
Figure 3.3.12. FFEC profiles measured during Test 4.

Figure 3.3.13 shows the FFEC logs for all four tests together, to provide an overall look at the data. Peaks 1-5 for Test 2 are disproportionally smaller than peaks 1-5 for Test 1, considering the difference in drawdown (50 vs 70 m). As shown in Table 3.3.3, this indicates that the h values for zones 1-5 are negative. The peaks for Test 3 look similar to those for Test 2, which is expected because the drawdowns specified for both tests are 50 m. For Test 4, peaks 1-5 are all absent. This is consistent with the h levels

for these zones shown in Table 3.3.3: all are lower than -10 m, so a drawdown of 10 m is insufficient to induce inflow into the borehole. Peak 6 is present for both Test 3 and Test 4, enabling Multi-Rate Analysis to estimate h. The persistence of the FEC minimum at $z = 288$ m suggests the inflow of low-C water from zone 7 occurs for all drawdown values and under non-pumped conditions, implying that h for zone 7 is positive.
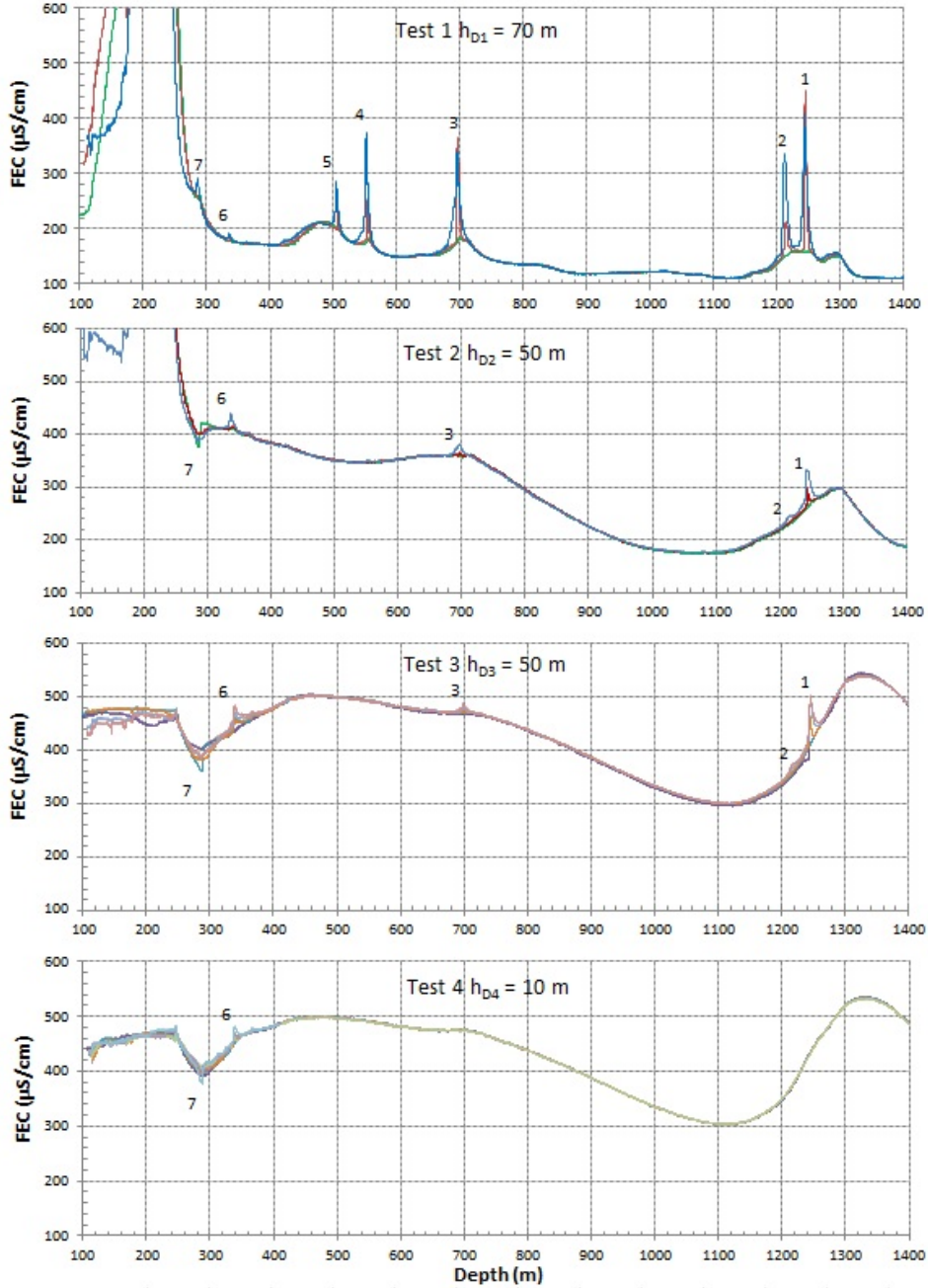
Figure 3.3.13. All measured FFEC profiles plotted on the same scale, for qualitative assessment.

3.3.7   BORE II Analysis Including Test 3 and Test 4

3.3.7.1   Multi-Rate Analysis of Test 1, Test 2, and Test 3

BORE II was used to fit the FFEC profiles for Test 3, and indicates that slightly higher q values are needed to match Test 3 than Test 2 for peaks 1, 2, and 6, suggesting h_{D3} is actually larger than h_{D2}, which is consistent with the visibly smaller drawdown during logging for Test 2 compared to Test 3 (Figures 3.3.4 and 3.3.10). The slow water-level decline for Test 2 could also mean that the flow coming out of the formation is actually smaller than the pumping rate, with the difference coming from wellbore storage, which would also be consistent with smaller inflow rates for Test 2 than for Test 3. The q values for peaks 1, 2, and 6 for Test 2 and Test 3 can be used in Equation (3.3.2.3) to determine the effective difference between h_{D2} and h_{D3}, producing $h_{D2} = 48$ m, just slightly smaller than $h_{D3} = 50$ m.

In contrast, Peak 3 requires a smaller q to match Test 3 than to match Test 2, which is not consistent with $h_{D3} > h_{D2}$. However, if the C value for Peak 3 were smaller than the range of C values obtained from fitting Test 1 and Test 2 (1000 – 1400 μS/cm), then the increase in baseline C between Test 2 and Test 3 could produce a smaller Peak 3 for Test 3, even with a slightly larger q value that is consistent with the slightly larger drawdown, as shown by Equation (3.3.3.4). For the Low-C approach, decreasing C for Peak 3 from 1000 μS/cm to 600 μS/cm and refitting q for peaks 3-7 for Test 1, Test 2, and Test 3 produces a reasonable fit to profiles for all these tests. Thus, $C = 600$ μS/cm for Peak 3 is retained in the modified Low-C approach. It turns out that the large difference in baseline FEC for the different tests, originally considered a shortcoming, can actually provide constraints on the C values of individual peaks, which is very useful information for low-flow peaks that do not show appreciable skewing.

Peak 7 requires a much smaller inflow for Test 3 than for Test 2 to produce the nearly zero upflow at the top of the logged zone. This discrepancy may not be too surprising, considering the large uncertainty associated with the Peak 7 analysis for Test 2. Additionally, the estimate of C is increased slightly, from 380 to 390 μS/cm, to better match all three tests. Despite the lack of quantitative agreement, the conclusion that the Peak 7 has a positive h remains.

Table 3.3.5 summarizes the q, C, h, and T values obtained from Multi-Rate Analysis of Test 1 and Test 2, with consideration of the Test 3 profiles, for all peaks except Peak 6.

Table 3.3.5. Parameters for Peaks 1-5 and Peak 7 obtained from the Multi-Rate Analysis of Test 1/Test 2, with consideration of the Test 3 profiles. Peak 6 parameters are from Multi-Rate Analysis of Test 3/Test 4.

		Test 1	Test 2	Test 3	Test 4			
	h_D (m)	70	48	50	10			
Peak No.	Depth (m)	q_1 (mL/min)	q_2 (mL/min)	q_3 (mL/min)	q_4 (mL/min)	C (μS/cm)	h (m)	T (m²/s)
1	1243	14	4	4.7		1700	-39	8E-9
2	1214	17	1.4	1.8		1150	-46	1E-8
3	697	40	8	9.8		600	-42	3E-8
4	553	10	0	0.1		2350	-48	8E-9
5	508	4.5	0	0.1		2350	-48	4E-9
6	338	1.7	2.6	2.7	1.6	1200	48	5E-10
7	288	55	40	10	3.4	390	11	1E-8

3.3.7.2   Multi-Rate Analysis of Test 3 and Test 4 and Application to Non-Pumped Conditions

Test 4 shows only one normally growing peak, Peak 6, and it can be readily fit with BORE II, yielding q_4 = 1.6 mL/min. Then, assuming h_{D3} = 50 m, h_{D4} = 10 m, and q_3 = 2.7 mL/min, Equation (3.3.2.2) and Equation (3.3.2.3) can be used to determine the h and T values shown in Table 3.3.5, which are an improvement on the conservative estimates obtained from the Test 1/Test 2 Multi-Rate Analysis.

Test 4 does not show normal peak growth for Peak 7, so it cannot be analyzed quantitatively. Any small value of q_4 can be used for a qualitative match, so one that gives a consistent h value with the Test 1/Test 2 Multi-Rate Analysis is used.

There is now an h value and a T value associated with every zone (Table 3.3.5), so Equation (1) can be used to predict inflow or outflow for any applied value of h_D. In particular, the outflow rates for Peaks 1 - 5 for Test 4 with h_{D4} = 10 can be determined, as shown in Table 3.3.6. When these outflow rates are used in a BORE II simulation for Test 4, there is significant downward skewing of the profiles, as shown in Figure 3.3.14. However, repeated logging over a period of 45 hours during Test 4 (Figure 3.3.12) indicates no visible changes of the FFEC profiles except at Peaks 6 and 7. This suggests that the h values estimated from analysis of Test 1, Test 2, and Test 3 are too negative for Peaks 1 - 5, resulting in too great an outflow for Test 4. By trial and error, the maximum outflow for Peaks 1 - 5 that produces minimal downward skewing is determined, as shown in Table 3.3.6. These new Test-4 q values can be used with the Test-3 q values shown in Table 3.3.5 to obtain new h values using Equation (3), also shown in Table 3.3.6.

Table 3.3.6. Comparison of h values obtained from Test 1/Test 2 Multi-Rate Analysis with those obtained from the requirement that there be minimal downward skewing for Test 4. T values and q values for quiescent conditions corresponding to the latter h values are also shown.

Peak No.	Depth (m)	h from Test 1/Test 2 Multi-Rate Analysis (m)	q_4 predicted from h for Test1/Test2 (mL/min)	maximum q_4 for minimal skewing in Test 4	h for minimal skewing (m)	T for minimal skewing (m²/s)	q for $h_D = 0$ (mL/min)
1	1243	-39	-12.7	-2.6	-24	3E-09	-4.4
2	1214	-46	-16.3	-3.4	-36	2E-09	-4.6
3	697	-42	-42.5	-8.7	-29	8E-09	-13.4
4	553	-48	-1.9	-0.4	-42	2E-10	-0.5
5	508	-48	-1.9	-0.4	-42	2E-10	-0.5
6	338	48*	1.6**	1.6	48	5E-10	1.3
7	288	11	3.4	3.4	11	3E-09	1.8

*from Test 3/Test 4 Multi-Rate Analysis
**fit from Test 4 peak
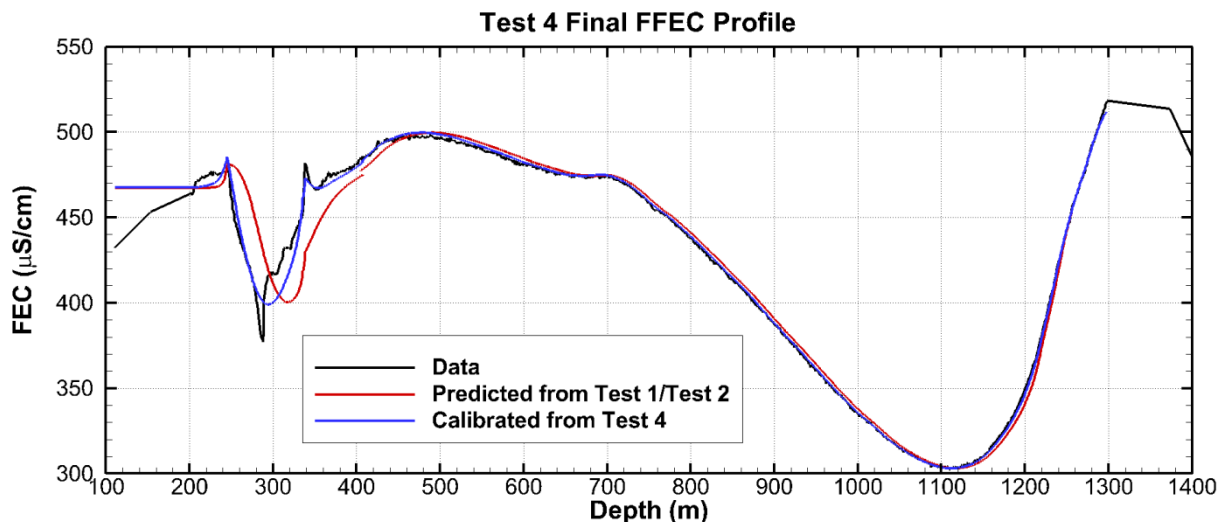
Figure 3.3.14. BORE II fit to final FFEC profile for Test 4. If the *h* values obtained from the Test 1/Test 2 Multi-Rate Analysis are used to predict the outflows for Peaks 1 - 5 for Test 4, the downward skewing is too great (red curve). Decreasing the outflow for Peaks 1 - 5 until downward skewing is minimal (blue curve) yields modified *h* values.

As a final consistency check, these new *h* values should not produce any visible downward skewing under quiescent conditions ($h_D = 0$). The *q* values for $h_D = 0$ are shown in Table 3.3.6.; using them in a BORE II simulation produces minimal downward skewing. The positive *h* values for Peak 6 and Peak 7 produce inflow when $h_D = 0$, but the rates are small enough to not produce distinctive peaks.

In summary, the main value added from the analysis of Test 3 and Test 4 is to provide additional information on the negative *h* values of Peaks 1 - 5. Because these negative head values produce inflow to the borehole when drawdown is large and outflow to the formation when drawdown is small, the wide range of drawdowns from Test 1 to Test 4 produces very different FFEC profiles, enabling better constraint of the *h* values. Additionally, Test 3 and Test 4 enable a quantitative Multi-Rate Analysis of Peak 6 to be done. Finally, the non-standard behavior of Peak 7 indicates that the parameters obtained for it are not well constrained.

3.3.8   Discussion

Table 3.3.5 indicates that all the zones below 500 m depth have negative *h* values. By definition (Tsang and Doughty, 2003) the transmissivity-weighted sum of all heads must be zero, thus shallower heads must be positive. The shallowest two peaks analyzed yield positive *h* values, and the high baseline FEC values for the depth range 100-250 m (Figures 3.3.5 and 3.3.6) are consistent with positive *h* values, since positive *h* results in inflow to the borehole during non-pumped conditions. This distribution of decreasing *h* with depth indicates downward flow under natural conditions, which makes sense for the mountainous terrain.

Tables 3.3.3, 3.3.5, and 3.3.6 show *h* and *T* values inferred from various Multi-Rate Analyses. Some indication of the uncertainty in *h* and *T* can be obtained by comparing these values, as shown in Figure 3.3.15. Another source of uncertainty in *T* is the value of r_{out} used in Equation (3.3.2.2). Increasing the assumed value of r_{out} from 48 to 4.8 m results in a modest decrease in *T* by a factor 1.5, which is relatively small compared to the range of *T* shown in Figure 3.3.15. The different symbols provide

reasonable uncertainty bounds for Peaks 1 – 6, but for Peak 7 the uncertainty should be even larger, due to the inability to quantitatively fit the FFEC profiles of Peak 7 during Test 3 and Test 4.

The independent results from an analysis of Test 1 data by Tsang et al. (2016) are also shown in Figure 3.3.15. Since their analysis considered only one test, they could not do a Multi-Rate Analysis, and they assumed all hydraulically conductive zones had the same hydraulic head, $h = 0$. For the deep peaks with negative h, Equation (1) indicates that assuming $h = 0$ would result in too strong a driving force for flow, and thus yield too low a value of T. For Peak 6 with positive h, the opposite would be true. While this trend is apparent in Figure 3.3.15 the T values obtained by Tsang et al. (2016) are generally close to the range of values obtained by the present Multi-Rate Analysis.
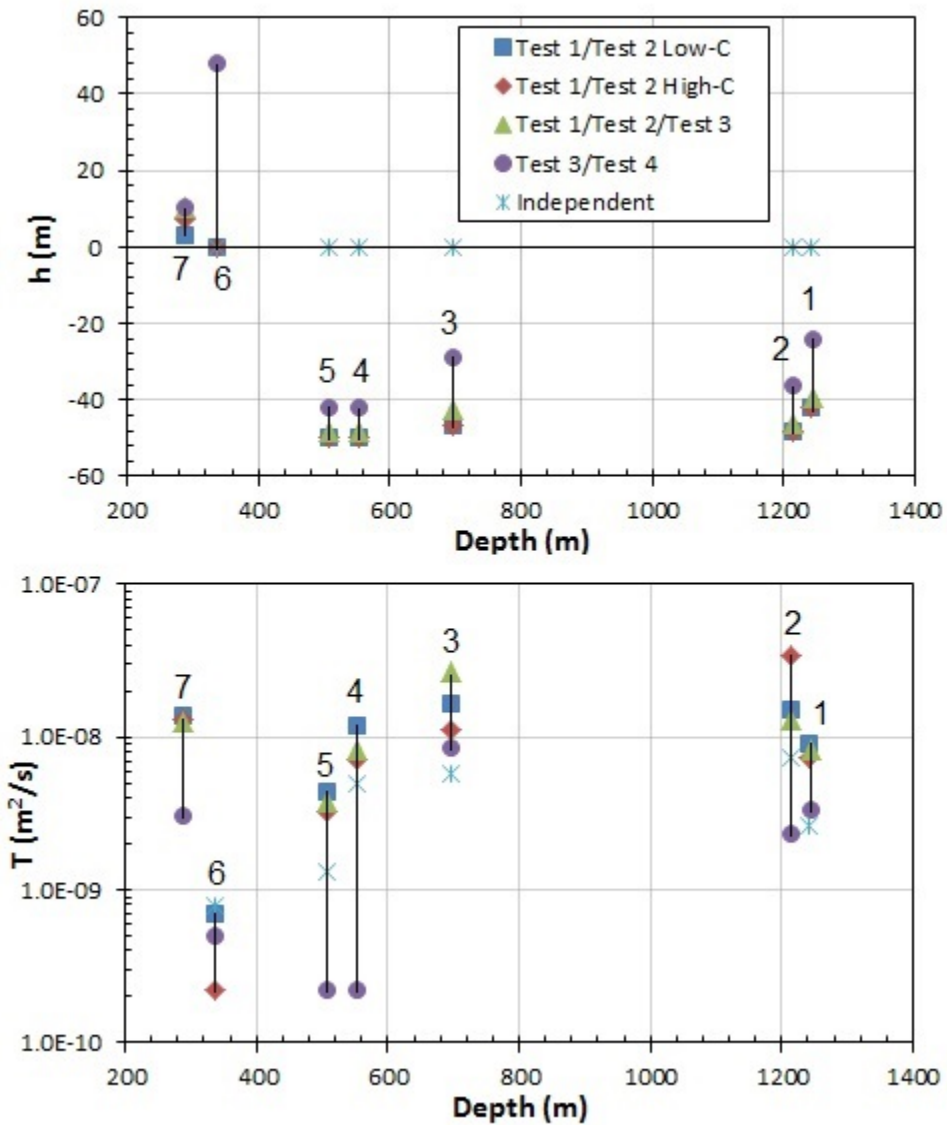
Figure 3.3.15. The h and T values obtained from various Multi-Rate Analyses. Independent results from Tsang et al. (2016) are also shown for comparison.

Analyzing FFEC logs obtained during a one-day break during drilling is challenging for a number of reasons, as enumerated below. Each of these challenges has been addressed in the present study, leading to a corresponding lesson learned, and these lessons learned may be useful for future application and analysis of FFEC logging.

Challenge 1: The time available for logging is limited, meaning few profiles can be obtained. The key information in FFEC logging analysis comes from changes between successive profiles, and there is always noise in the data, so obtaining multiple successive profiles is optimal for getting a clear signal. Furthermore, when inflow rates are small, peaks in the FFEC logs are small and symmetric. That is, there is little or no peak skewing up the borehole in the short time available for logging, which means it is difficult to determine inflow rate q and flow zone salinity C for each peak independently.

Lesson 1: The fact that few profiles are available means it is easier to fit the FFEC logs, and hence there is greater uncertainty associated with the returned parameters for inflow rate q and salinity C for each hydraulically conductive zone. The lack of peak skewing also makes the determination of q and C independently subject to greater uncertainty. These difficulties can be addressed by doing the fitting twice, with different constraints on C. This exercise provided a measure of the uncertainty of C, which could be used to estimate the uncertainty of flow-zone transmissivity T. Significantly, in this case the same values for the hydraulic head h of the flow zones were obtained with the different C constraints, greatly increasing confidence in the validity of the results and the robustness of the Multi-Rate Analysis method.

Challenge 2: Washing out the borehole prior to FFEC logging is not as well-controlled an operation as borehole water replacement, especially in the case of conductive fractures having different hydraulic heads, which could have two adverse consequences. First, borehole fluid may enter the flow zones during washing out; it returns to the borehole during logging while pumping, thus early-time logs do not represent formation fluid. Second, the baseline profile does not reflect internal flow in the borehole under non-pumped conditions.

Lesson 2: Baseline FEC profiles that result from poorly controlled washing out of the borehole can be used as initial conditions for FFEC logging, if they represent steady conditions in the borehole. Their use complicates the analysis, requiring detailed fitting instead of the simpler Mass Integral Analysis to infer the qC product of each peak. For data analysis a t_0 value is introduced for each inflow zone to mark the onset of formation fluid entering the borehole, and it turned out that the t_0 values were not difficult to estimate from the data for properly executed FFEC logging tests. On the other hand, having different baseline levels of FEC may enable identification of the salinity of inflow zones that are close to the FEC baseline values.

Challenge 3: Because of the short time available for testing, it may not be possible to determine the optimal pumping rate to use during logging, resulting in a variable pumping rate, which makes FFEC log analysis much more difficult.

Lesson 3: For the highly variable pumping rates used, a perfect match to all aspects of all profiles cannot be expected, and the totality of the logging operations must be taken into account in choosing what to emphasize in the fitting process. For this reason, it is important to measure drawdown and pumping rate throughout the FFEC logging operation. The short duration of FFEC logging during drilling requires that the available time be used as efficiently as possible, which can be expedited by doing a preliminary analysis of the data in real time. Monitoring FFEC peak growth or lack thereof can determine whether or not additional profiles should be obtained. Monitoring drawdown and pumping rate can determine optimal values to select. A very feasible solution of the problem is to use three different one-day breaks in the drilling schedule: the first to establish the optimal pumping rate to use

and to monitor how long it takes for drawdown to stabilize to determine the timing of profiles; the second for logging at $h_{D1;}$ and the third for logging at $h_{D2} \sim h_{D1}/2$. This three one-day FFEC logging testing procedure during drilling is highly recommended.

The above points show, on the one hand, lessons learned for an effective analysis of FFEC logging data during drilling, and on the other hand, lessons learned for improving the procedure for the one-day FFEC testing, such as better control of pumping rate and maximizing the drawdown value with the proper positioning of the pump in the borehole. Many of the improvements for field test procedures should be possible to accomplish without much trouble. The overall lesson is that with careful planning and thoughtful execution, much useful information can be obtained from FFEC logging, even when logging is conducted during drilling.

3.3.9   Summary and Conclusions

The FFEC logging-during-drilling tests, Test 1 and Test 2, and follow-up tests, Test 3 and Test 4, produced key information about the hydraulically conductive features intercepting COSC-1 borehole between 250 m and 2000 m depth. Seven hydraulically conductive zones were identified, each localized over a small depth zone, suggesting that they are individual fractures. Flow rate q and salinity C of each zone were determined by fitting the FFEC profiles for Test 1 and Test 2 independently with the code BORE II. Then a Multi-Rate Analysis was used to obtain the transmissivity T and hydraulic head h of the zones by combining results of the two tests, which were conducted with different drawdowns. Comparison with profiles obtained from Test 3, conducted with a similar drawdown, but different baseline FEC to Test 2, enabled refinement of flow zone properties. Test 4 was conducted with such a small drawdown that most peaks were absent, but Multi-Rate Analysis with Test 3 enabled estimates of the outflows from the borehole to the hydraulically conductive zones. Conducting multiple analyses and comparing the results provided estimates of uncertainty associated with the zone properties.

Compared to the previous analysis of Test 1 by Tsang et al. (2016), the present paper has made the following advances: (1) determination of a distinct h value for each hydraulically conductive zone; (2) use of different baseline FEC levels to help constrain the C values for several zones; (3) confirmation and refinement of the results of tests conducted during the drilling period by follow-up tests conducted a year later; and (4) joint re-analysis of data from all four tests, considering distinct h values, to provide the most constraints possible on the results.

All the inferred fracture properties – flow rate, salinity, transmissivity, and hydraulic head – varied greatly among the hydraulically conductive zones, as is typical of a poorly connected fracture network in low-permeability rock. Salinity values are relatively low and hydraulic head variability suggests downward groundwater flow; both features are consistent with the mountainous setting of the COSC-1 borehole.

Despite the challenges discussed in the previous section, useful and critically important information from FFEC logging during one-day breaks in drilling was obtained, with no impact on the drilling schedule and at minimal cost, as all the equipment needed was already available on site as part of the drilling operation. The most basic information obtained is the depth of hydraulically conductive zones, which can be determined very accurately, typically within 10 centimeters, assuming that the depth value has been properly calibrated against other geophysical logging data. Given that the vast majority (about 97%) of fractures observed in core and logs are non-conductive, identifying the conductive features is of utmost importance, both for its own sake and to guide deployment of further borehole characterization techniques such as fluid sampling and packer tests.

Next, inflow and outflow rates from the conductive zones and salinity of the formation fluid can be determined with reasonable accuracy by calibrating against BORE II models, which are also very useful information for designing further characterization studies. Finally, combining tests with different applied

drawdowns enables estimates of the hydraulic head and transmissivity of individual fractures. There is greater uncertainty associated with these estimates, but they are data not easy to obtain in any field tests and are critically valuable for understanding the overall pattern of groundwater flow through fractured rock.

Given the high value of the information that can be obtained, and the relative ease of conducting the tests, it is strongly recommend that FFEC logging during drilling be considered whenever suitable breaks in the drilling schedule occur. They can provide a wealth of information on the hydrology of the fractured rock in themselves, and offer essential guidance for designing and deploying more expensive, time-consuming characterization studies to be conducted after drilling is completed. As a further recommendation, it will be most useful to conduct a post-drilling, regular FFEC logging test lasting about one-week that includes an initial replacement of borehole water. Such a test would greatly improve the accuracy of hydrologic data obtained from the deep borehole.

3.4   Core Sample Measurements

Flow in fractures in crystalline rock in the deep subsurface is governed by the aperture distribution and the head field. Measurements of transmissivity in the field have been made in a fractured rock in a deep borehole in Sweden (Collisional Orogeny in the Scandinavian Caledonides - COSC). This is a scientific deep borehole project with geologic, hydrologic, and geophysical measurement goals. The project is centered on the drilling of two deep boreholes (2.5 km each) into crystalline rock in Sweden. One of the holes (COSC-1) was drilled last year and another (COSC-2) will be drilled in 2017. Core was collected from the first borehole over almost the entire borehole depth.

The main thrust of the COSC-1 core measurements at LBNL is to determine fracture transmissivities as a function of controlled stress. Cores were taken from the COSC-1 borehole in flowing zones identified from preliminary flowing fluid electrical conductivity (FFEC) logs and selected by visual inspection for the presence of fractures. The flowing zones are found at depths from 340 m to 2380 m. Test samples are full-diameter (~3 inch), vertically-oriented cores that are approximately 8 inches long. The measurements were conducted under controlled stress conditions with fluid delivery and collection customized to directly investigate the effects of stress on fracture hydrologic behavior. These permeability (transmissivity) measurements are compared with in-situ fracture transmissivities based on detailed FFEC logging. Because the direction of the head field was unknown, a unique multi-directional permeability apparatus was constructed.

3.4.1   Experimental design

Core samples obtained from COSC were to be minimally changed during our tests. In addition, the transmissivities were to be measured over a range of effective stresses. To honor these requirements, we constructed a custom apparatus (Figure 3.4.1) allowing us to deliver water to any of four inlets distributed at 45 degree increments along the surface, and to extract water from an outlet opposite to the inlet. The inlets and outlets are half-tubes that run along the length of the core insuring contact with the fracture.
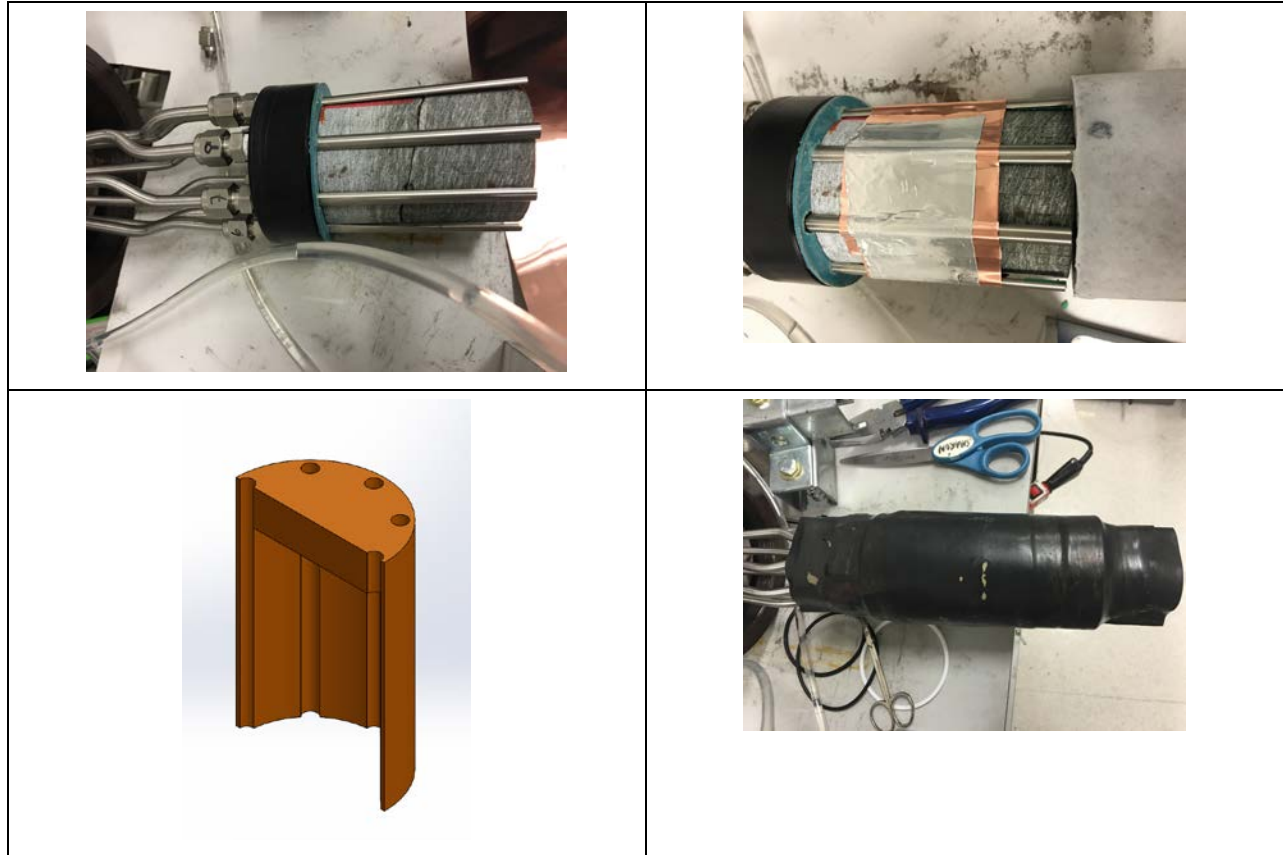
Figure 3.4.1. Apparatus internal assembly. Top left – both pieces of the fractured core are placed in between the water inlets and outlets. Top right – Thin metal strips are wrapped around the region containing the fracture to keep the rubber sleeve from flowing into the aperture at elevated confining pressure. Bottom left – Cut-away schematic of the custom silicone rubber sleeve that the rock core and inlets are placed in. Bottom right – view with outer sleeve in place.
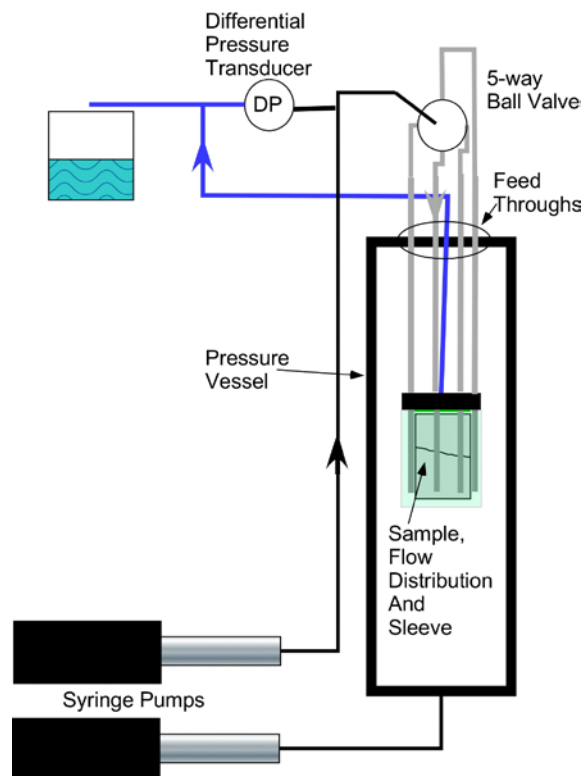
Figure 3.4.2. System schematic. Confining pressure is controlled by the lower syringe pump, and the upper syringe pump flows water through the sample. Two 5-way ball valves (one shown) control flow to the inlet and outlet tubes.

A custom silicone rubber sleeve (Figure 3.4.1) was manufactured to fit around the core and inlet and outlet tubes to inhibit flow around the core. This sleeve was cast over a mockup of the setup to provide the proper fit. The top inlet and outlet support is a solid Delrin (a hard plastic) puck with holes to hold the inlet and outlet tubes on one side, and national pipe thread (NPT) fittings on the other. One-quarter inch stainless steel tubes were connected to the NPT fittings, and these were run through feed-throughs on the pressure vessel cap (Figure 3.4.2). Outside the pressure vessel, each tube was connected to a pressure relief valve, and then to a five-way ball valve. A solid hockey puck-shaped Delrin disk was placed at the bottom of the sample and sleeve, and a thin Viton sleeve was placed over the entire assembly to inhibit leaks into the assembly from the confining fluid. The assembly shown in Figure 3.4.1 is placed in a pressure vessel (High Pressure Equipment Company TOC-31-20) having an inside diameter of about 4 inches, an inside length of 20 inches and a rating of 5000 psi. Effective stresses exceeding 5000 psi would require use of a different vessel. A high-pressure precision syringe pump (Quizix Q6000) connected to a pressure port on the bottom of the pressure vessel was used to provide controlled confining pressure.

Flow through the fracture was driven using another precision high-pressure syringe pump (Quizix Q6000), although flow pressures were kept below 30 psi. Flow was regulated through two 5-way ball valves (inlet tube and 4 outlets), and the pressure difference between the inlet and outlet was measured using a Rosemount 3051 differential pressure transducer, with output measured using a Keithley 2701 digital multimeter, and recorded to a computer using Excelinx software.

Measurements were made across each of the four pathways (1-5, 2-6, 3-7, 4-8) for a number of flowrates over a range of confining pressures, from 200 psi up to 4,500 psi, corresponding to depths of about 61 meters to about 1370 meters. For a set of tests, a pathway was selected, and the confining pressure was

set. Flow would be applied at three different rates, and measurements would be taken every 10 seconds until they reached a stable value (about 60 seconds). Since the applied flowrates resulted in low pressures, the confining pressure can be assumed to be the effective stress on the sample and no correction is needed for the pore pressure.

3.4.2 Transmissivity measurements

Transmissivity measurements were completed on two of the fractures -– Samples 211-2 and 188-4. Both were chosen because the diameter and length fit well in the system geometry. Flow was directed through the designated flow paths as controlled by the valve position, and pressure differential across the fracture was recorded. For each confining pressure and flow path, differential pressure was measured using three different flow rates. When all the flow paths had been measured at one confining pressure, the confining pressure was raised or lowered to a new confining pressure set point and the process repeated. Transmissivity was calculated using the following relationship.

$$Transmissivity \ (m^2/s) = \frac{Qg\rho l \Delta l}{\Delta P} \tag{3.4.2.1}$$

where Q = volumetric flow rate, g = gravity, ρ = density, l = fracture length, P = pressure. Equation 3.4.2.1 assumes a planar rectangular fracture with fluid distributed across the inlet and outlet (Figure 3.4.3). Our geometry is different, in that water is applied over a finite region on opposite sides of an elliptical fracture. In the cases we looked at, our ellipse was nearly circular. We corrected the relationship using the solution to a similar electrical resistance problem across a disk with finite sized electrodes (McDonald, 2000).
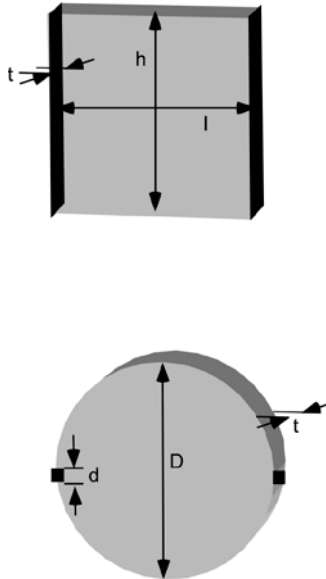
Figure 3.4.3. Fracture geometries used in the analogy.

For the rectangular case (Figure 3.4.3 top), the resistance across the volume is:

$$R_s = \frac{l}{\sigma * t * h}$$
(3.4.2.2)

and the conductance is:

$$C_s = \frac{\sigma * t * h}{l} \qquad (3.4.2.3)$$

where R is resistance, l is length, $\square$ is resistivity, circular case (Figure 3.4.3 bottom),

$$R_c = \frac{2}{\pi * \sigma * t} \ln \frac{2d}{D} \qquad (3.4.2.4)$$

and the conductance is

$$C_c = \frac{\pi * \sigma * t}{2 * \ln \frac{2d}{D}}$$
(3.4.2.5)

Letting l=h and dividing

$$\frac{C_c}{C_s} = \frac{\pi}{2\ln\frac{2d}{D}} \qquad (3.4.2.6)$$

To account for the geometric difference between the circular and rectangular geometry, we modified Equation 1 to

$$Transmissivity \ (m^2/s) = \frac{C_c}{C_s} \frac{Qg\rho l \Delta l}{\Delta P} \qquad (3.4.2.7)$$

Figures 3.4.4 and 3.4.5 show the measured transmissivities for the two fractures over the range of effective stresses. For the first fracture that was put into the system, 188-4 (Figure 3.4.3), the confining pressure was only able to reach 2000 psi before the sleeve failed. This was due to gaps in the rock along the fracture line from tiny pieces of rock breaking off during drilling. The confining pressure was adequate to compress the metal into the gap, but a larger void allowed the metal and sleeve to break. Lines in the plot show the average values of the data for each flow path. There was some variability in the measured transmissivity with flow path but no strong trend with confining pressure.

For Sample 211-2 (Figure 3.4.5), a new sleeve was made and gaps along the fracture line were carefully filled in with a non-destructive epoxy cement, as well as reinforcement from a metal strip. For this core the confining pressure was able to reach a maximum of 4500 psi – the maximum intended pressure for the tests. Fracture 211-2 also showed changes in transmissivity up until 2000 psi, where the values appeared to stabilize. It is interesting to note that in both cases, two of the values seem to increase (1-5 and 4-8 for Sample 188-4, and 3-7 and 4-8 in Sample 211-2), and two decrease (2-6 and 3-7 for Sample 188-4 and 1-5 and 4-8 in Sample 211-2). Additionally, the increasing and decreasing pairs are adjacent. Although insufficient data have been collected to be conclusive, this is consistent with data in crystalline rock under shear (Gentier et al. 1997).
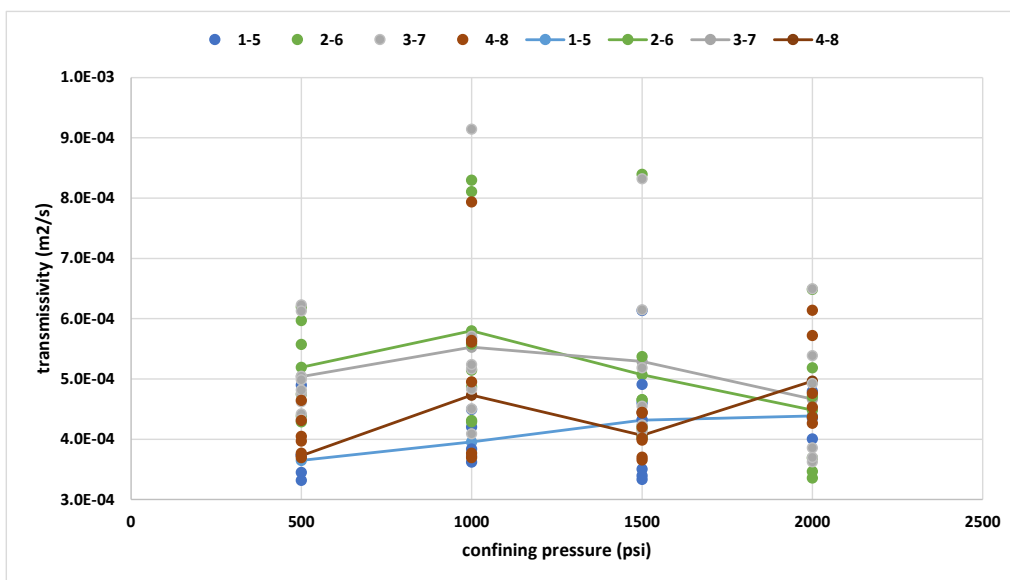
Figure 3.4.4. Transmissivity of fracture 188-4. Lines connect average values for transmissivity for the defined conditions.
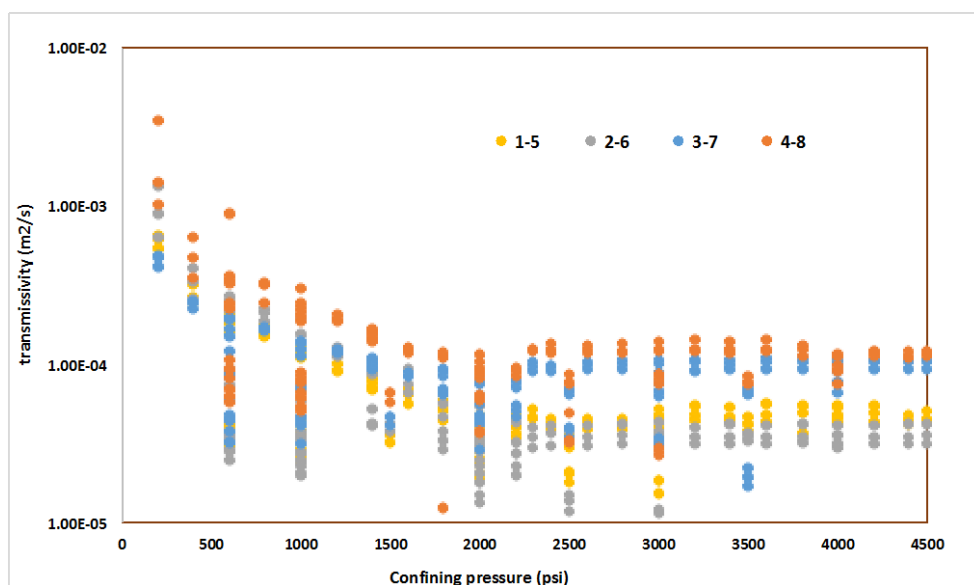
Figure 3.4.5. Transmissivity of fracture 211-2.

3.4.3   Aperture Distributions

The fractured cores were CT scanned using a modified GE Lightspeed medical X-ray CT scanner to get a better understanding of fracture geometry and to estimate aperture distribution. Because the fractured samples had to be removed from the pressure vessel to complete the scans they were performed without applied confining pressure.

Figure 3.4.6 (a) is a top down view of the core showing the flow channels located around the circumference showing and Figure 3.4.6 (b) show the cross sections of the channels lined up down the core.

Fracture apertures were computed from the X-ray CT data. Because of the heterogeneity of the rock, the standard Missing Mass Method could not be used because the fundamental assumption is the rock is uniform. To rapidly assess the aperture, X-ray CT values corresponding to the aperture were segmented out and the Missing Mass Method was applied to the resulting data. This approach results in a more stair-step aperture than actually exists, however does provide an understanding of the potential flow paths. Estimates of fracture aperture distributions are shown in Figures 3.4.7 and 3.4.8. Values range from 0 to almost 2 mm.

Comparison of transmissivity and fracture aperture distributions
A comparison between the aperture structure and the resulting changes in transmissivity with direction was performed. In Figure 3.4.7, the aperture distribution of Sample 211-2 is shown. The segmentation induced artifacts highlight real aperture distribution showing a structure in which aperture changes are stronger (higher gradients) leaning about 10 degrees to the right, and less strong in the perpendicular direction. The strong (high gradient) changes, are roughly along the 3-7, 4-8 direction, and the lower gradient changes are along the perpendicular 1-4 and 2-5 direction. As was noted above, the higher transmissivity direction at elevated stress correlates to the 3-7 and 4-8 direction.

In sample 188-4, the high gradient direction (Figure 3.4.8) leans about 45 degrees to the right, correlating to the 4-8 and 1-5 direction. This has been noted previously as the direction that tends to increase in transmissivity with increasing effective stress. Thus, in both samples, the transmissivity tends to increase perpendicular to the apparent delineations (high gradient direction) on the computed apertures.
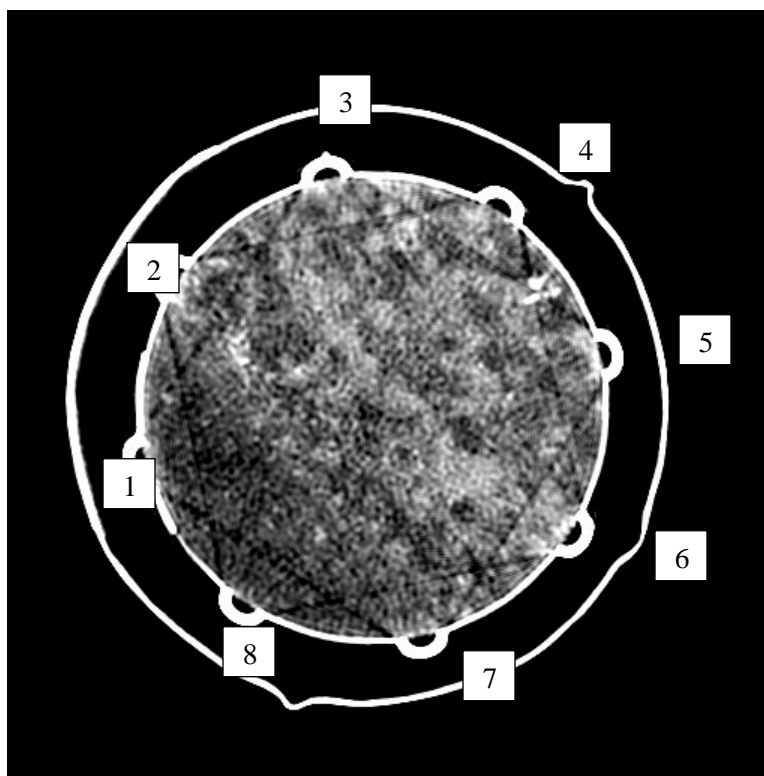
Figure 3.4.6. (a) X-ray CT cross-section of Core 188-4 with inlet and outlet channels labeled.

| Path 1 to 5 | Path 2 to 6 | Path 3 to 7 | Path 4 to 8 |
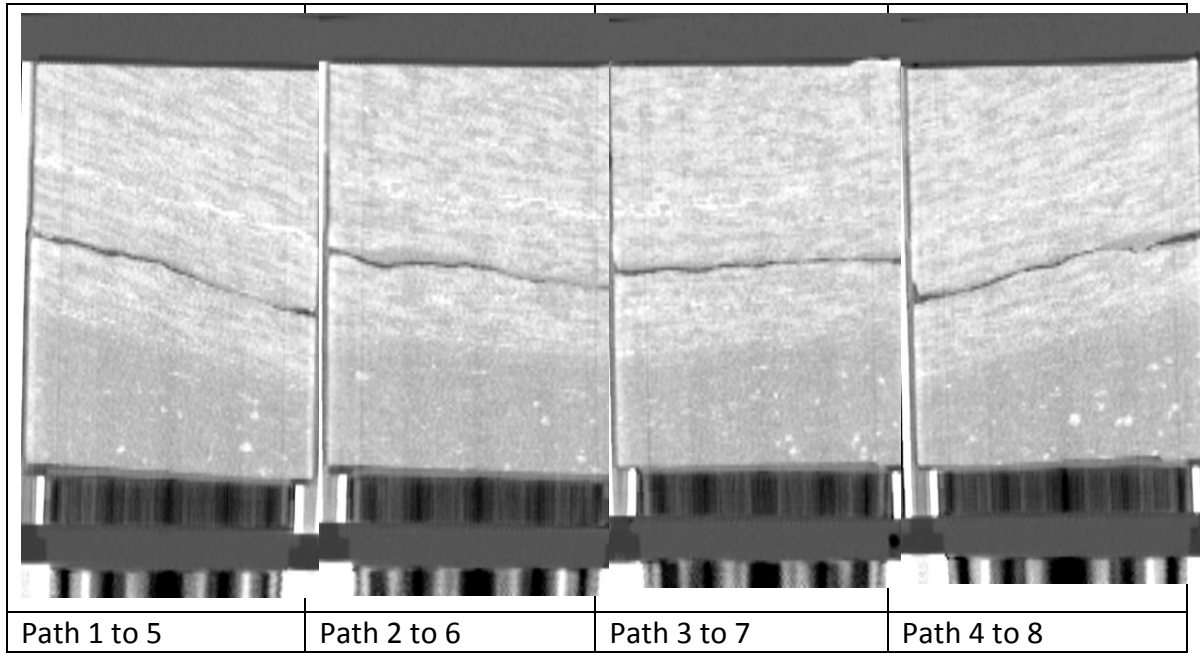
Figure 3.4.6. (b) X-ray CT cross sections of Core 188-4 visualization of the fracture for each flow channel.
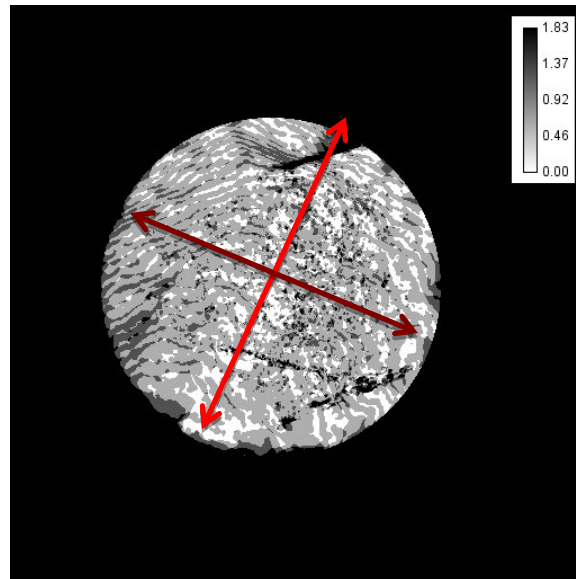
Figure 3.4.7. Aperture distribution (in mm) for the 211-2 core fracture. The high gradient direction is shown with the red arrow, and the low gradient direction is shown with the brown arrow.
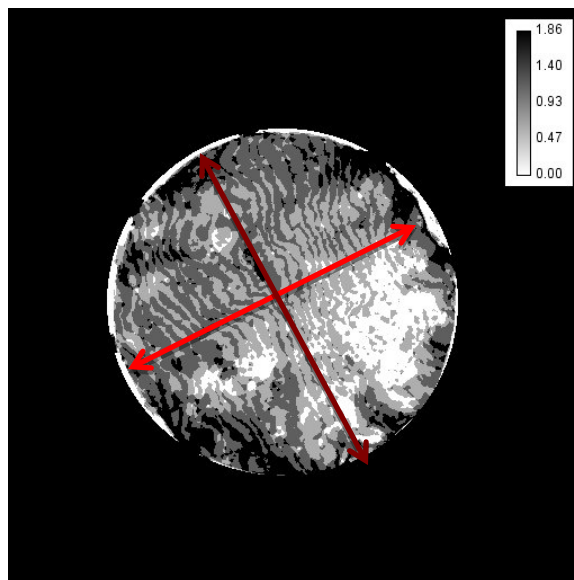
Figure 3.4.8. Aperture distribution (in mm) of 188-4 core fracture. The high gradient direction is shown with the red arrow, and the low gradient direction is shown with the brown arrow.

3.4.4   Comparison of results to FFEC analysis

Previous work described in Section 3.3 using the technique of Flowing Fluid Electric Conductivity (FFEC) estimated transmissivity estimated values from 1×10^{-8} to 1×10^{-10} m^2/s, several orders of magnitude smaller than those observed in the laboratory study. The differences in the values may be because in natural systems the asperity contacts would wear and dissolve over much longer timescales than available in the lab. Additionally, fine particles generated by rock shear or mineral precipitation can reduce the flowing aperture, reducing transmissivity. It is very difficult to recover a fractured core without damaging the fracture faces. One explanation for the difference could be that some damage-induced pathways formed on collection. Our unloaded samples were carefully reassembled to avoid damage, thus we reduced the possibility of generating fines in our setups, and our tests were performed over timescales much too short to have significant consequences from mineral dissolution and precipitation.

3.4.5   Discussion and Summary

In this work, a novel technique was developed to investigate the effect of effective stress on transmissivity. Because the cores we received were to be returned relatively undamaged, we designed a permeability measurement system that allowed for measurements in 8 directions at 45 degrees from another using one setup. Tests were performed on two fractured samples of COSC rock, at effective stresses from 200 psi to 4,500 psi. Both samples had fractures with roughly circular cross sections (perpendicular to the borehole). We expected that transmissivity would decrease with increasing effective stress. Our measurements show that in general this is true. The measurements also show, however, that the magnitudes of these changes depend on the flow direction with respect to the aperture distribution. Apertures calculated from X-ray CT data show a high-gradient direction, and a low gradient direction. Transmissivities tended to have a directional component, with transmissivities along the high-gradient direction increasing with increasing effective stress, and transmissivities along the low gradient direction decreasing with increasing effective stress. Our laboratory transmissivity measurements are much higher than field measurements. Possible reasons for this can include the wearing of asperity contacts over long times in the field resulting in smoother local surfaces and fine particles that can reduce the available aperture for flow.

3.5   Geochemical Variations of COSC-1 Water Samples

The COSC-1 well provided the opportunity to test out two different downhole water sampling techniques and see how well they corresponded with each other, and also to look for variations in fluid chemistry associated with identified inflow zones and changes in lithology. The two sampling techniques consisted of a conventional wireline downhole fluid sampler and a tube sampling method that was developed by the Geological Survey of Finland (GTK). The tube sampling was conducted using a setup depicted in Figure 3.5.1. An illustration of this method being conducted in the field is depicted in Figure 3.5.2.
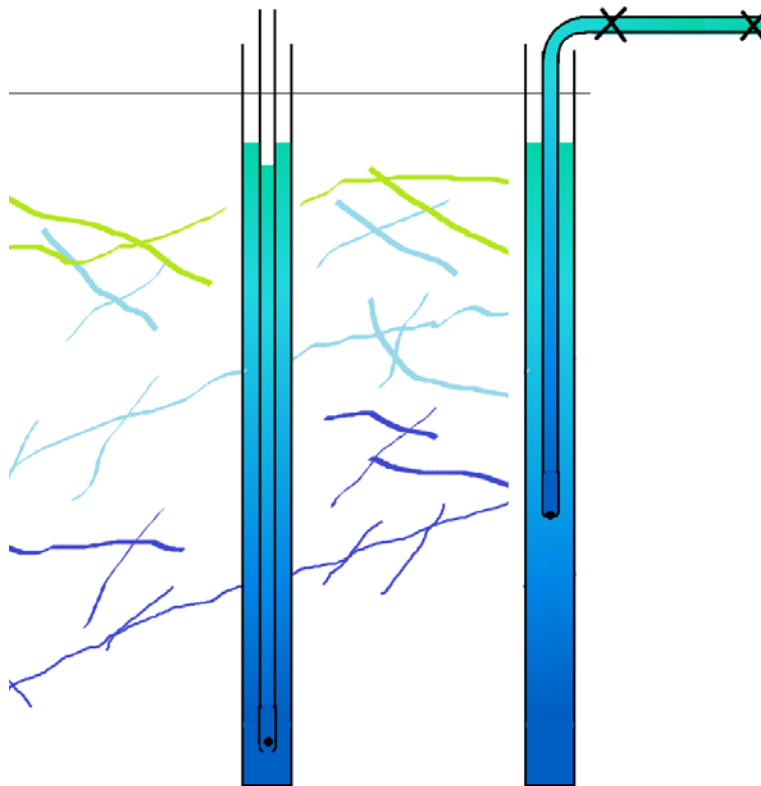
Figure 3.5.1. Schematic illustration of tube sampling method developed by the GTK for the COSC-1 well. On the left, the tube is lowered down to the bottom of the well and the bottom portion of the tube is sealed. The stratification of the water column chemistry is preserved throughout the length of the tube. On the right, as the tube is raised from the hole, individual segments are crimped off, thus isolating that section of the water column chemistry.

Figure 3.5.2. Collection of tube water samples in the field, and selected samples packaged for shipment to LBNL for analysis.

The tube sampling was collected by GTK from September 14-18, 2014, at nominal 100 m depth intervals for entire borehole using a 10 mm Inner Diameter (ID) tube; eight sub-samples (each consisting of 6 m of tubing) near the eight inflow zones from 300 to 2500 m that were identified by FFEC logging during drilling, were shipped to LBNL for microbiological analysis described in Section 3.6. The conventional downhole sampling was conducted at 6 depths in the COSC-1 well by Lund University on Oct. 2 and 5, 2015 – these intervals were also chosen to coincide with fluid entry zones identified by the FFEC logging. Both sampling techniques are designed to sample water from specific depths – the tube sampler provides the added benefits of being able to sample the entire water column and also preserve its dissolved gas component. Additional water chemistry analyses conducted on samples collected using the tube sampling method were conducted by Lasse Ahonen and Riikka Kietäväinen (GTK). Gas samples were extracted from the tubing segments, and water samples were then drained to sampling bottles for analysis. Both electrical conductivity and pH were measured on site.

Splits of the two types of water samples were shipped to Gary Andersen and Yvette Piceno of LBNL's Climate & Ecosystem Sciences Division for microbiological characterization (Section 3.6.1). For the conventional downhole samples, after the samples were filtered for the microbiological studies, the remaining water was then provided for geochemical analysis. Li Yang of LBNL analyzed the cation and anion chemistry of the water samples obtained by the downhole sampler; the stable isotope compositions of these samples were measured at the Center for Stable Isotope Biogeochemistry at University of California (UC) Berkeley. The geochemical results from the LBNL sample suite are presented in Table 3.5.1.

Table 3.5.1. Water chemistry analyses for COSC-1 water samples collected using conventional downhole sampler

Depth (m)	T °C	Li	B	Al	SiO$_2$	K	Na	Mg	Ca	Mn	Fe	Ni	Cu	Zn	As	Sr	Rb	Ba	SO$_4$	Cl	F	HCO$_3$	δ^{18}O ‰	δD ‰
248	7.95	0.0019	0.09	0.06	16.45	2.0	32	0.56	59	0.02	0.009	0.003	0.032	0.24	0.0007	0.10	0.006	0.01	178	3.3	0.3	70.66	-13.5	-95.6
339	9.73	0.0022	0.03	0.06	14.85	2.7	34	1.17	56	0.04	0.006	0.003	0.003	0.47	0.0005	0.16	0.007	0.01	139	9.5	0.4	45.19	-13.6	-96.5
552	13.87	0.0024	0.03	0.06	9.07	3.0	41	1.28	58	0.06	0.006	0.002	0.001	0.66	0.0005	0.18	0.008	0.02	152	22.2	0.5	67.30	-13.5	-95.8
699	16.65	0.0032	0.03	0.06	5.85	3.0	34	1.39	62	0.08	0.006	0.003	0.001	0.85	0.0004	0.20	0.008	0.02	144	22.8	1.2	78.59	-13.3	-93.7
1216	27.66	0.0011	0.02	0.06	3.61	1.7	10	0.99	64	0.12	0.007	0.004	0.004	1.77	0.0004	0.27	0.007	0.03	118	16.7	0.2	59.02	-12.3	-86.5
1244	28.08	0.0009	0.02	0.06	3.73	1.8	10	1.05	78	0.13	0.010	0.004	0.002	2.17	0.0003	0.31	0.008	0.03	144	16.8	0.2	57.24	-12.2	-85.7
drilling water		bd	bd	0.01	2.97	bd	2.4	0.56	14	0.01	0.06	0.001	0.003	0.006	0.00005	0.04	0.002	0.01	3.6	1.9	bd	na	-12.0	-85.8

Concentration data in ppm. bd – below detection. na – not analyzed. Stable isotope data reported respective to V-SMOW standard. Analysis of stream water used for drilling at COSC-1 courtesy of Riikka Kietäväinen (GTK). Temperature data from COSC-1 thermal profile at corresponding sample depths taken from Lorentz et al. (2015b).

Plots comparing the results of the tube samples analyzed by GTK and the downhole sampler analyzed by LBNL are presented in Figures 3.5.3 to 3.5.13. The composition of the surface water supply used for drilling is shown for comparison.
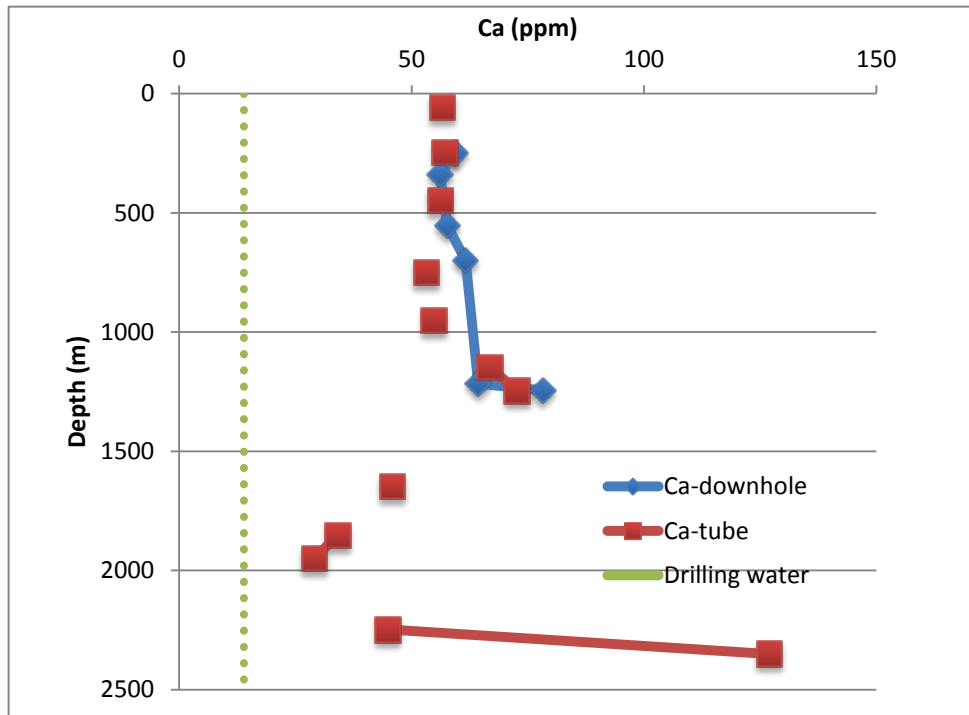
Figure 3.5.3. Comparison of COSC-1 Ca concentrations in water obtained from downhole sampler analyzed by LBNL and tube sampler analyzed by GTK. Drilling water shown for comparison.
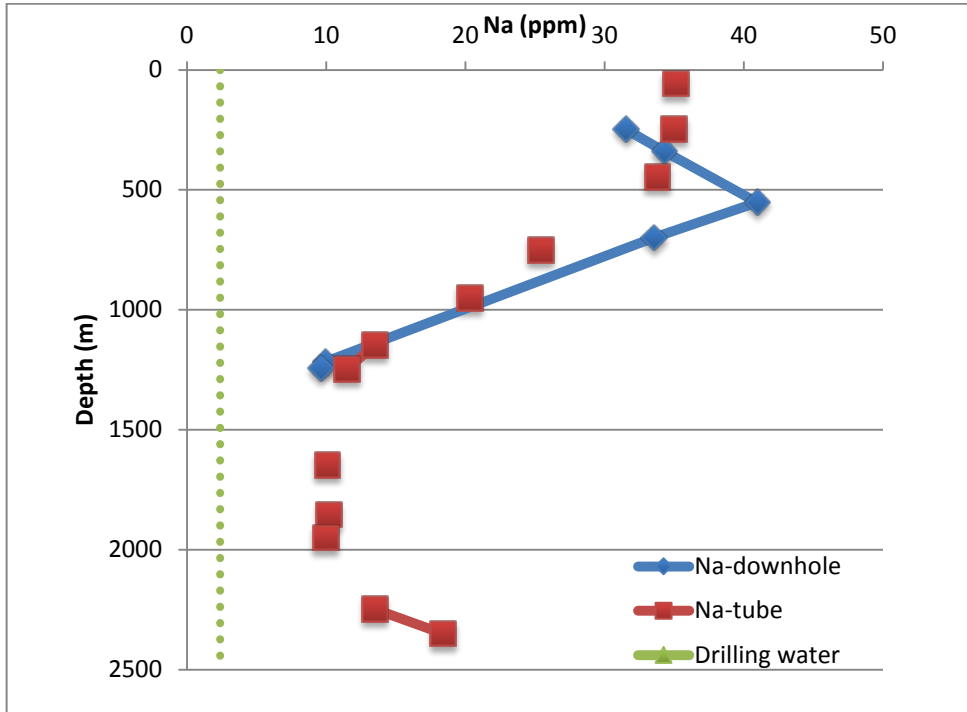
Figure 3.5.4. Comparison of COSC-1 Na concentrations in water obtained from downhole sampler analyzed by LBNL and tube sampler analyzed by GTK. Drilling water shown for comparison.
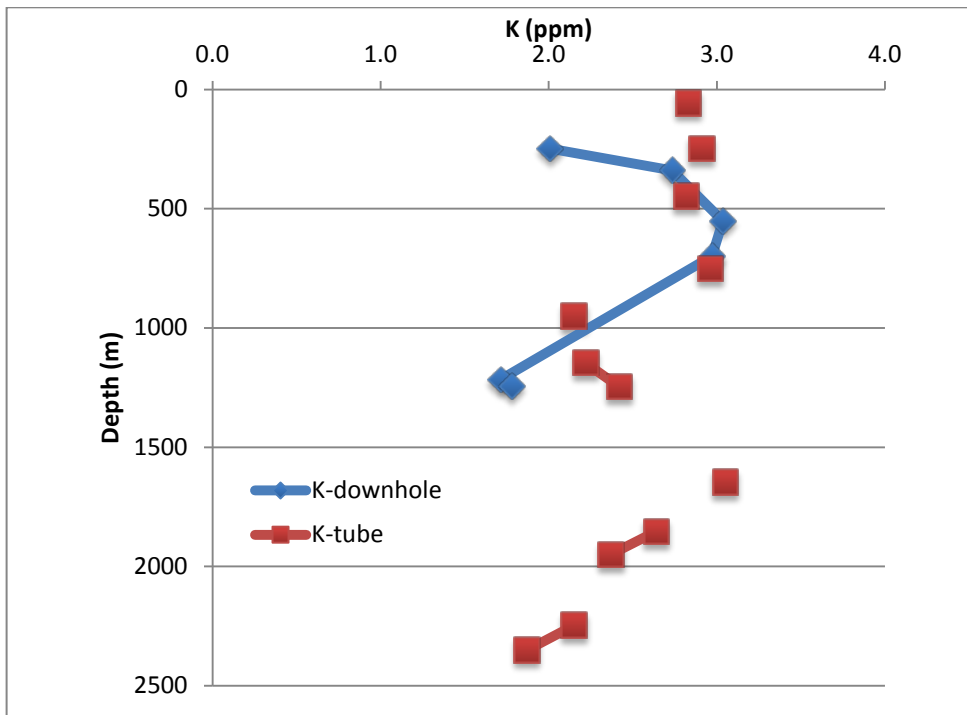
Figure 3.5.5. Comparison of COSC-1 K concentrations in water obtained from downhole sampler analyzed by LBNL and tube sampler analyzed by GTK.
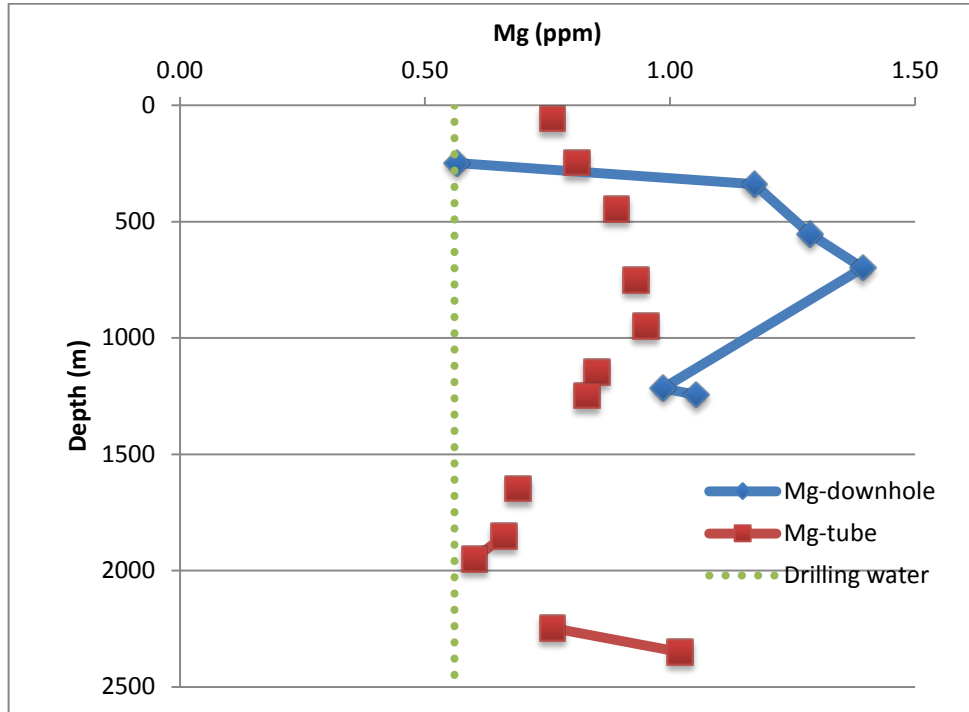
Figure 3.5.6. Comparison of COSC-1 Mg concentrations in water obtained from downhole sampler analyzed by LBNL and tube sampler analyzed by GTK. Drilling water shown for comparison.
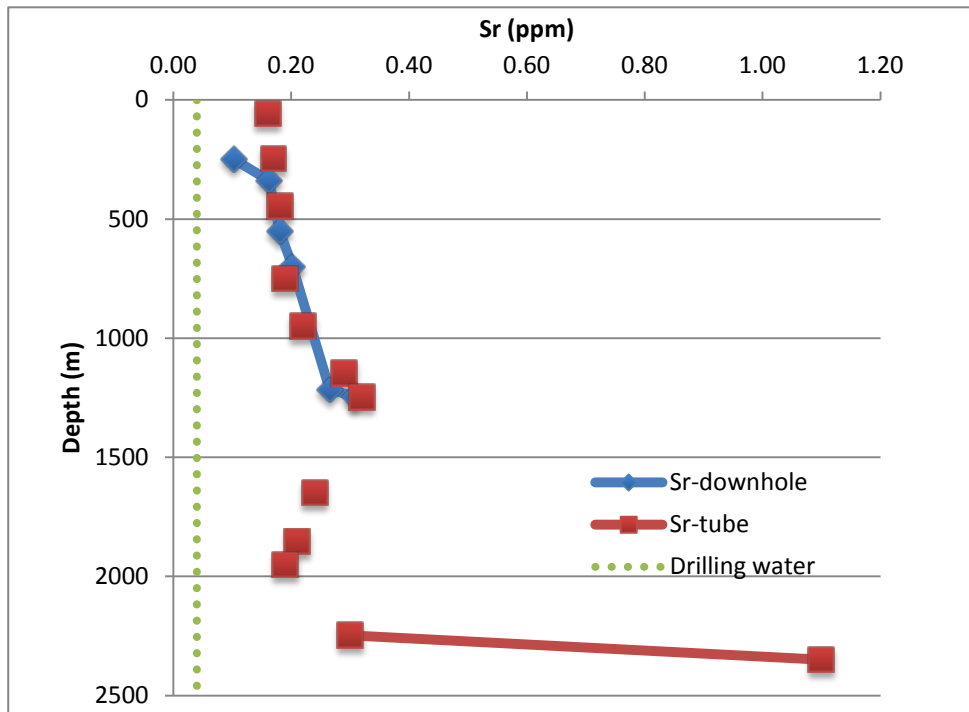
Figure 3.5.7. Comparison of COSC-1 Sr concentrations in water obtained from downhole sampler analyzed by LBNL and tube sampler analyzed by GTK. Drilling water shown for comparison.
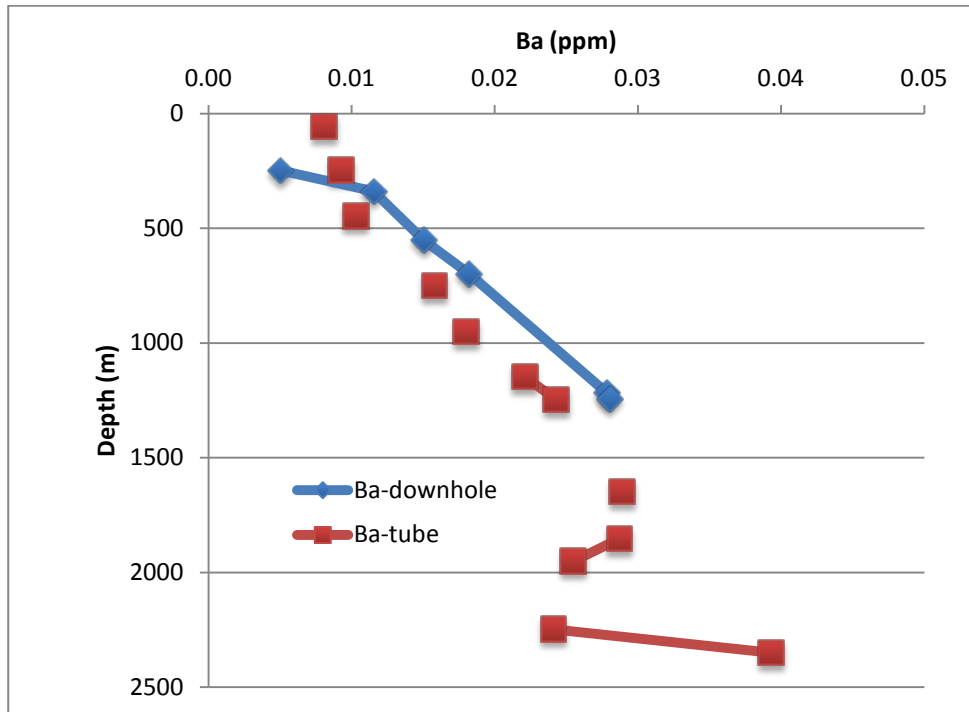
Figure 3.5.8. Comparison of COSC-1 Ba concentrations in water obtained from downhole sampler analyzed by LBNL and tube sampler analyzed by GTK.
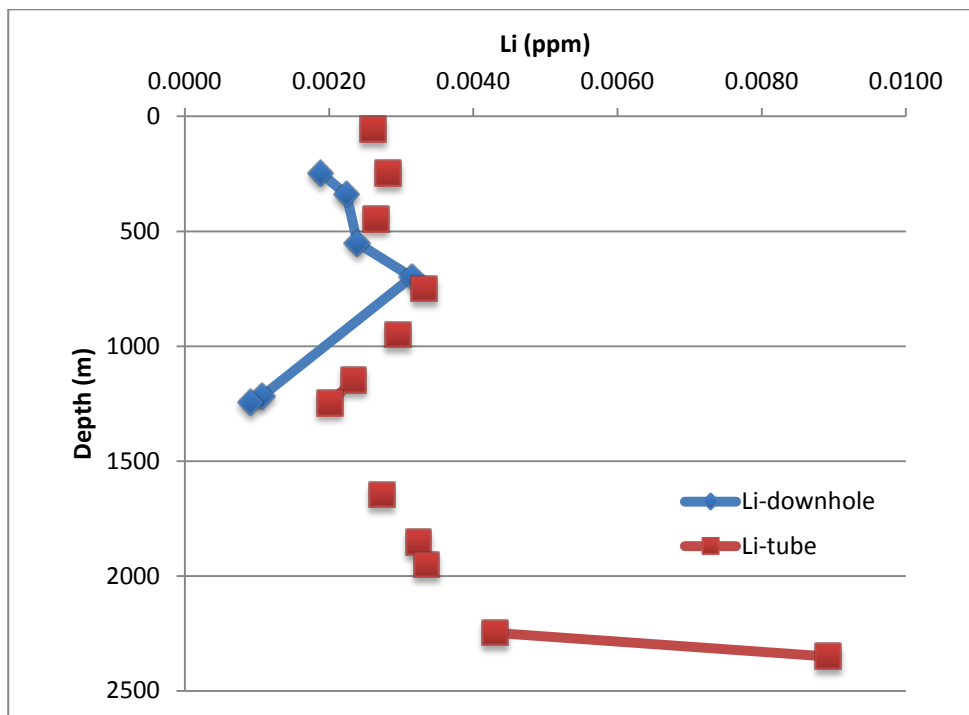
Figure 3.5.9. Comparison of COSC-1 Li concentrations in water obtained from downhole sampler analyzed by LBNL and tube sampler analyzed by GTK.
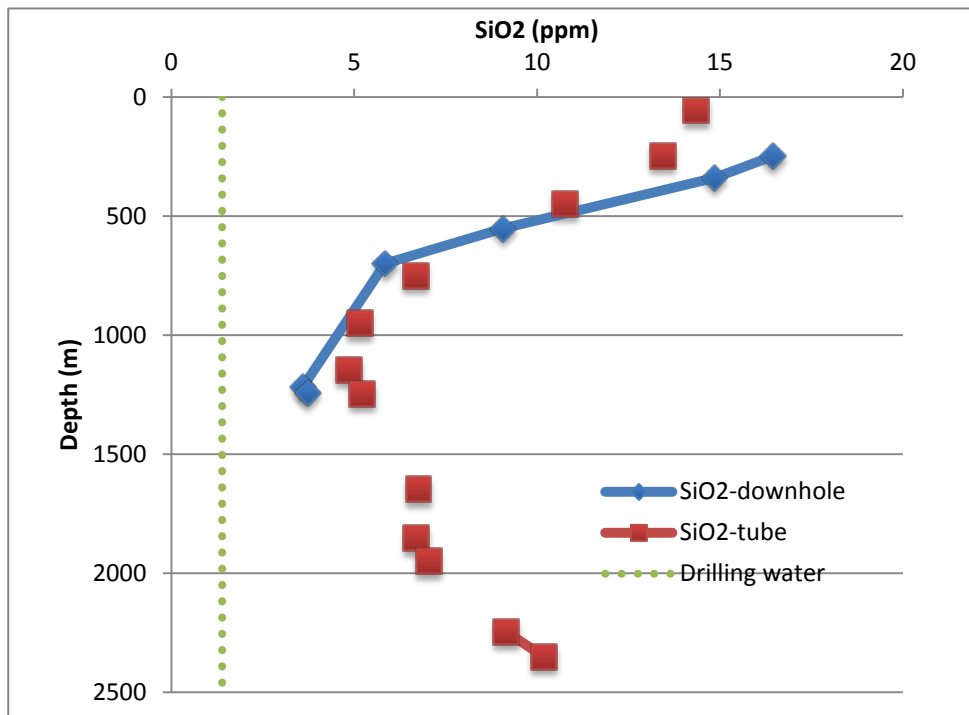
Figure 3.5.10. Comparison of COSC-1 SiO_2 concentrations in water obtained from downhole sampler analyzed by LBNL and tube sampler analyzed by GTK. Drilling water shown for comparison.
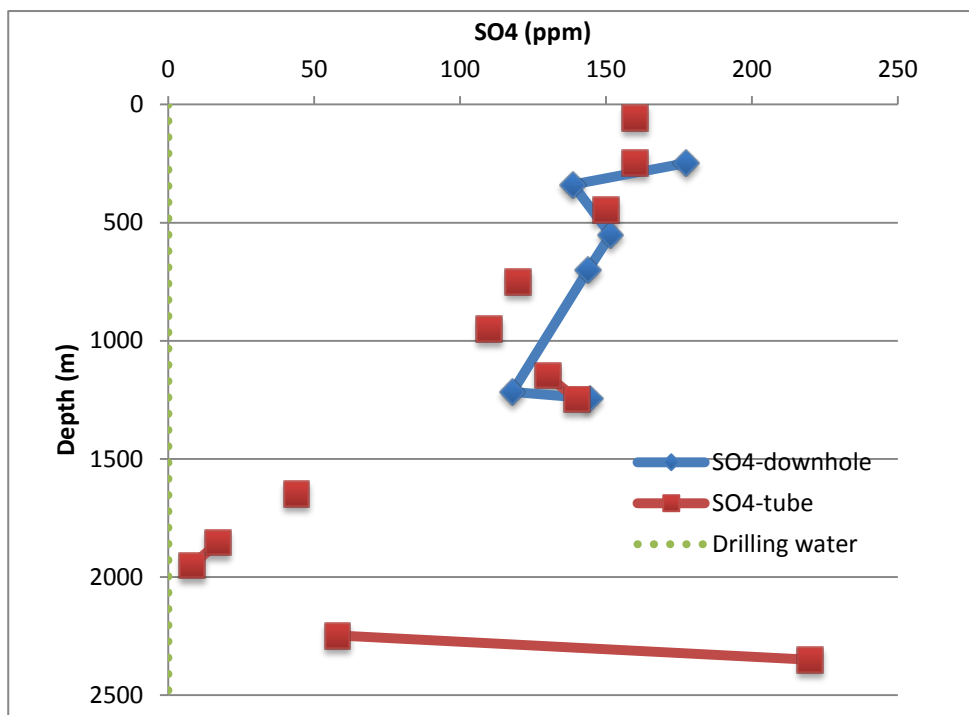
Figure 3.5.11. Comparison of COSC-1 SO_4 concentrations in water obtained from downhole sampler analyzed by LBNL and tube sampler analyzed by GTK. Drilling water shown for comparison.
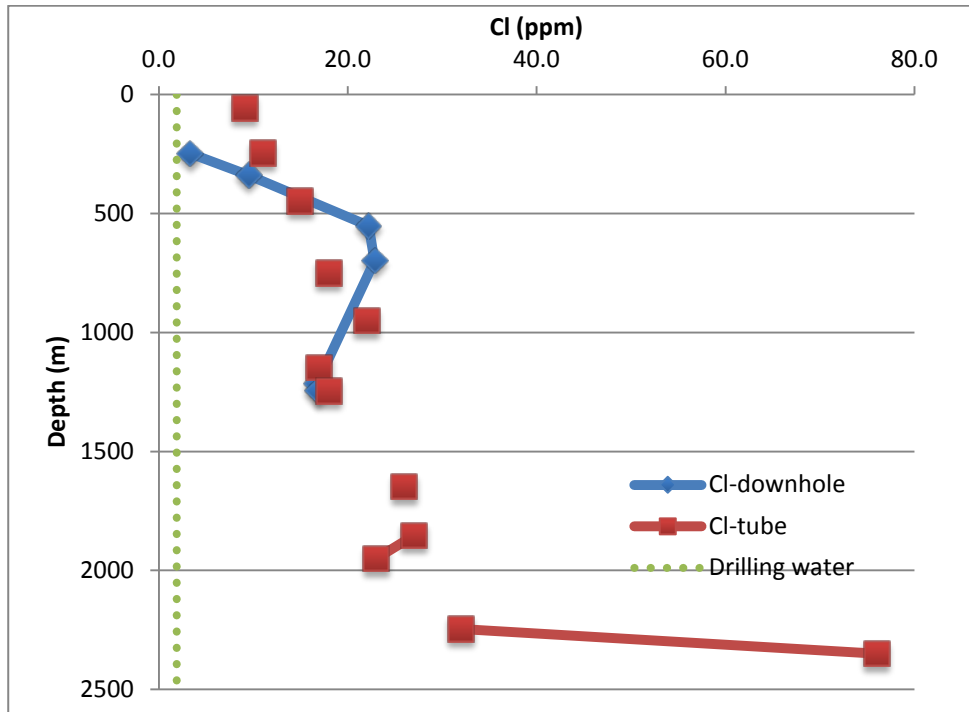
Figure 3.5.12. Comparison of COSC-1 Cl concentrations in water obtained from downhole sampler analyzed by LBNL and tube sampler analyzed by GTK. Drilling water shown for comparison.
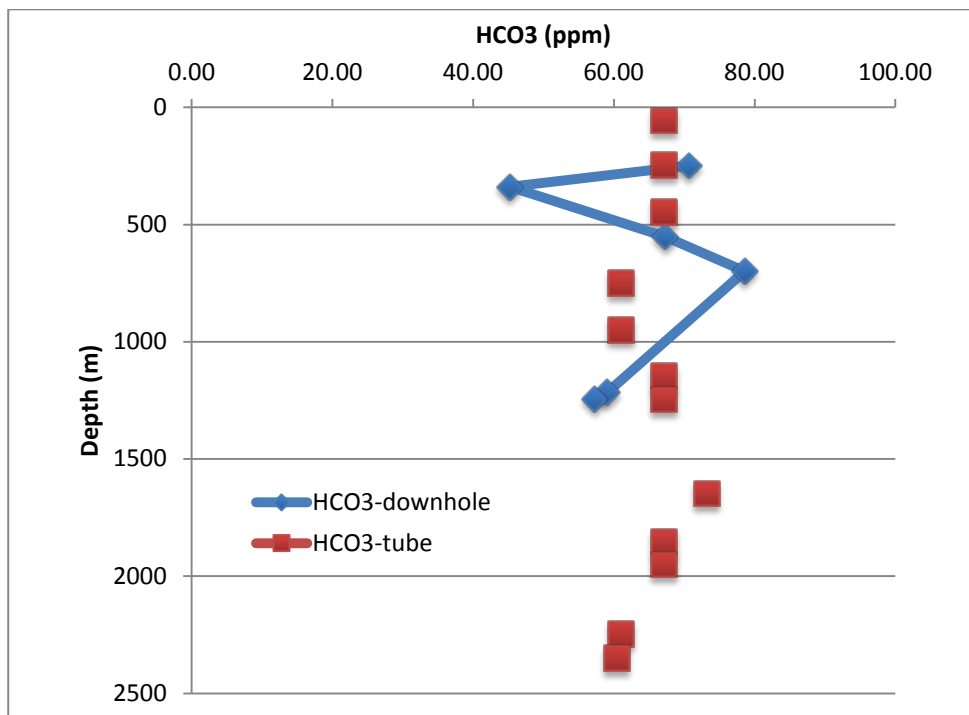
Figure 3.5.13. Comparison of COSC-1 HCO_3 concentrations in water obtained from downhole sampler analyzed by LBNL and tube sampler analyzed by GTK.

Good agreement is seen between the different sampling methods and analytical laboratories. There is a significant shift in water chemistry trends for most of the dissolved constituents at ~1200-1300 m depth, corresponding to two of the main conductive fracture zones (1210 & 1250 m) and the microkarst zone observed between 1200 − 1320 m. The waters are generally calcium-sulfate-bicarbonate in composition (Figure 3.5.14). The bottommost samples (2350, 2426 m) have higher TDS than all other samples – these were collected near the two deepest fracture flow zones and a change in lithology. There is a trend towards higher δD and δ^{18}O values for waters sampled from the deeper portion of the well. Interestingly, the intermediate depth compositions are similar to surface water isotope compositions that were used for drilling and flushing the well (Figures 3.5.15 to 3.5.16). These waters also have the lowest concentrations of most dissolved constituents, suggesting that most of the fluids in this portion of the wellbore contain a large component of dilute water from drilling and well flushing operations. This zone also has the lowest dissolved silica concentrations – given that the well has an conductive thermal gradient (20 °C/km – Lorenz et al. 2015b), equilibrated wellbore waters would be expected to progressively increase in silica concentrations with depth. However, the surface water composition also has low dissolved silica content, suggesting that the intermediate depth wellbore fluids that were sampled are dominated by surface water introduced by drilling and flushing operations. This is also consistent with the modeling results of the FFEC logs presented in Section 3.3, which reveal that the deeper fluid entries have a negative head, which would preclude significant inflow from these zones under static conditions.
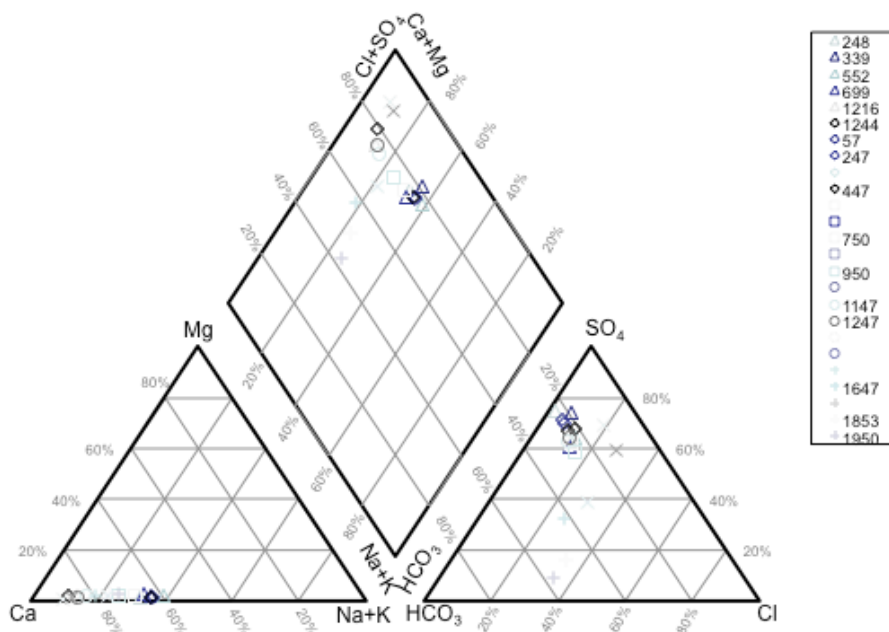
Figure 3.5.14. Piper diagram of borehole waters from COSC-1 well
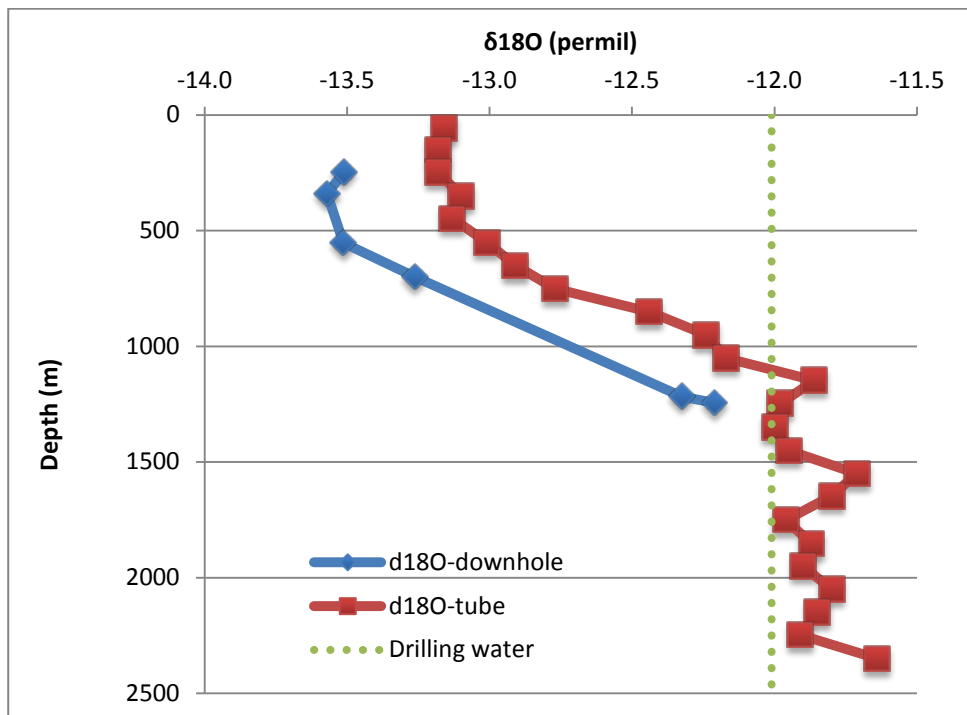
Figure 3.5.15. Comparison of COSC-1 $\delta^{18}O$ values obtained from downhole sampler waters analyzed by UC Berkeley and tube sampler waters analyzed by GTK. Drilling water shown for comparison.
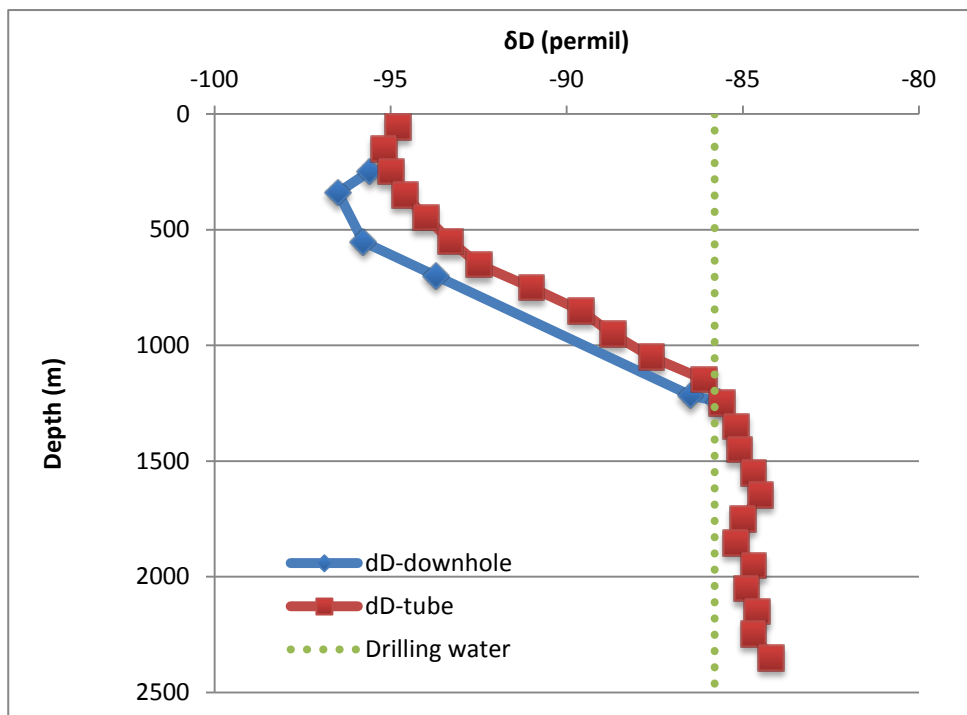
Figure 3.5.16. Comparison of COSC-1 δD values obtained from downhole sampler waters analyzed by UC Berkeley and tube sampler waters analyzed by GTK. Drilling water shown for comparison.

In order to obtain more representative compositions for future sampling efforts, two possible strategies could be followed. The first would be to pump the well to remove the current fluid composition from the wellbore, which still contains a significant fraction of dilute drilling/flushing water; this would also lower the hydraulic head, thus permitting the influx of fluids from the identified permeable fracture inflow zones. A more effective way of characterizing fluid compositions from these zones would be to isolate them using a packer assembly and pumping the isolated zones, thus allowing direct sampling of each of these intervals.

3.6   Microbial Characterization of Water Samples

Microbiological analysis was performed on downhole water samples taken from multiple sample depths of the COSC-1 borehole. The purpose of this microbiological analysis was to determine if assemblages of microbial communities varied by depth and if the fracture water microbial community composition could differentiate flow zones within the borehole. Since these were samples of opportunity, special effort to control microbiological variables, such as providing sterile conditions, was not possible. Within this context, our objective was to get preliminary information as to the feasibility of identifying microbial community differences at different depths within the borehole that would be reflective of the immediately adjacent fracture water and to determine if the extra effort required to obtain scientifically defensible samples using proper microbiological technique would be warranted for future studies.

Borehole water samples were collected on two separate dates, September 16-17, 2015 and October 2-3, 2015 and arrived at LBNL on September 23 and October 8, respectively (Figure 3.6.1). As described in other sections of the report, the first set of samples used a "tube" sampling method at 100 m depth intervals over the entire length of the borehole with a 10 mm ID tube for 8 depths ranging from 100 m to 2300 m. The samples arrived on September 23 and were filtered through a 0.2-micron pore size Nalgene filter to concentrate slightly under 500 ml of water volume for each sample depth. Genomic Deoxyribonucleic Acid (DNA) was extracted from the water filters for molecular analysis of the microbial composition. The DNA extraction was performed using the MoBio Power Soil DNA extraction kit (with garnet bead tubes). Each whole filter was cut in 1/2 and one half was put in each bead tube. DNA was isolated initially through a heat-lysis step (65 °C for 5 min.) before bead beating (5.5 m/s for 45 sec.). DNA from both halves of a filter was concentrated to a One-Spin filter and eluted in 60-uL elution buffer prior to analysis. Additional samples from 6 depths were received on October 8 using a conventional downhole sampling method. Approximately one liter from each polyethylene bottle, along with any associated sediment was filter and genomic DNA was extracted as previously described. The sample depths for the two sample types, along with the depths of the inflow zones identified by Tsang et al. (2016), are presented in Table 3.6.1. Note that in the case of the tube samples, the collection point is in many cases tens of meters away from the actual inflow zone. Some additional samples were intentionally collected away from known fracture sites to see if the inflow zones were distinct from regions in the borehole away from flowing fractures.

Figure 3.6.1. Tubing and bottle samples obtained for microbial characterization of COSC-1 borehole waters. Note that some of the bottle samples, which were collected using a downhole sampler, contain visible amounts of sediment.

Table 3.6.1. Correlation between identified inflow zones and microbiology sample depths

Inflow zone depth (m) Tsang et al. (2016)	Corresponding tube sample depth interval (m)	Corresponding bottle sample depth (m)
	94-100	248
339	294-300	339
507	494-500	
554		552
696		699
1214	1194-1200	1216
1245	1294-1300	1244
	1694-1700	
	1800-1806	
2300	2294-2300	
2380		

The exact microbial community composition for each sample was measured by molecular analysis of the extracted genomic DNA. This "culture-independent" technique does not require growth of the microbes in a laboratory media. It is estimated that over 99% of all microbes are resistant to being cultured in the laboratory, so DNA-based methods are proven to identify a much greater variety of microbial species. For this study we used two complementary DNA-based techniques to identify the individual bacterial and archaeal species in the sample. Both methods rely on DNA sequence variation of the 16S ribosomal RNA gene (rRNA) present in all genomic DNA as a type of "bar-code" to identify each different type of bacteria.

The first method uses the Berkeley Lab PhyloChip DNA microarray to identify the census of all the different species in a sample (DeAngelis et al. 2011). This method can accurately identify up to 60,000 different types of microbes in a sample using one million different tests, each probing for a different DNA

sequence variation found in a specific bacterium or archaea, in a single PhyloChip microarray. In addition to its accuracy, the advantage of this test is the ability to reproducibly identify very low abundance members of the microbial community. This method is very sensitive to small difference in the types and concentrations of the different microbial species in the community (Figure 3.6.2).
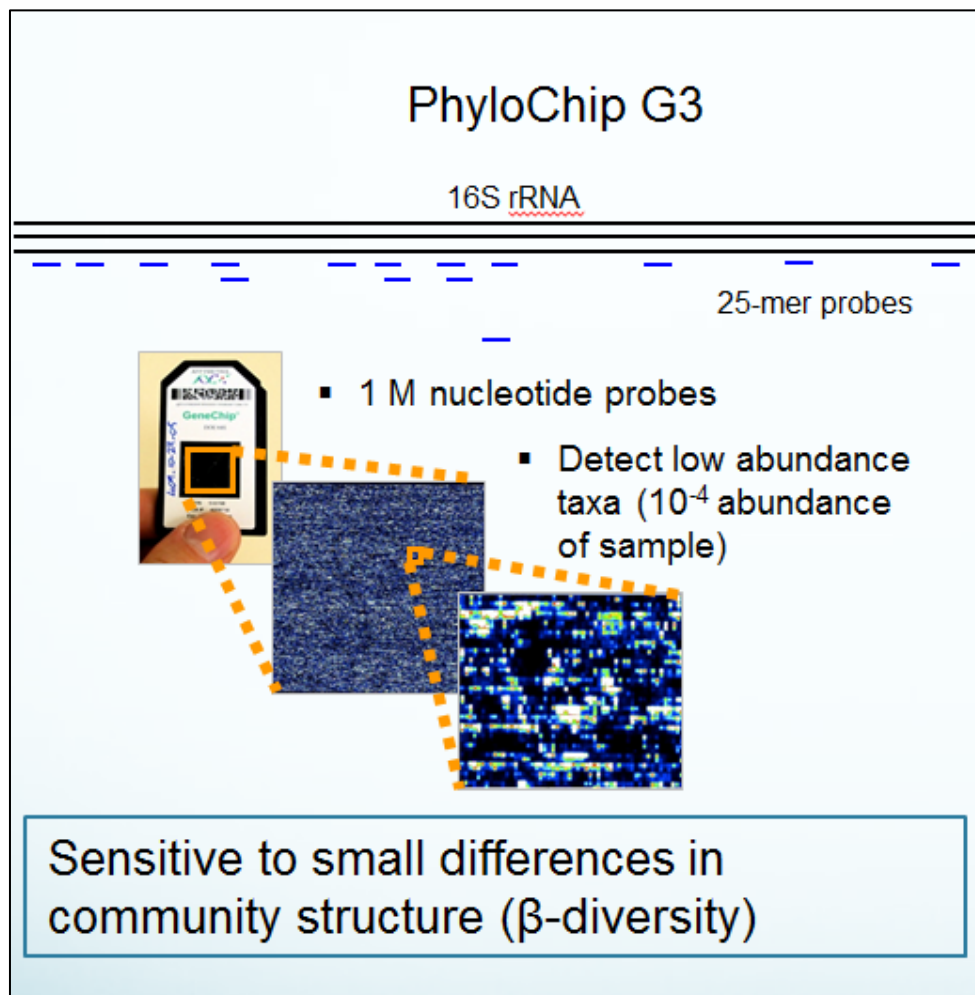
Figure 3.6.2. Key elements of PhyloChip G3 method. This technique is sensitive to small differences in community structure (β-diversity).

The second method is a next-generation DNA sequencing with the Illumina iTag machine (Figure 3.6.3). Instead of looking at variations in the entire 1,500 DNA sequence bases of the rRNA gene it focuses on a shorter 300 base region of the gene due to methodological constraints in sequencing longer regions of DNA. Although this method does not have the resolution of the PhyloChip it has the advantage of providing a more accurate estimation of the absolute concentration of the most abundant species in the sample. Taken together, the two methods provide the most reliable estimation of the types of microbes that are in an environmental sample and their abundance.

16S rRNA

V4 region (~300bp read length)

Figure 3.6.3. Key elements of iTag sequencing method. This technique can identify the most abundant organisms within a sample (α-diversity), as well as see large differences across samples (β-diversity).

Using these two independent methods for estimation of microbial community composition in each water sample and changes in both composition and abundance across samples we found remarkably similar results (Figures 3.6.4 and 3.6.5). The main conclusion from these data was that these microbial community analysis methods were able to differentiate flow zones within the borehole. Both analyses resulted in the delineation of upper and lower zones and additional structure within the lower zone was discernable in both data sets and statistically supported in the PhyloChip data. Both data sets also revealed trends in organism abundance consistent with geochemical parameters measured (e.g., sulfate-reducing bacteria) and indicated numerous bacteria likely responsive to the thermal gradient through the 2.5 km deep borehole.
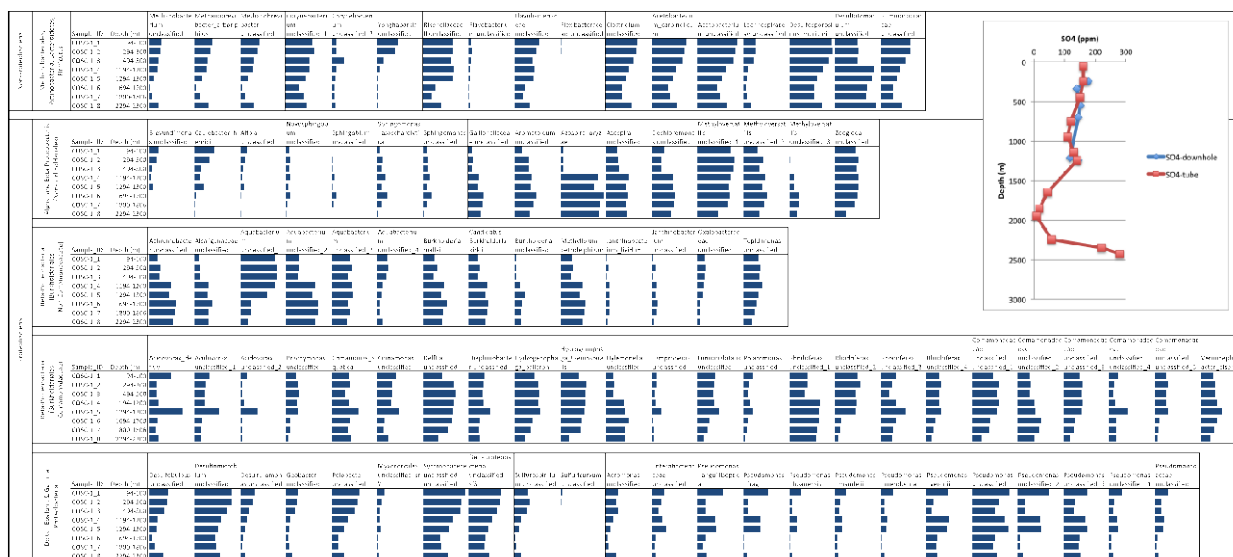
Figure 3.6.4. PhyloChip analysis of tubing samples. Many of these taxa appear to show changes consistent with the trends in sulfate compositions. Bars represent relative abundance.
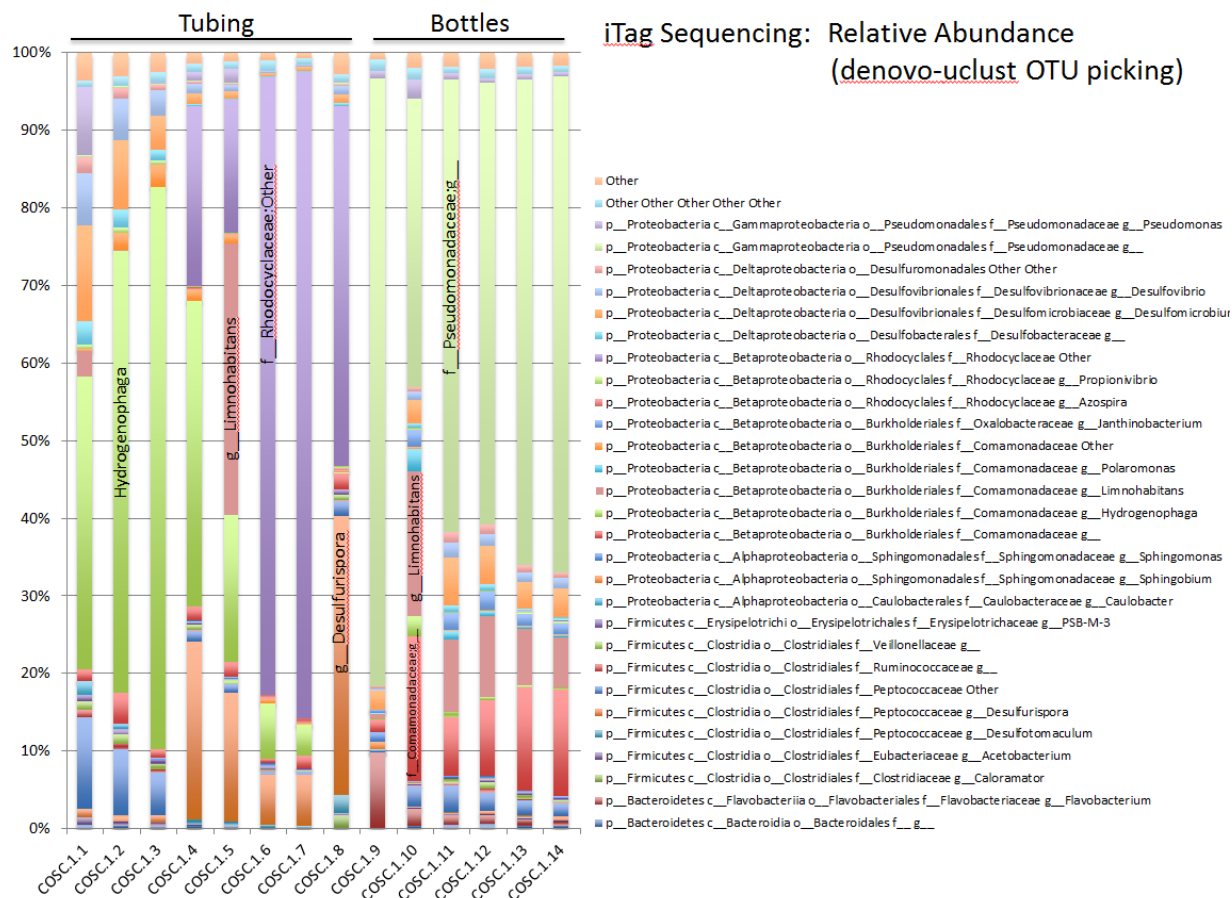
Figure 3.6.5. iTag sequencing of tubing and bottle samples, depicting the relative abundance of taxa that make up >0.5% of the population (denovo-uclust Operational Taxonomic Unit (OTU) picking).

The sampling methodology appeared to have a large influence on the vertical profiles, primarily due to sediment observed in the bottle-collected samples compared with the tubing-collected samples (see photos in Figure 3.6.1). PhyloChip and iTag sequencing results showed a clear separation of samples based on collection method (Figure 3.6.6), though there were other confounding factors that differed between the sample sets, so some differences could be related to borehole flushing rather than sediment load. The two suites of samples were not collected in identical locations in the borehole, as the tube samples were taken at the ends of the 100 m tube intervals; thus in many cases, they are tens of meters away from the actual inflow sites (Table 3.6.1). One suggestion for future microbiological study of deep boreholes would be to use inflatable packers to isolate specific targeted regions of the borehole for sample collection (e.g., Nyysonen et al. 2012). Anticipating that this will not always be feasible, especially at great depth, the tubing method yielded samples that appeared representative of the variable microbial communities throughout the borehole.

Sample_ID	Depth (mbs)	
COSC-1_1	94-100	
COSC-1_9	248	B
COSC-1_2	294-300	
COSC-1_10	339	B
COSC-1_3	494-500	
COSC-1_11	552	B
COSC-1_12	699	B
COSC-1_4	1194-1200	
COSC-1_13	1216	B
COSC-1_14	1244	B
COSC-1_5	1294-1300	
COSC-1_6	1694-1700	
COSC-1_7	1800-1806	
COSC-1_8	2294-2300	
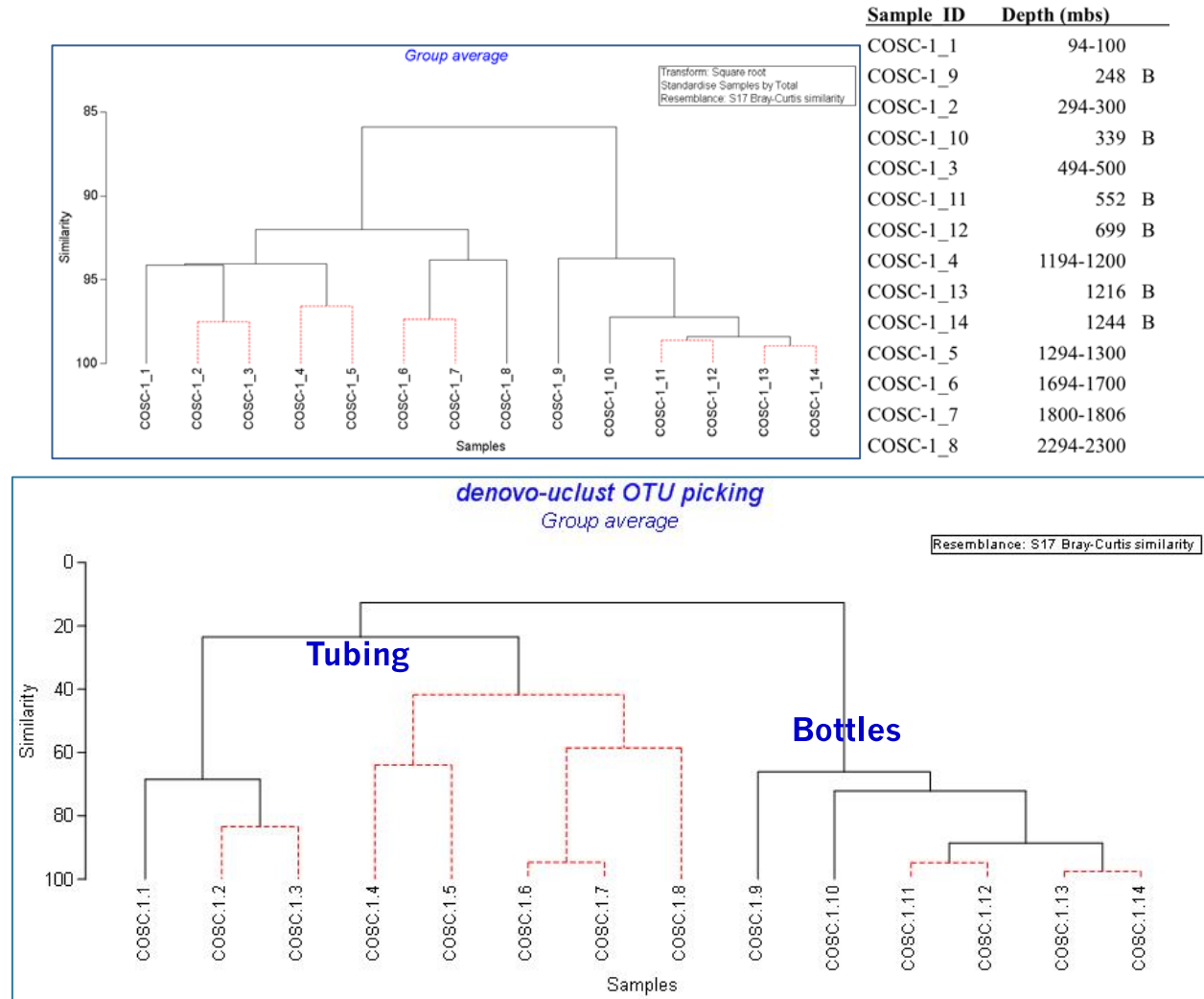
Figure 3.6.6. (upper) PhyloChip probe (OTU) intensity (relative abundance) data used for SIMPROFF analysis. All 1863 OTU data were used. Red dotted lines indicate no statistical difference [same SIMPROFF group]. (lower) - iTag Sequencing data OTU data. Similar distinctions between tubing and bottle samples were observed using this method.

The PhyloChip analysis provided strong support for identifying different functional classes of microorganisms that correlated with measured environmental parameters, including TDS, SO_4 and Na (Figure 3.6.4). The associated classes of bacteria and archaea that decreased with increasing wellbore depth but with a slight uptick in the deepest samples were, *Syntrophaceae, Pelobacter, Acetobacterium, Desulfosporosinus*, and *Desulfomicrobium*. The PhyloChip analysis also demonstrated how the microbial communities differed along the depth profile of the borehole. Three distinctive zones were observed, one that correlated to samples <1000 m, one that centered in the 1200-1300 m range, and one that was for samples > 1600 m. Within the > 1600 m samples the 2300 m sample was sometimes an outlier. Bacteria from the genera *Acidovorax, Pseudomonas, Comamonas*, and *Diaphrobacter* had a strong peak at 1300 m.

The iTag analysis of the 16S rRNA gene sequencing data revealed a very similar overall microbial community structure with greatest differences between the initial tube-collected samples from September 16-17, 2015 and the bottle collected samples collected on October 2-3, 2015 (Figure 3.6.5). Bacterial taxa

from the genus *Hydrogenophaga* dominated the shallower, tube-collected samples, peaking in dominance at 500 m depth and were also observed in shallow bottle samples. These bacteria are known for their ability to oxidize hydrogen as an energy source and often couple with methane generating microorganisms. Bacteria from the *Limnohabitans* were one of the dominant organisms in deeper samples, especially at 1300 m. This group of organisms is commonly identified in European freshwater habitats and is known for their fast rate of growth. Among the common organisms identified from the deeper samples were members of the Family *Rhodocyclaceae* with peak dominance at around 1800 m. This aquatic group of organisms contains a number of members that are able to perform an oxygenic photosynthesis, which is consistent with this anoxic environment. An unidentified species from the genus *Desulfurispora* dominated the samples at 1200 m (23% of the microbes) and 2300 m (36%) with much lower numbers in the other deep samples. This sulfate-reducing bacterium is typically thermophilic and able to grow between 40-67 °C. Similar to the PhyloChip analysis, many organisms, especially sulfur-cycling bacteria, were found to decrease in relative abundance with depth of sample with an uptick in abundance in the deepest sample.

With identification of the entire microbial community using the two DNA-based methods we were able to determine that microorganisms varied by depth and the type of microbes found at the different depths corresponded well with our previous knowledge of their habitat preference. From this, we can conclude that samples collected from the different depths had a high likelihood of containing fracture water originating from the nearby flow zone. This work also demonstrates the utility of using microbial analysis as a biomarker to indicate the integrity of the sampling procedure. Future work with added emphasis on using best practices for microbiological collection techniques will help to understand flow and fracture water transport through the subsurface from this region.

3.7   Conclusions

The COSC project provides an excellent opportunity for the DOE Deep Borehole Field Test project to glean key insights regarding the characterization of basement rocks intersected by a deep borehole through geophysical surveys and downhole logging, lithologic descriptions of core, and structural studies (deformation, stress measurements, fracture orientations). The COSC-1 well also allows testing of hydrologic characterization methods in a deep borehole environment through flowing fracture identification and modeling, fluid chemistry variations with depth, and microbial community characterization. Through the FFEC logging, a total of eight hydraulically conductive zones were identified, each localized over a small depth zone, suggesting that they are individual fractures; this has been confirmed by evaluation of the corresponding core). All the inferred fracture properties determined from modeling – flow rate, salinity, transmissivity, and hydraulic head – varied greatly among the fractures, as is typical of a poorly connected fracture network in low-permeability rock. Salinity values are relatively low and hydraulic head variability suggests downward groundwater flow. Collected core samples obtained from hydraulically conductive zones in the COSC-1 well provided a means to directly compare core scale vs. formation scale permeability measurements obtained in the laboratory and field, respectively. Geochemical and microbiological studies conducted at the COSC-1 site reveal the challenges in obtaining representative samples of the deep borehole environment – contamination with drilling fluids was observed particularly in the deeper sections of the borehole, where little fracture permeability was present.

There are additional research opportunities with the COSC-1 well that could be pursued in FY17. These include examining borehole breakout data, downhole seismic logs and core lithology and XRF chemistry data (all of which have been collected by the COSC science team), and see how these correlate with the observed permeable fracture zones and variations in fluid chemistry. It would also be useful to attempt downhole fluid sampling of the COSC-1 well at the hydraulically conductive zones using a straddle

packer assembly to obtain less contaminated samples of the inflow zone waters. The techniques that were demonstrated to be most successful in characterizing the lithologic and hydrologic properties of the COSC-1 well should be considered for use in the DOE deep characterization borehole once it has been drilled.

3.8   References

DeAngelis, K.M., Wu, C.H., Beller, H.R., Brodie, E.L., Chakraborty, R., DeSantis, T.Z., Fortney, J.L., Hazen, T.C., Osman, S.R., Singer, M.E., Tom, L.M., and Andersen, G.L. 2011 PCR amplification-independent methods for detection of microbial communities by the high-density microarray PhyloChip. *Applied Environmental Microbiology* 77:6313-6322.

Doughty, C. and C.F. Tsang, 2000. BORE II – A code to compute dynamic wellbore electrical conductivity logs with multiple inflow/outflow points including the effects of horizontal flow across the well, Rep. LBL-46833, Lawrence Berkeley National Laboratory, Berkeley, CA, 2000. Available from: www.ipo.lbl.gov/lbnl12561673/

Doughty, C. and C.F. Tsang, 2005. Signatures in flowing fluid electric conductivity logs, *J. Hydrol*. 310, 157–180.

Doughty, C., S. Takeuchi, K. Amano, M. Shimo, C.-F. Tsang, 2005. Application of Multi-rate Flowing Fluid Electric Conductivity Logging Method to Well DH-2, Tono Site, Japan, *Water Resour. Res.* 41, W10401, doi:10.1029/2004WR003708.

Doughty, C., C.F. Tsang, K. Hatanaka, S. Yabuuchi. and H. Kurikami, 2008. Application of direct-fitting, mass integral, and multirate methods to analysis of flowing fluid electric conductivity logs from Horonobe, Japan, *Water Resour. Res.* 44, W08403, doi:10.1029/2007WR006441.

Doughty, C., C.F. Tsang, S. Yabuuchi, T. Kunimaru, 2013. Flowing fluid electric conductivity logging for a deep artesian well in fractured rock with regional flow, *J. Hydrol.* 482, 1–13.

Follin S., 2008. Bedrock hydrogeology Forsmark, Site descriptive modeling, SDM-Site Forsmark, SKB report R-08-95, available at www.skb.se

Follin, S., L. Hartley, I. Rhén, P. Jackson, S. Joyce, D. Roberts, B. Swift, 2014. A methodology to constrain the parameters of a hydrogeological discrete fracture network model for sparsely fractured crystalline rock, exemplified by data from the proposed high-level nuclear waste repository site at Forsmark, Sweden. *Hydrogeol. J.* 22, 313–331.

Gee, D.G., Janák, M., Majka, J., Robinson, P., and van Roermund, H. 2013 Subduction along and within the Baltoscandian margin during closing of the Iapetus Ocean and Baltica-Laurentia collision, *Lithosphere* 5:169-178, doi:10.1130/L220.1

Gee, D.G., C. Juhlin, C. Pascal, and P. Robinson, 2010. Collisional orogeny in the Scandinavian Caledonides (COSC) 2010, GFF, 132(1), 29 – 44, doi:10.1080/11035891003759188.

Gentier, S., Lamontagne, E., Archambault, G., and Riss, J., (1997). "Anisotropy of flow in a fracture undergoing shear and its relationship to the direction of shearing and injection pressure." International Journal of Rock Mechanics and Mining Sciences 34(3): 94.e91-94.e12.

Lorenz, H., Rosberg, J.E., Juhlin, C., Bjelm, L., Almqvist, B.S.G., Berthet, T., Conze, R., Gee, D.G., Klonowska, I., Pascal, C., Pedersen, K., Roberts, N.M.W., and Tsang, C.F. (2015a) COSC-1 – drilling of a subduction-related allochthon in the Palaeozoic Caledonide orogen of Scandinavia, *Scientific Drilling* 19:1-11, doi:10.5194/sd-19-1-2015

Lorenz, H., Rosberg, J.E., Juhlin, C., Bjelm, L., Almqvist, B.S.G., Berthet, T., Conze, R., Gee, D.G., Klonowska, I., Pascal, C., Pedersen, K., Roberts, N.M.W., and Tsang, C.F. (2015b) Operational report about Phase 1 of the Collisional Orogeny in the Scandinavian Caledonides scientific drilling project (COSC-1), *GFZ German Research Center for Geosciences*, doi:10.2312/ICDP.2015.002

McDonald, K.T. 2000. "Resistance of a Disk", www.physics.princeton.edu/~mcdonald/examples/resistivedisk.pdf, accessed June 30, 2016.)

Moir, R.S., Parker, A.H., and Bown, R.T. 2014 A simple inverse method for the interpretation of pumped flowing fluid electrical conductivity logs, Water Resour Res 50, 6466–6478, doi:10.1002/2013WR013871.

Nyyssönenn, M., Bomberg, M., Kapanen, A., Nousiainen, A., Pitkänen, P., and Itävaara, M. (2012) Methanogenic and Sulphate-Reducing Microbial Communities in Deep Groundwater of Crystalline Rock Fractures in Olkiluoto, Finland, *Geomicrobiology Journal*, 29:10, 863-878.

Rhén, I., Forsmark, T., Hartley, L., Jackson, P., Roberts, D., Swan, D., and Gylling, B., 2008. Hydrogeological conceptualization and parameterization, Site descriptive modeling SDM-Site, Laxemar, SKB report R-08-78, available at www.skb.se.

Thiem, G., 1906. Hydrologische methoden (in German). Leipzig: J. M. Gebhardt: 56.

Tsang, C.F. and Doughty, C. 2003 Multirate flowing fluid electric conductivity logging method, *Water Resources Research* 39(12):1354-1362, doi:10.1029/2003WR002308

Tsang, C.-F., P. Hufschmied, and F. V. Hale, 1990. Determination of fracture inflow parameters with a borehole fluid conductivity logging method, *Water Resour. Res. 26, 561–578.*

Tsang, C.F., Rosberg, J.E., Sharma, P., Berthet, T., Juhlin, C., and Niemi, A. (2016) Hydrologic testing during drilling: application of the flowing fluid electrical conductivity (FFEC) logging method to drilling of a deep borehole, Hydrogeology Journal 24: 1333-1341.

West L and Odling N (2007) Characterization of a multilayer aquifer using open well dilution tests, Ground Water 45,74–84, doi:10.1111/j.1745-6584.2006.00262.x

THIS PAGE INTENTIONALLY LEFT BLANK

4. SEAL MODELING

In this section, we present LBNL's activities related to seal modeling. To set the stage, we first review some of analogous key observations that are important for developing the seal modeling strategy. This includes a review of field observations on stress and permeability at depth and observations of damage, borehole break-out and disturbed zone around tunnels and boreholes. We then present our initial thermal-hydrological (TH) modeling of deep borehole disposal focusing on thermally driven fluid pressurization and potential upflow along an assumed disturbed zone. Finally we present plans for the next step, which will be to add mechanical processes, in a coupled thermal-hydrological-mechanical (THM) analysis of the deep borehole system, as well as modeling of the evolution of the disturbed zone around the deep well, and impacted by seals and plugs within the borehole, eventually including effects of long-term chemical processes on the seals in a THMC analysis.

4.1 Stress and Permeability at Depth

Deep boreholes extending several km down into the crystalline basement will be exposed to high tectonic stress. Figure 4.1.1 shows vertical profiles of vertical stress (S_v) and lateral stress coefficient $k = S_h/S_v$ where S_h is horizontal stress. Figure 4.1.1 (a) shows that stress would be around 80 MPa at 3 km depth, and if extrapolating to 5 km, it would be around 100 MPa. It is also shown that at 3 km the horizontal stress might be as high as the vertical or as low as 1/3 of the vertical, creating a differential stress that could have consequences on borehole stability. Figure 4.1.2 shows estimates of stresses down to about 5 km at two deep boreholes in Sweden and Germany indicating high differential horizontal stress with maximum as horizontal stress as high as 200 MPa at 5 km depth (Lund and Zoback, 1999; Brudy et al. 1997). Considering stress concentration around a well, maximum compressive stresses could then easily exceed the compressive strength of rock and borehole break-out may occur. In fact, the stress estimates made at depth in these deep boreholes are based on observed borehole break out and drilling-induced tensile fractures. Figure 4.1.1 and 4.1.2 gives as estimates as to what range of boundary stresses we could apply to the coupled THM models.

At depths of 3 to 5 km, the stresses are high and therefore fractures might be expected to be closed for fluid flow and permeability limited to low permeability matrix flow. However, a compilation of permeability in bedrock shown in Figure 4.1.3 shows that at 3 to 5 km depth, permeability can be substantially higher than that of intact crystalline rocks, indicating that fractures can stay open at depth. Figure 4.1.3 gives an estimate of what ranges of permeability could be applied to the THM models.

The field data shown in Figure 4.1.1 to 4.1.3 gives a range, but the goal of the site investigations for deep borehole disposal would probably be to find an area of intact low permeability rocks with low and isotropic stress.
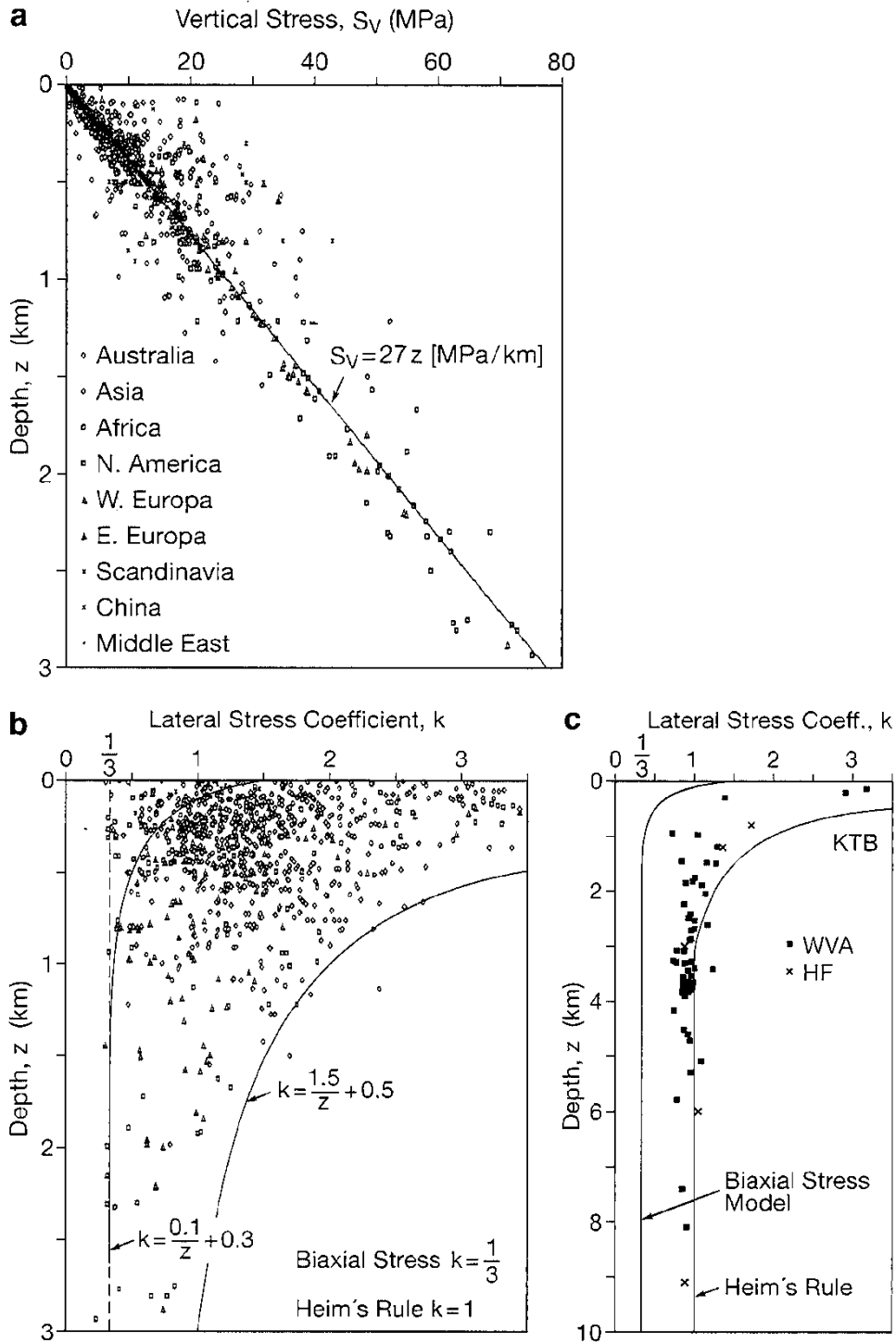
Figure 4.1.1. Global compilation of (a) vertical stress and (b, c) lateral stress coefficients, k, down to a depth of 3 km in the Earth's crust according to Brown and Hoek (1978) (Zhang and Stephansson, 2010).
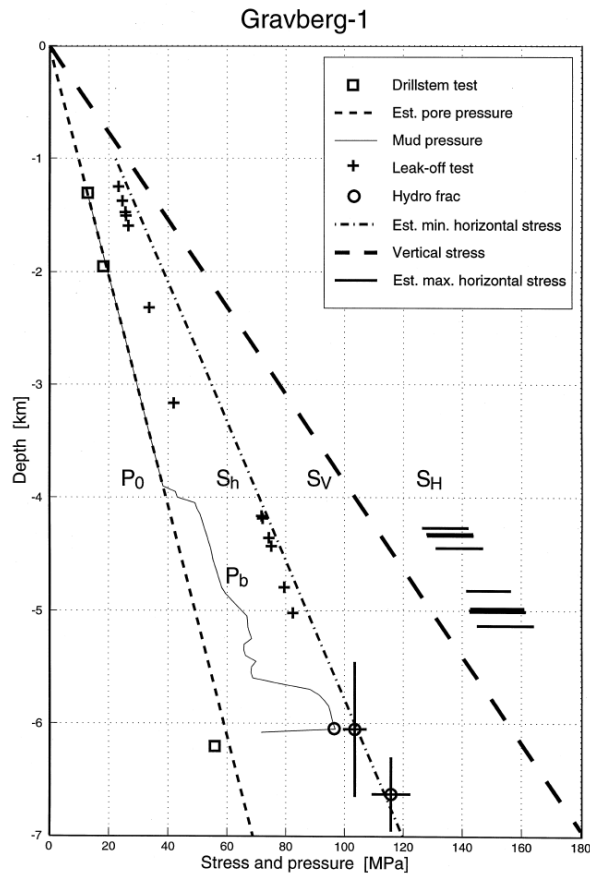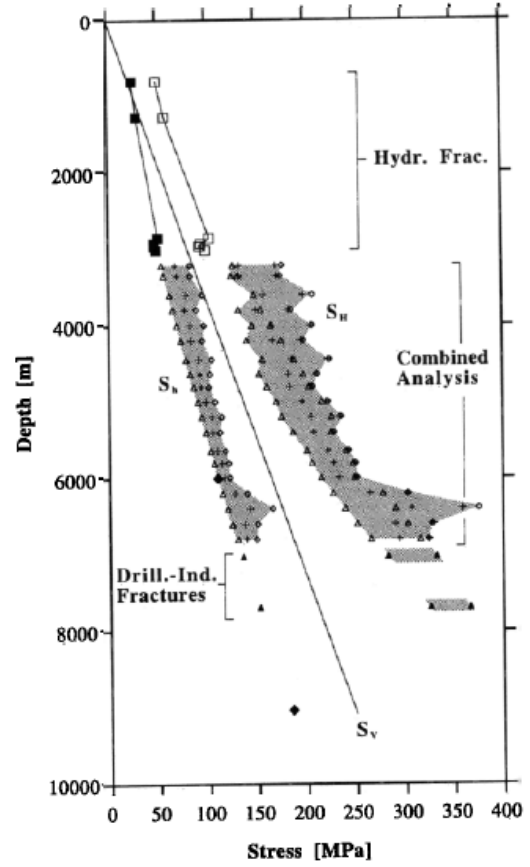
Figure 4.1.2. Published stress estimates at (a) Gravberg-1 deep borehole in Sweden (Lund and Zoback, 1999), and at (b) KTB borehole Germany (Brudy et al. 1997).
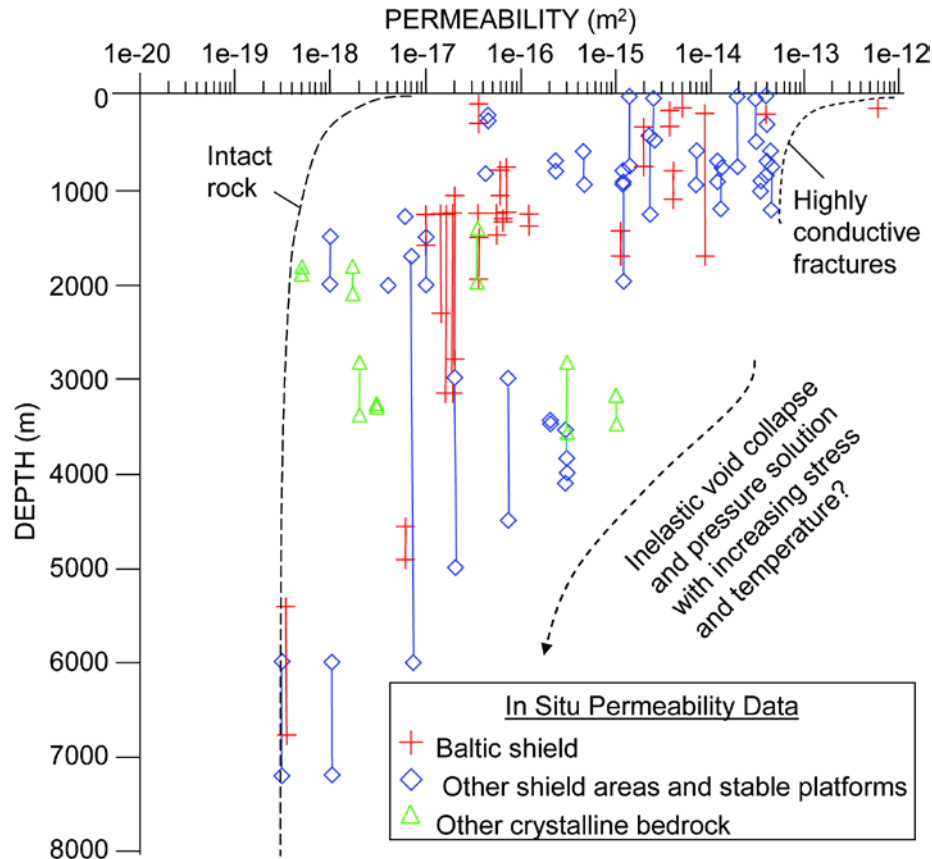
Figure 4.1.3. Compilation of permeability measurements in boreholes in crystalline bedrock (from Juhlin et al. 1998) with added schematic of upper and lower limits of permeability related to mechanical and chemo-mechanical behavior (Rutqvist 2015).

4.2 Spalling, Borehole Break-out and Disturbed Zone

Figure 4.2.1 shows example of borehole break-out in deep boreholes associated with deep borehole drilling projects in Europe (Lund and Zoback 1999; Brudy et al.1997). The figures show various degrees of borehole break-out including depths around 3 to 6 km. Another analogue for disturbed zone changes are the very extensive studies of excavation damage and disturbed zones around tunnels at the Manitoba underground research laboratory (URL) in Canada and at the Äspö Hard Rock Laboratory in Sweden (Bäckblom and Martin 1999). At the Manitoba URL, some parts consist of massive granite without any natural macroscopic fractures. The stress is relatively high for the depth with a high maximum horizontal stress. Figure 4.2.2 shows one well known example from these studies associated with a mine-by experiment (Read 2004). So-called spalling failure has occurred at the top and bottom and permeability changes of up to six orders of magnitude have been measured in this excavation damaged zone (Rutqvist and Stephansson 2003; Bäckblom and Martin 1999). However, from studies at both the Manitoba URL and the Äspö Hard Rock Laboratory in Sweden, it has been observed that a small confining pressure can effectively inhibit stress induced fracturing or spalling failure (Andersson and Martin, 2009). Moreover, at both the Manitoba URL and the Äspö Hard Rock Laboratory it has been observed that the *in situ* compressive strength (spalling around tunnels) is about 50% of laboratory compressive strength. A question is how this translates into large diameter boreholes (e.g., 41 inches) that could be used in a deep borehole concept. Nevertheless, based on the observations reviewed in this section we conclude that the

evolution of the disturbed zone through different stages of disposal development (borehole break-out) is likely to be a key issue for deep borehole nuclear waste disposal.
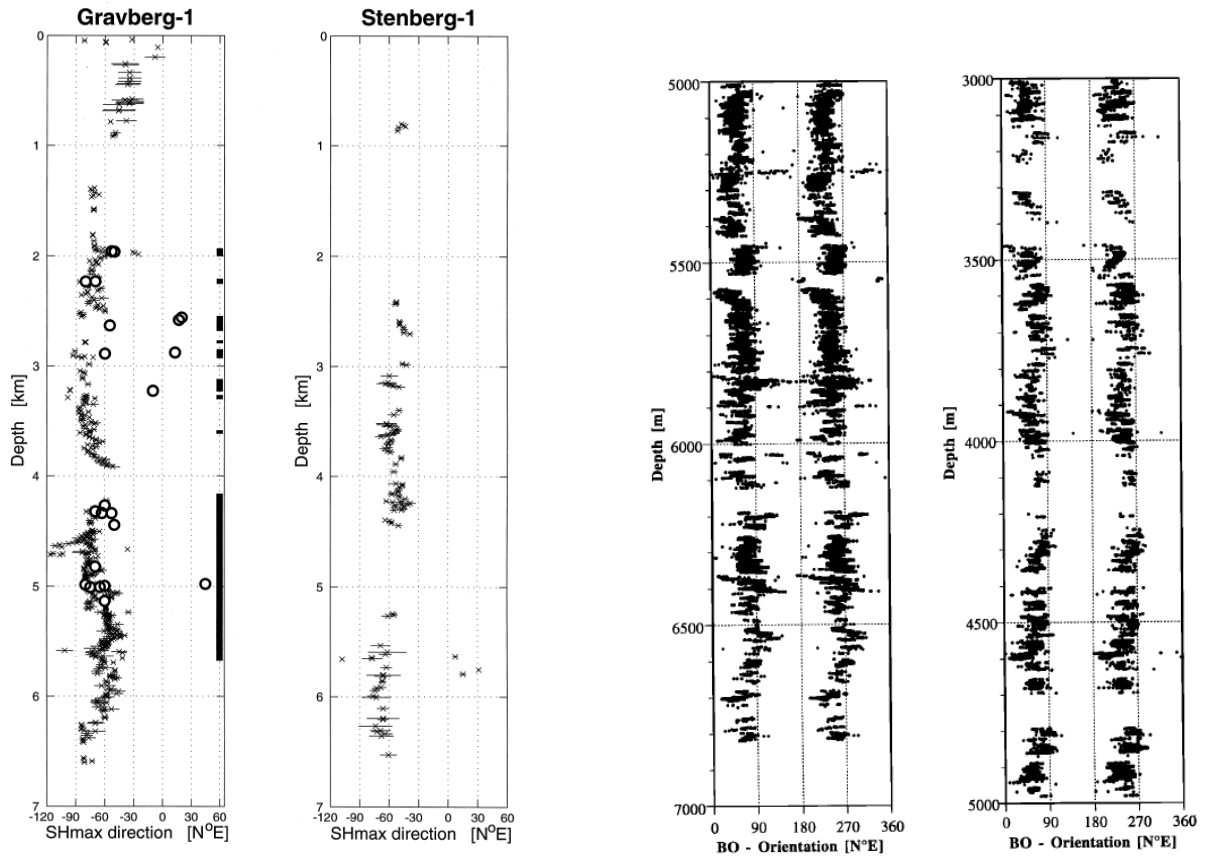
Figure 4.2.1. Published borehole break-out data at (a) Gravberg-1 and Stenberg -1 deep boreholes in Sweden (Lund and Zoback, 1999), and at (b) KTB borehole Germany (Brudy et al. 1997).
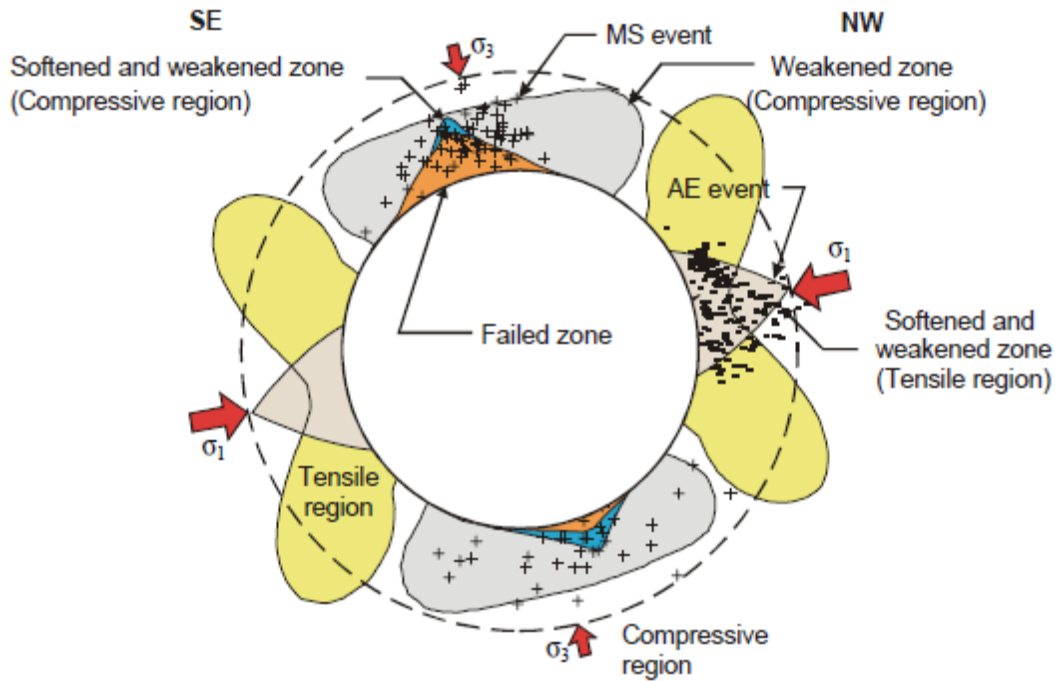
Figure 4.2.2. EDZ characteristics around the mine-by test tunnel at the Manitoba URL, Canada (Read 2004).

4.3   TH Modeling of Thermal Pressurization and Upflow through Disturbed Zone

Previous simulation studies have performed thermal-hydrological calculations (Brady et al. 2009) and coupled flow-thermal-mechanical calculations (Rutqvist et al. 2014) for single boreholes (isolated, or spaced far apart relative to the timescales of heat transfer and decay of the heat source), while another (Arnold and Hagdu 2013) has examined fields with groups of equally spaced boreholes to examine multi-well interactions, although using a lower-resolution 3D grid. In this section we discuss efforts to develop and run a cylindrical system within the framework of the TOUGH2 family of codes. This model will not only assess thermal pressurization and flow, but will also be compatible with TOUGHREACT (for coupling geochemistry) and TOUGH-FLAC (for coupling geomechanics) for use in future THMC modeling studies.

4.3.1   Simulation setup

To assess the effect of multiple interacting wellbores on the thermal states and potential upflow within the wellbore or surrounding rock, we performed TOUGH2/TOUGHREACT (Pruess et al. 1999; Xu et al. 2006) simulations using a radially symmetric 2D/3D r-z mesh (Pruess et al. 1999). The simulated zone corresponds to a single wellbore that is part of a larger field, arranged in a rectangular pattern with 200 m spacing between wellbores (Figure 4.3.1). The cylindrical simulated zone extends from the surface to -7,000 m, has a radius of 100 m, with no-flow boundaries at r = 100 m consistent with uniform 200 m wellbore spacing (Figure 4.3.2). The mesh contains 20,505 elements with variable refinement, including high resolution in r and z near the wellbore and near boundaries between zones of differing permeability and thermal conductivity. The wellbore, waste disposal zone, a distinct disturbed-rock zone next to the wellbore (Brady et al. 2009), and sedimentary and crystalline rock zones are all explicitly defined within

the mesh to allow localized parametric variations. Rock properties for the simulated system are listed in Table 4.3.1.
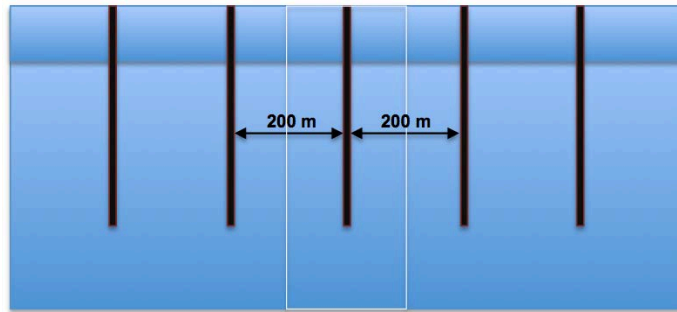
Figure 4.3.1. Spacing of multiple wellbores, showing 100 m simulated zone (wellbore to midpoint) and no-flow boundaries.
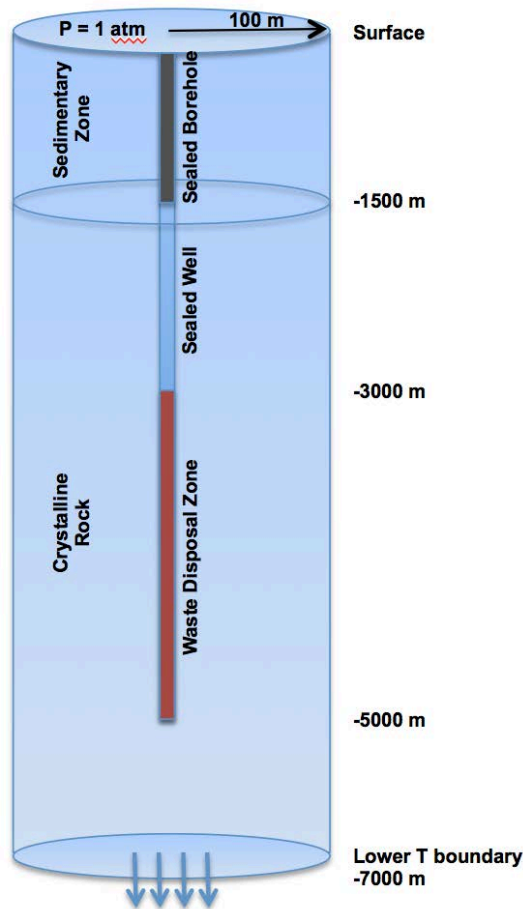
Figure 4.3.2. Configuration of the cylindrical simulated region, including wellbore, sealed well, waste disposal zone, and boundaries.

Table 4.3.1. Simulated rock properties (from Brady et al. 2009).

From: Brady et al. (SAND2009-4401)	k (mD)	φ	ρ (kg/m³)	Spec. Heat (J/kg/K)	Thermal Cond. (W/mK)
Sedimentary Rock	10/1.0	0.30	2750.0	1000.0	3.3
Crystalline Bedrock	0.0001	0.01	2750.0	790.0	3.0
Damaged Bedrock	0.2 (2.0,20.0)	0.01	2750.0	790.0	3.0
Sealed Borehole	0.1 (1.0)	0.35	2750.0	760.0	0.8
Waste/Sealed Well Casing	0.00001	0.0001	2750.0	760.0	46.0

The simulations were performed using EOS4 (Pruess et al. 1999) under fully saturated, non-isothermal conditions. The system was first equilibrated to hydrostatic conditions and a linear temperature profile of 25 °C/km (Brady et al. 2009) with constant pressure at the surface (1 atm). The waste packages were represented by a series of time-variable heat sources implemented within the TOUGH2/TOUGHREACT source/sink framework (Pruess et al. 1999). The base heat curve assumes a single average pressurized-water reactor (PWR) fuel assembly aged for 25 years before emplacement (Brady et al. 2009) with an initial output of 580W/canister. Heat output vs. time is represented by the curves designed by Greenberg et al. (2013). A second heat source is considered, with a higher initial heat output of 2,600W/canister, representative of reprocessed high-level waste aged 10 years before emplacement. The heat sources are arranged uniformly within the wellbore at depths from z = - 5,000m to z = -3,000 m (the waste disposal zone). Fully coupled, non-isothermal simulation of flow and heat transport was performed for up to 100,000 years of simulation time to assess temperature, pressure, and flow-field changes in the system.

Within the TOUGH2/TOUGHREACT simulation, temperatures and pressures were monitored at various radii from the midpoint of the waste disposal zone (from the package wall to the far boundary) as well as at the top of the crystalline rock zone and near the surface. Water flow was monitored in the disturbed-rock zone at multiple locations from the waste disposal zone to the surface. In addition to the base parametric cases (Table 4.3.1), the simulations were also run using the same initial conditions but with increased permeability of the damaged-rock zone and sealed borehole.

4.3.2 Simulation results: Thermal response

The thermal response of the system for the 580W canister configuration resembles the behavior seen in earlier thermo-hydrological modeling (Brady et al. 2009; Arnold and Hegdu 2013) at early times. Figure 4.3.3 presents temperature vs. time for monitoring points at 0 m, 1 m, 10 m, 50 m, and 100 m from the waste packages at the midpoint of the waste disposal zone (z = -4,000 m) for both 580W (left) and 2,600W (right) waste canisters. For the first hundred years, we see temperatures rise steadily, reach an initial maximum and begin to decrease. The temperature increases near the borehole 580W packages are not large and initially drop off with increasing distance from the borehole. For 2,600W waste canisters the temperature change is much greater, with initial temperature increases exceeding 80 °C near the wellbore.

The effect of interacting adjacent wellbores becomes apparent after 100 years of simulation. In the single-wellbore T-H study of Brady et al. (2009), temperatures drop quickly and return to near-ambient levels by t = 10,000 yr. With multiple wellbores, temperatures begin increasing again at t = 200 yr and climb steadily until t = 20,000 yr as thermal disturbances from the adjacent emplacements reach the monitored elements. The second temperature peak at t = 20,000 yr is of similar magnitude to the first peak at t = 100 yr, but the increased temperatures persist for tens of thousands of years. Temperatures drop slowly and do not approach ambient/initial conditions until after 100,000 yr.
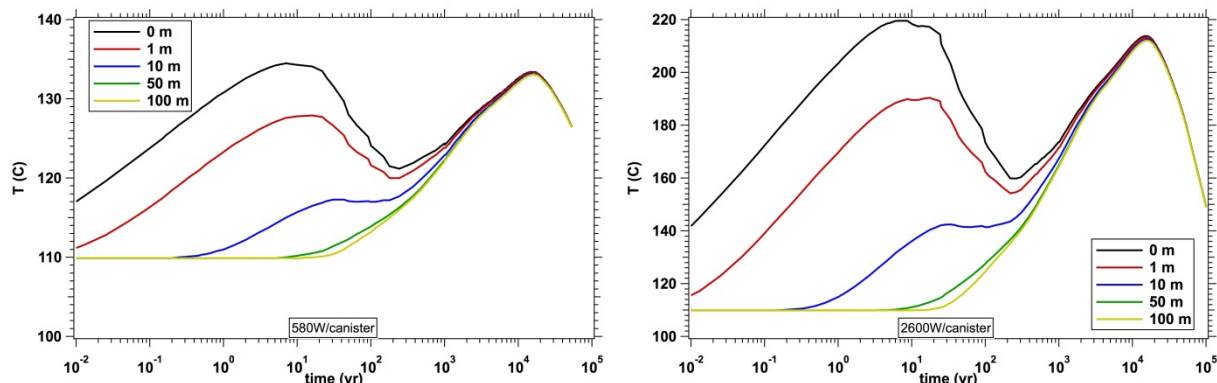
Figure 4.3.3. Temperature evolution at several distances from the waste packages at the midpoint of the waste disposal zone (z = -4,000 m) for 580W (left) and 2,600W (right) canisters.

Figure 4.3.4 presents the temperature evolution adjacent to the wellbore at varying depths: -3,000 m (top of waste disposal zone), -1,500 m (top of crystalline rock), and -500 m. We see significant temperature increases only near the top of the waste canister, with only minimal temperature effects higher in the sediment column away from the emplacement zone for the case of 580W canisters. However, some warming is apparent within the sedimentary zone for the case of 2,600W canisters after t =10,000 yr.
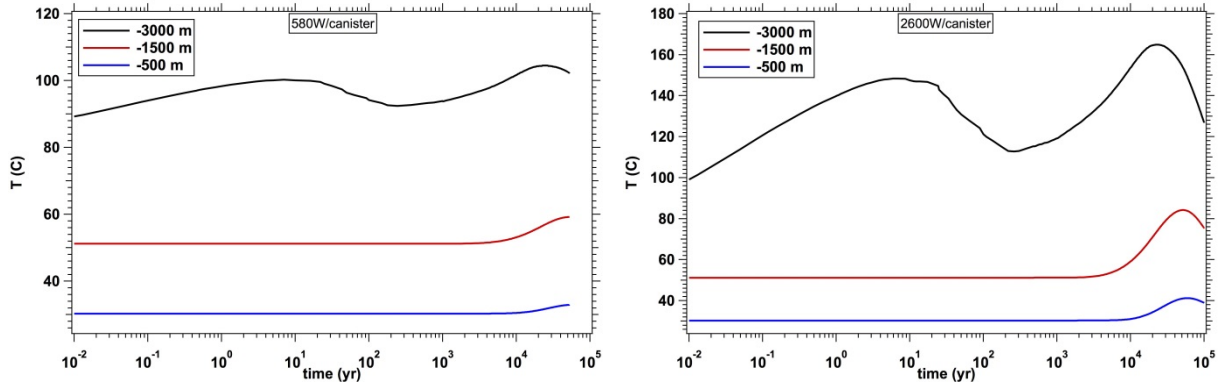
Figure 4.3.4. Temperature evolution adjacent to the wellbore at z = -3,000 m, -1,500 m, and -500 m (r = 0 m) for 580W (left) and 2,600W (right) canisters.

4.3.3 Simulation results: Pressure Response and Fluid Flow

The pressure response of the system to thermal changes, and the resulting fluid flow, are expected to deviate from previous single-well studies due to the lack of open/distant boundaries, the secondary thermal peak from multiple interacting wellbores, and well as differences in the assumed permeability and porosity of the near-wellbore region (including mesh geometry). Figure 4.3.5 presents the evolution of pressures at various distances from the waste canisters at the midpoint of the waste disposal zone (z = -4,000 m). For the 580W waste canisters, pressure changes peak at +10 MPa at t = 2,000 yr, at all monitored radii as the thermally driven pressure changes propagate rapidly (compared to simulation time) through the low-permeability but still permeable crystalline rock. Emplacement of 2,600W canisters results in a much larger surge in pressure, reaching +42 MPa by t = 1,500 yr. Note that the peak in pressures corresponds to the period where temperatures at all radii begin to rise again due to thermal interaction between wellbores.
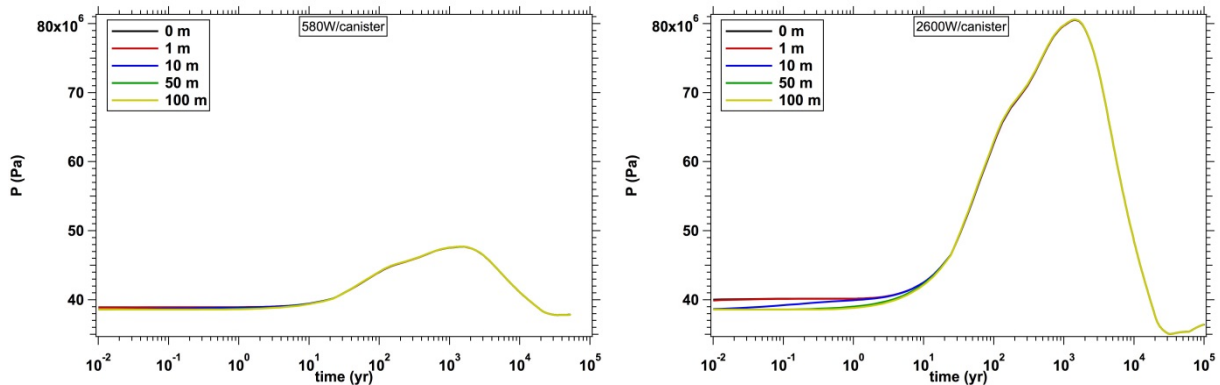
Figure 4.3.5. Pressure evolution at several distances from the waste packages at the midpoint of the waste disposal zone (z = -4,000 m) for 580W (left) and 2,600W (right) canisters.

Pressure changes do not propagate higher into the region around the sealed wellbore, however. Figure 4.3.6 presents pressure evolution in the disturbed-rock zone adjacent to the wellbore at z = -3,000 m (top of waste disposal zone), -1,500 m (top of crystalline rock zone), and -500 m. Only within the crystalline rock immediately above the heated waste disposal zone do we see large pressure increases.
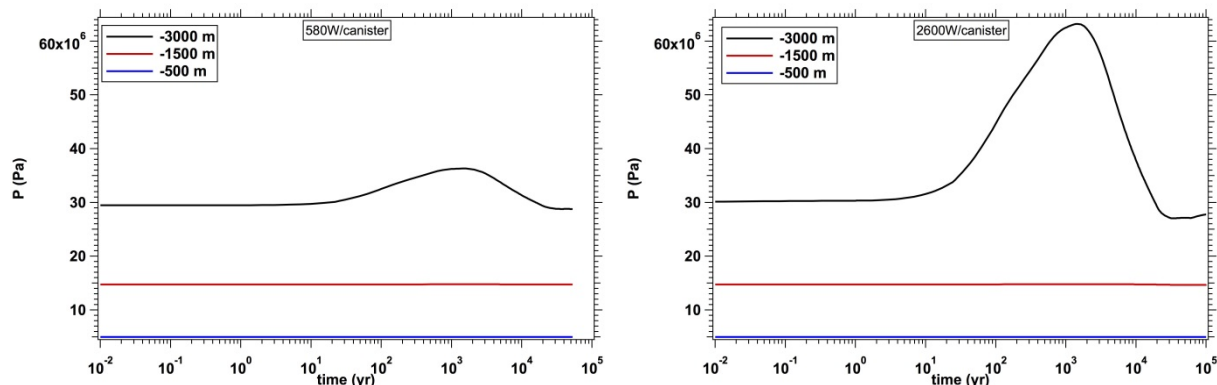
Figure 4.3.6. Pressure evolution adjacent to the wellbore at z = -3,000 m, -1,500 m, and -500 m (r = 0 m) for 580W (left) and 2,600W (right) canisters.

The water flows resulting from these induced pressure gradients are shown in Figure 4.3.7, as recorded in the disturbed-rock zone at varying depths. At the top of the waste disposal zone (z = -3,000 m) and at the top of the low-permeability crystalline rock (z = -1,500 m), we see significant upward flows of water on the order of 100s (580W canisters) to 1,000s (2600W canisters) of kg per year. However, once into the higher-permeability sedimentary layer, the water flows (small in magnitude compared to the volume of the permeable, saturated sedimentary layers) are not detectable at the surface. However, a significant quantity of water from within the waste disposal zone is seen to migrate above and beyond the crystalline rock layers over 100 – 10,000 yr timescales. These values are significantly higher than the upflows simulated in previous studies (Brady et al. 2009; Arnold and Hegdu 2013), most likely due to variations in the mesh geometry and refinement (previous studies used coarser meshes, and thus will represent different cross-sectional areas for the disturbed-rock zone than stated in the well-design specifications) as well as the increased pressure in the waste disposal zone due to increased heating from interacting wellbores. Note also that after t = 20,000 yr, the cooling system is now subject to downward water flows (negative Q_W) as thermal expansion of deep fluids is replaced by contraction due to cooling.
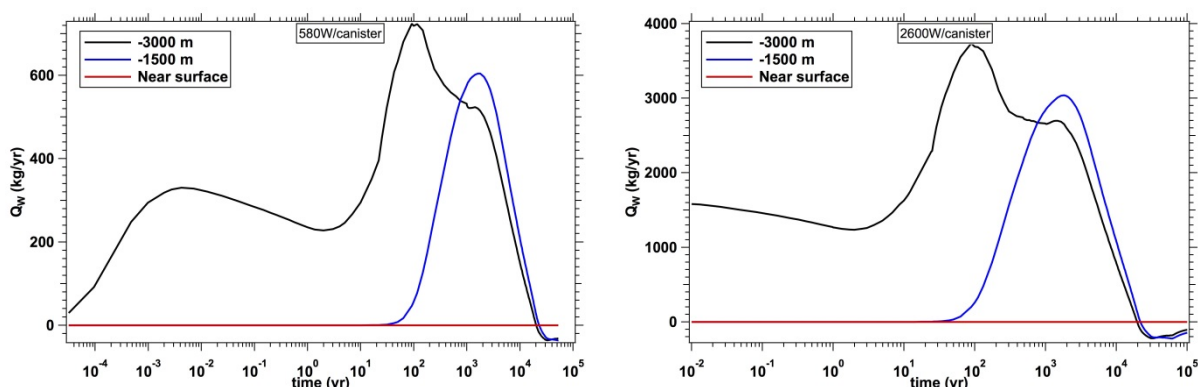
Figure 4.3.7. Total water flow in the disturbed rock zone adjacent to the wellbore at z = -3,000 m, -1,500 m, and -500 m (r = 0 m) for 580W (left) and 2,600W (right) canisters.

To assess sensitivity of the pressure changes and resulting flow rates, the permeability of the disturbed-rock zone was increased by a factor of 10 (k_{DR} = 2.0 mD) and the permeability of the sealed borehole was increased by factors of 10 and 100 (k_{SW} = 1.0 mD, 10.0 mD). The pressure evolution of the system with increased disturbed-rock permeability compared to the base case is sown in Figure 4.3.8. Increased permeability in the pathway surrounding the wellbore decreases the pressure changes by approximately 50%. This is the result, seen in Figure 4.3.9, of significantly increased upward fluid flow in the disturbed-

rock zone despite the nearly identical thermal evolution of the system. However, the system shows no sensitivity to increased permeability within the sealed wellbore zone—increasing k_{SW} by factors of 10 and 100 gives pressure and fluid-flow values roughly identical to the base case for both 580W and 2,600W waste packages.
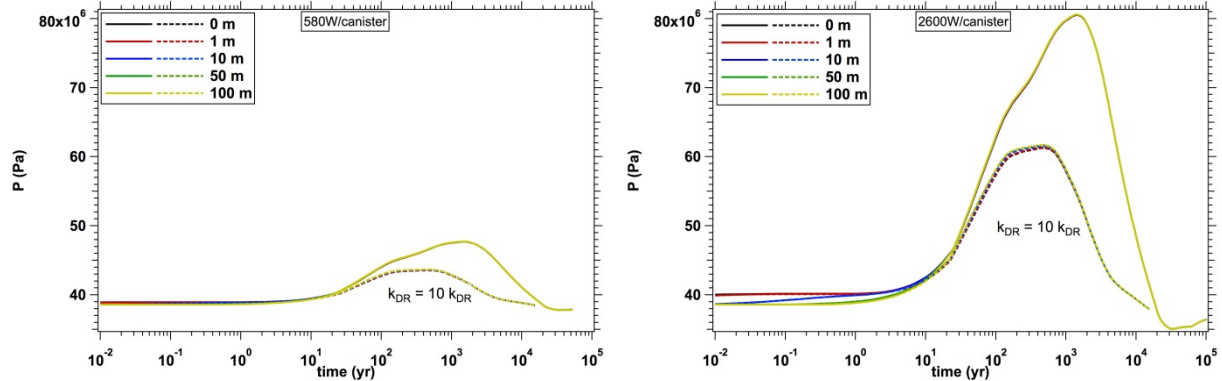
Figure 4.3.8. Pressure evolution adjacent to the wellbore at z = -3,000 m, -1,500 m, and -500 m (r = 0 m) for 580W (left) and 2,600W (right) canisters for the base disturbed-rock permeability and for a 10X increases in permeability.
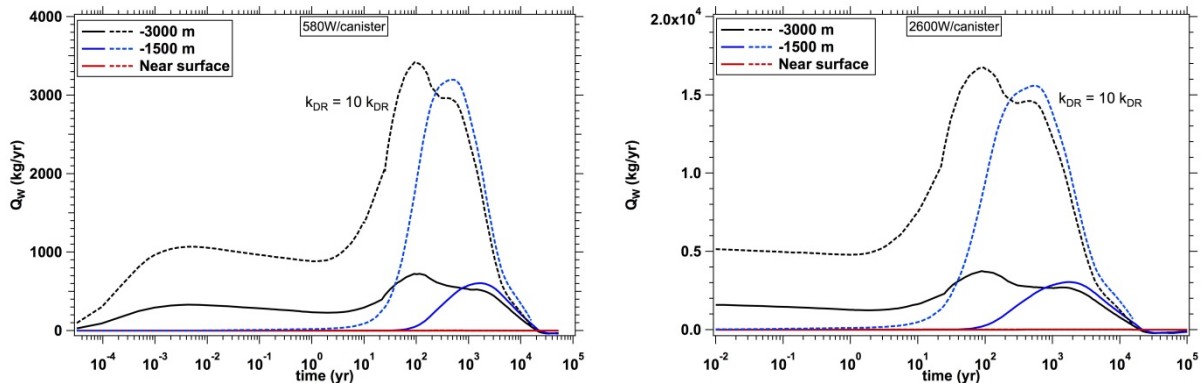
Figure 4.3.9. Total water flow in the disturbed rock zone adjacent to the wellbore at z = -3,000 m, -1,500 m, and -500 m (r = 0 m) for 580W (left) and 2,600W (right) canisters for the base disturbed-rock permeability and for 10X increases in permeability.

4.3.4   TH Modeling Conclusions

The presence of a large field of wellbores and the resulting interactions between them are expected to result in greater maximum temperature and pressure changes than seen for isolated boreholes, and also create a second peak in temperature and pressure as boreholes interact at later times. This results in greater upflows of water at later times than seen in earlier studies. These results are likely different from previous work due to variations in permeability (especially crystalline rock) and variations in the porosity/volume of the wellbore/disturbed-rock regions (a function of mesh discretization near the borehole). Modification of the disturbed-rock radius (possibly through simple relabeling of near-wellbore mesh elements to alter the radius of higher permeability) will be used to evaluate this.

A further step in simulation development will be to add salt in (varying concentration with depth) to the water in the crystalline rock zone. This will involve the use of the EWASG EOS module for TOUGH2 (Battestelli 1997) in place of EOS4, and the conversion of the existing input files and initial conditions.

The addition of salt (and the resulting increase in density of the deeper fluids, as well as the role of salt as a tracer) will also help distinguish between upward flow due to thermal expansion vs. upward flow due to buoyant convection of heated fluids.

4.4   Proposed THM and Disturbed Zone Modeling

THM and disturbed zone modeling is proposed to be conducted at multiple scales to be able to model both the large-scale stress evolution and the detailed evolution of the disturbed zone. First, a 3D THM quarter symmetric model will be used to calculated temperature, pressure and stress evolution (Figure 4.4.1). In this model, the goal will also be to model the steps (shown as steps 1 to 8 in Figure 4.4.1) from drilling to the long term behavior and return to ambient conditions.
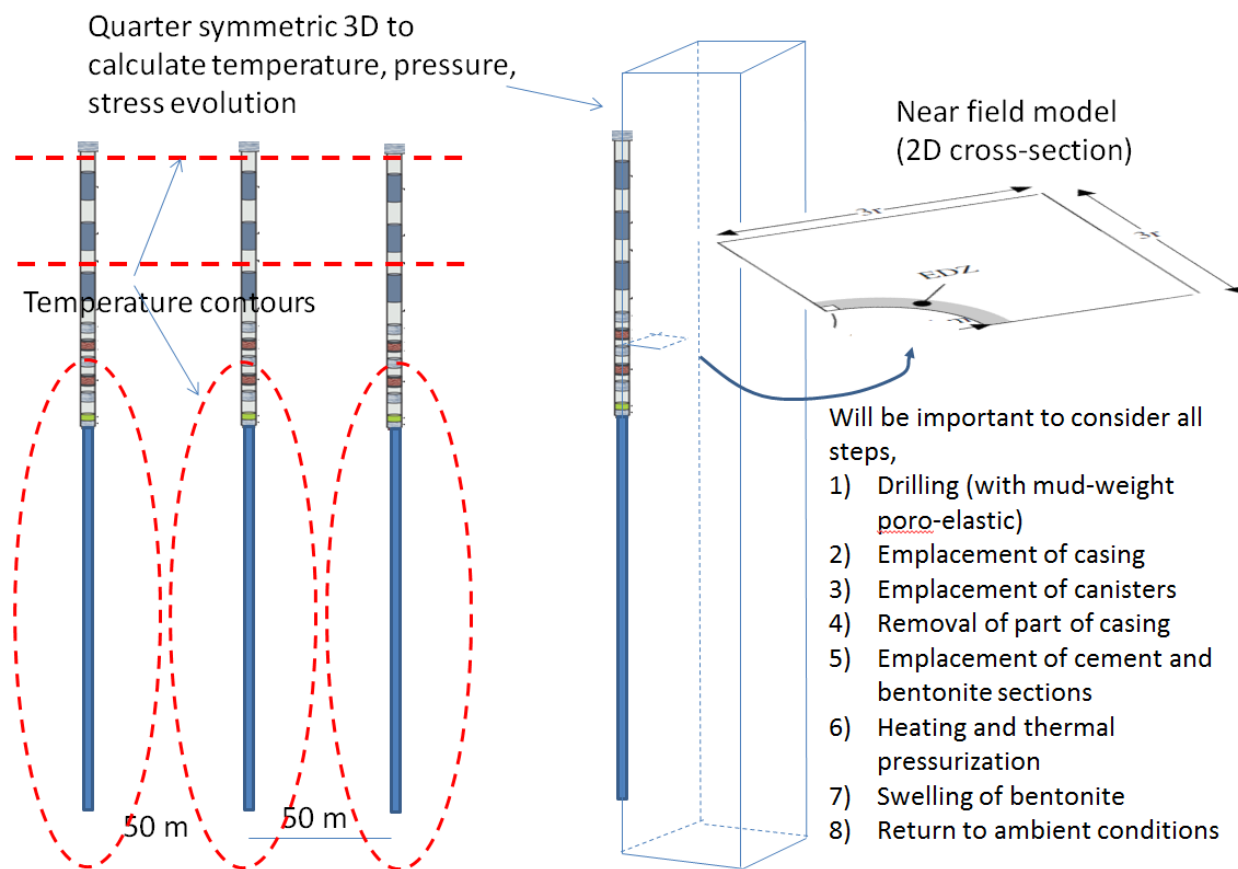
Figure 4.4.1. Overview of THM modeling approach

The disturbed zone modeling would, including calculation of the evolution of the damage and permeability changes over time. A few approaches may be applied with increasing complexity as follows:

1. Simple stress-permeability model (mean and deviatoric stress vs permeability) with *in situ* calibrated parameters at the Manitoba URL in Canada (tight granite)

2. Anisotropic damage model with anisotropic crack propagation under tensile and shear stress

3. Discrete fracture propagation model (TOUGH-RBSN) 2D cross-section model

The first alternative has been done in practice by Rutqvist et al. (2009) as shown in Figure 4.4.2. In this case a model involving how permeability changes with deviatoric (shear) and mean effective stress for competent (intact) granite. Permeability increases of up to 4 orders of magnitude were measured during

excavation of the tunnel, some of which were stress-induced and some of which were induced by excavation operation. The second alternative would include a constitutive model for anisotropic damage which would involve a mechanistic coupling between stress-induced anisotropic damage and anisotropic permeability changes. The third alternative involves modeling of discrete propagation and damage using TUOGH-RBSN in a 2D cross-section as shown in Figure 4.4.3. Using this model we will be able to study and address issues related to the size of the hole, in relation to observations of spalling strength at tunnels and laboratory experiments. The idea is to extract stress, temperature and pressure evolutions from the large scale 3D model and apply it as time-dependent stress boundaries and internal temperature and pressure conditions on the 2D disturbed zone model.

In the modeling, the effect of the bentonite and concrete plugs needs to be considered in the modeling. Various mechanical models for bentonite behavior may be applied, from a simple linear swelling model to more complex mechanical constitutive models, such as the Barcelona Basic Model (Rutqvist et al. 2011).
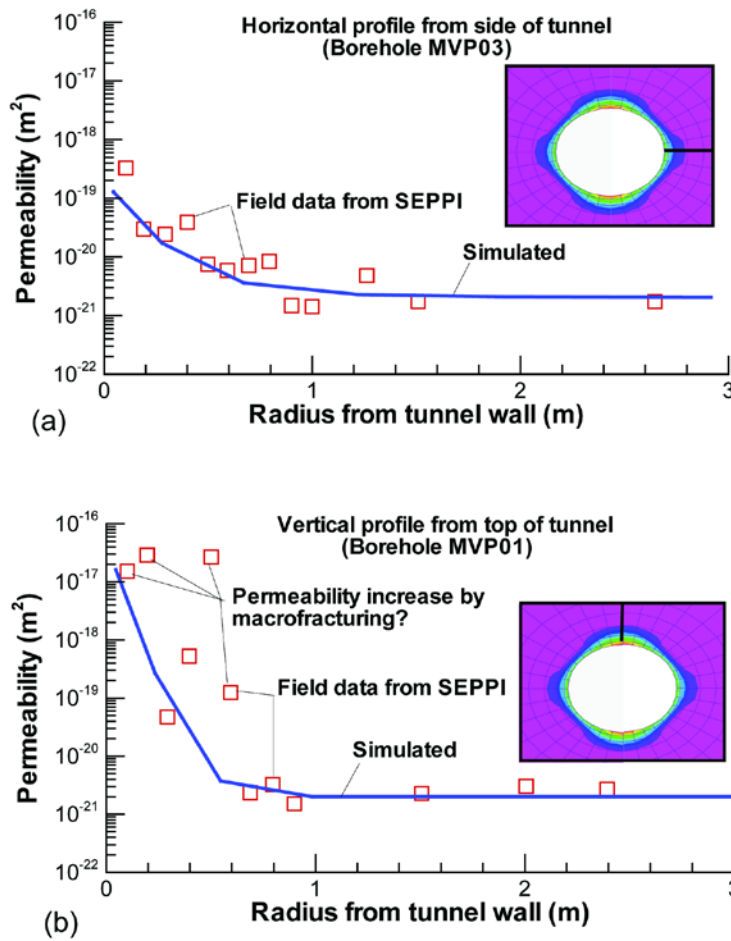
Figure 4.4.2. Calculated and measured permeability changes around the TSX tunnel (Rutqvist et al. 2009). Permeability versus radius along (A) a horizontal profile from the side of the tunnel and (B) a vertical profile from the top of the tunnel.
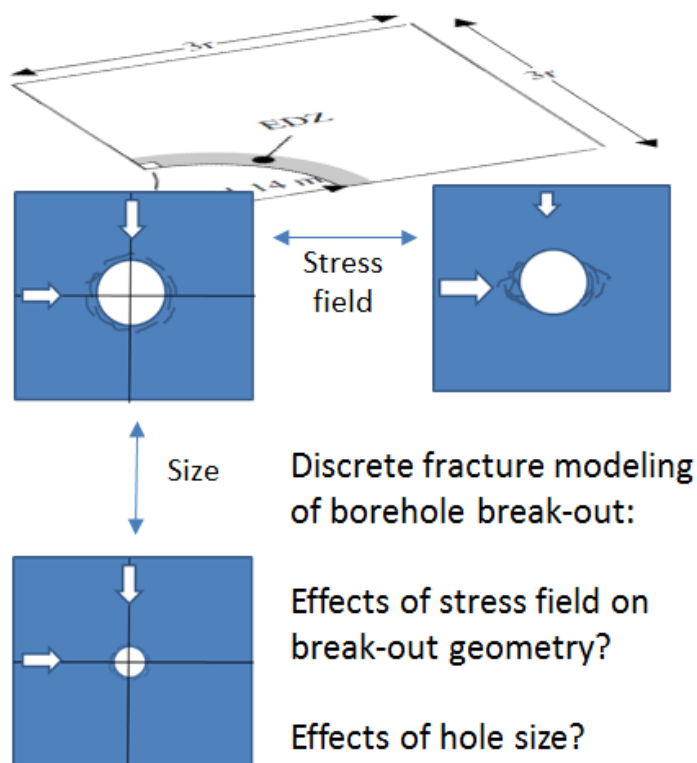
Figure 4.4.3. Concepts of TOUGH-RBSN detailed modeling of discrete damage around the borehole translating into borehole break-out and permeability changes.

4.5   Status of Seal Modeling and FY17 Plans

Based on our initial brief review in this report we conclude that the evolutions of the disturbed zone (including spalling and break-out) and seals through different stages of disposal development are key issue for the long-term performance of a deep borehole repository.

We have in FY16 completed a number of TH simulations with evaluate upflow along the disturbed zone with assumed permeability, considering thermal pressurization. The TH analysis will next be completed by including variations in permeability and in the porosity/volume of the wellbore/disturbed-rock regions, as well as adding salt in (varying concentration with depth) to the water in the crystalline rock zone.

In FY17 we plan to extend modeling activities to THM and THMC processes modeling of the seal and disturbed zone. Specifically, coupled THM simulations of seal and disturbed zone evolution and associated upflow will be conducted using a multi-scale modeling approach as described in Section 4.5. It will be very important to evaluate the seal and disturbed zone evolution, because in the current planned deep borehole field test, the two deep boreholes (characterization and emplacement boreholes) will be left open (not sealed) as observatories, so *in situ* seal behavior will likely not be tested. In this context, proposed *in situ* seal experiments involving packer tests to evaluate permeability changes and flow though disturbed zone rock will be important for model validation and calibration of disturbed zone properties. Thus, in FY17 we propose to model such an experiment, to use modeling for pre-test design and later for interpretative analysis of the actual experiment. Another important component of the seal modeling will be to evaluate the function of bentonite seals at greater depth, including the effect of swelling and support of the borehole walls during thermal stress peak. Finally, the THM modeling will eventually be expanded

to consider THMC processes, such as the effect of salinity on the swelling capacity of bentonite seals, as wells as chemical interactions between seals, ballast and cement plugs.

4.6   References

Arnold, B.W., and Hagdu, T. 2013. Thermal-hydrologic modeling of a deep borehole disposal system. Proc. Int. High-Level Radioactive Waste Conference, Albuquerque, NM, Apr.

Andersson, J.C., and Martin, C.D. 2009 The Äspö pillar stability experiment: Part I—Experiment design. International Journal of *Rock Mechanics & Mining Sciences*, 46, 865–878. .

Battestelli, A., Calore, C., Pruess, K. 1997. The simulator TOUGH2/EWASG for modeling geothermal reservoirs with brines and non-condensable gas. *Geothermics*, 26(4), 437-464.

Brady, P.V., Arnold, B.W., Freeze, G.A., Swift, P.N., Bauer, S.J., Kanney, J.L., Rechard, R.P., Stein, J.S. (2009). Deep Borehole Disposal of High-Level Radioactive Waste, Report SAND2009-4401, July 2009.

Brown ET and Hoek E (1978) Trend in relationship between measured in situ stresses and depth. International Journal of Rock Mechanics and Mining Sciences15: 211-215.

Brudy, M., Zoback M.D., Fuchs K, Rummel F., and Baumgärtner J., 1997 Estimation of the complete stress tensor to 8 km depth in the KTB scientific drill holes: Implications for crustal strength. Journal of *Geophysical Research*, 102, 18,453-18,475.

Bäckblom, G., Martin, C.D. 1999 Recent experiments in hard rock to study the excavation response: Implication of the performance of a nuclear waste geological repository. Tunnel Underground Space Technol 14:377–394.

Greenberg, H.R., Wen, J., Buscheck, T.A. 2013. Scoping Thermal Analysis of Alternative Dual-Purpose Canister Disposal Concepts. LLNL-TR-639869, June, 2013.

Juhlin, C., Wallroth, T., Smellie, J., Eliasson, T., Ljunggren, C., Leijon, B., Beswick, J. 1998 The Very Deep Hole Concept – Geoscientific appraisal of conditions at great depth. Swedish Nuclear Fuel and Waste Management Co. Technical Report 98-05.

Lund, B., and Zoback, M.D., Orientation and magnitude of *in situ* stress to 6.5 km depth in the Baltic Shield. International Journal of Rock Mechanics and Mining Sciences 36 (1999) 169-190.

Pruess, K., Oldenburg, C.M., Moridis, G.J. 1999. TOUGH2 Users Guide, Version 2. LBNL report 43134

Read R.S. 20 years of excavation response studies at AECL's Underground Research Laboratory. *International Journal of Rock Mechanics & Mining Sciences* 41 (2004) 1251–1275

Rutqvist, J., 2015 Fractured rock stress-permeability relationships from *in situ* data and effects of temperature and chemical-mechanical couplings. *Geofluids*, 15, 48–66.

Rutqvist, J., and Stephansson, O., 2003 The role of hydromechanical coupling in fractured rock engineering. *Hydrogeology Journal*, 11, 7–40.

Rutqvist, J., Börgesson, L., Chijimatsu, M., Hernelind, J., Jing, L., Kobayashi, A. and Nguyen, S., 2009 Modeling of damage, permeability changes and pressure responses during excavation of the TSX tunnel in granitic rock at URL, Canada. Environmental Geology, 57, 1263–1274.

Rutqvist, J., Ijiri, Y. and Yamamoto, H. 2011 Implementation of the Barcelona Basic Model into TOUGH-FLAC for simulations of the geomechanical behavior of unsaturated soils. *Computers & Geosciences*, 37, 751–762.

Rutqvist, J., Zheng, L., Chen, F., Liu, H.H., and Birkholzer, J., 2014 Modeling of Coupled Thermo-Hydro-Mechanical Processes with Links to Geochemistry Associated with Bentonite-Backfilled Repository Tunnels in Clay Formations. *Rock Mechanics and Rock Engineering*, 47, 167–186.

Xu, T., Sonnenthal, E.L., Spycher, N., and Pruess, K., 2006. TOUGHREACT - A simulation program for non-isothermal multiphase reactive geochemical transport in variably saturated geologic media: Applications to geothermal injectivity and CO_2 geological sequestration, *Computers & Geosciences*, v.32, p.145-165.

5.   SEAL EXPERIMENTS

5.1   Introduction

Because the seal section of the borehole used for the waste disposal is expected to be at large depth (~3 km or deeper), the borehole wall will be subjected to significantly high stresses from the overburden and possible tectonic forces. The resulting stress concentrations on the borehole wall can cause spalling and buckling failure of the rock (borehole breakout), and tensile fracturing under extremely high levels of stress anisotropy, which compromises the integrity of the waste repository by providing bypassing permeability in the rock around the seals (Figure 5.1.1). The primary objectives of the experiments are to investigate (1) the geometry of the damage around a borehole (borehole breakout, tensile fracturing) within crystalline rock under high stress, (2) the hydrological properties of the damage zone, and (3) the hydrological-mechanical-chemical (HMC) changes of the damage zone and the seal materials (cement, bentonite) via diffusion and transport of fluid (water), once the seal is placed within the borehole. The effect of temperature may be important especially for chemical changes. However, for experimental simplification, at this moment the experiments are planned to be conducted at ambient temperature (up to ~60ºC). For the HMC study, both short-term changes (clogging of the fractures by transport and swelling of clay particles) and long-term changes (chemically induced mineral precipitation and dissolution) in the permeability of the damage zone and the rock and seal are of interest.

During FY2016, we started a laboratory investigation of borehole seal integrity by designing and conducting preliminary laboratory borehole breakout experiments under high stress (>100 MPa). In the following, we will describe the experimental setups and the results of the preliminary experiments.
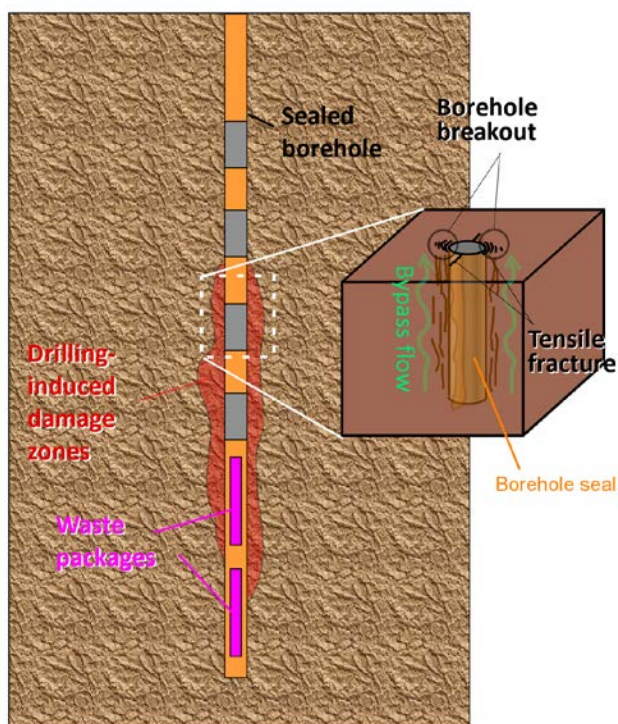
Figure 5.1.1. Permeability increases around a borehole caused by damage zones

5.2   Experimental design

5.2.1   Rock sample selection

One critical problem with the scaled laboratory borehole breakout experiments using a small, analogue borehole is that the geometry of the induced damage can be strongly dependent upon the size of the mineral grains and microcracks. For example, for a field borehole with a diameter of 0.5 m and an analogue laboratory borehole of 1 cm, a 1-mm-size grain within a common granite sample in the laboratory scales to an unrealistically large, 5 cm block. To avoid this problem, we selected ultra-fine-grain Arkansas novaculite (fine-grain quartzite) for our tests. The sample blocks were obtained from a novaculite quarry (Figure 5.2.1 (a); Dan's Whetstone Company, Inc. AR.).

The particular kind of black, novaculite our study uses has uniform grain sizes with a mean diameter of ~10μm (Figure 5.2.1 (b)) which corresponds to reasonable ~0.5mm grain size in the field.

(a) Novaculite boulders at the vendor quarry
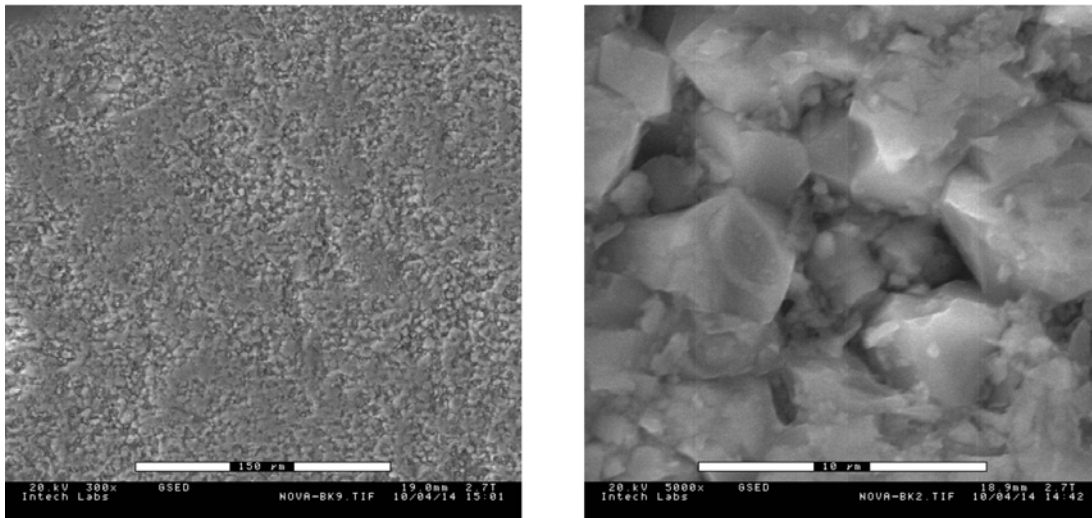
(b) SEM images of the samples

Figure 5.2.1. Black Arkansas Novaculite samples (Courtesy, vendor)

5.2.2   Experimental stress state

Because rock failure depends upon the strength characteristics of particular rocks, the use of *in-situ* stress is not necessarily consistent with the use of the "analogue" *in-situ* rock. Because of the uniform and fine grain size, the novaculite sample used in our experiment is expected to be much stronger than *in-situ* rock which has more heterogeneous mineral compositions and size, and larger grains and microcracks. Nevertheless, we assume a possible *in-situ* stress state scenario and use it as a guideline to design our experiments.

The major constraint on the experiment is the loading capability of our true-triaxial loading system. This system consists of a small lateral (X-Y) frame and a high-capacity vertical (Z) frame. The maximum applicable forces are 16,800 lbf (74.7 kN) and 115,050 lbf (512 kN), respectively. For a 2-inch (5.08 cm) cube sample, the resulting stresses are $(\sigma_x, \sigma_Y, \sigma_Z)$=(29 MPa, 29 MPa, 198 MPa). The depth of the expected in-situ borehole at the seal depth is assumed to be ~3km. For a rock density of ~2650 kg/m^3, the resulting overburden stress is ~80 MPa. Although the actual *in-situ* horizontal stresses are not known at this point, the above maximum applicable horizontal stress (29 MPa) appears to be too small for inducing a borehole breakout in our competent, crystalline rock. Although the stress can be increased by reducing the overall sample size in all dimensions, we decided against it because the scale of the laboratory experiment is already very small.

In order to increase the stress applied to induce borehole breakout using currently available equipment, we designed and fabricated two sets of experimental setups (Figure 5.2.2). The first setup (the "triax" test) uses a rock slab containing a center hole (Figure 5.2.2 (a)). The reduced thickness (1.27 cm instead of 5.08 cm) increases the applicable maximum horizontal stresses to 116 MPa. The second setup (the "box" test) uses a 2-inch cube sample containing an analogue borehole (Figure 5.2.2 (b)), but the experiment is conducted while constraining the lateral deformation of the sample. The rock samples were machined with high precision to our specifications by D. K. Milovic Company, Inc., CA (Figure 5.2.3).

| (a) "Triax(ial)" test platens | (b) "Box" test platens |
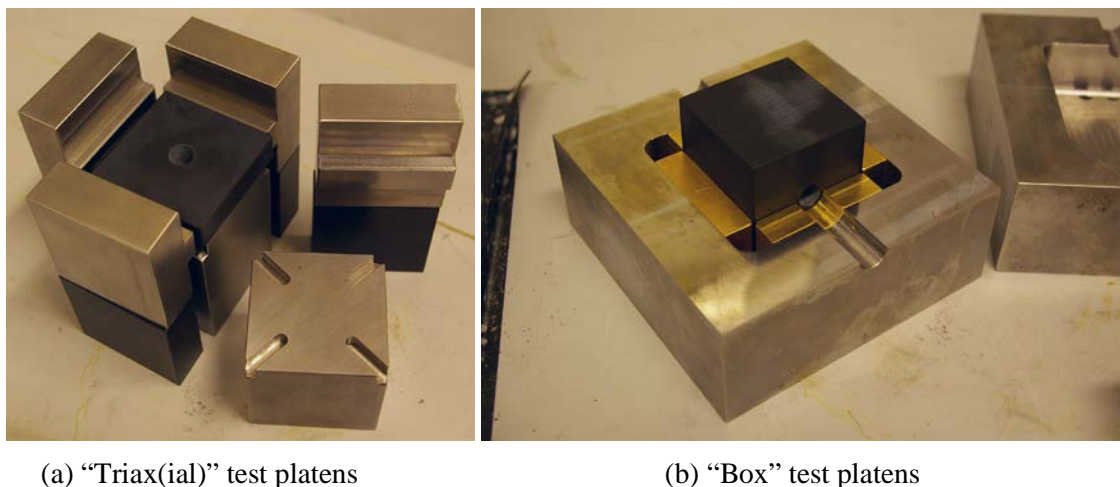
Figure 5.2.2. Loading platens used for laboratory borehole breakout experiments
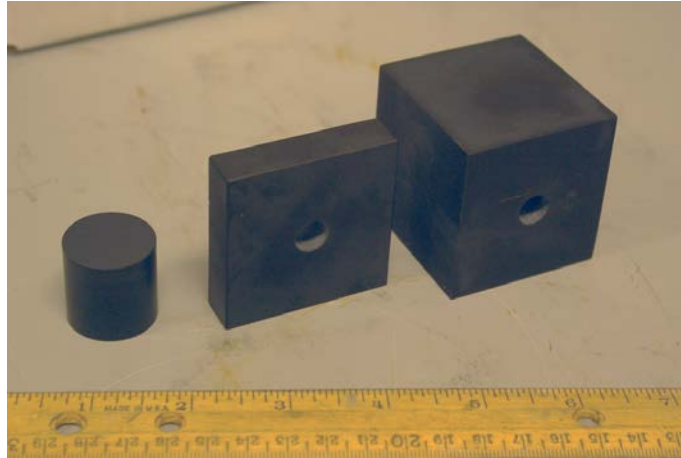
Figure 5.2.3. Three geometries of novaculite samples used in the experiment. From the left, cylindrical core (used for seismic velocity measurements and permeability tests), thin slab sample and cube sample containing an analogue borehole.

The box experiment can be conducted by applying only the vertical stress to the sample which can have relatively large maximum applicable stress. (The stress can be increased by increasing the drive pump pressure, if necessary.) The sample is held between a pair of split metal boxes made of alloy steel and brass inserts (Figure 5.2.2 (b)). Vertical stress, which is the maximum principal stress, is applied to a direction perpendicular to the borehole in the box, and the remaining two principal stresses are applied via reaction forces from the box walls, resulting from the Poisson expansion of the sample. Low Poisson ratios (less than 0.25 if the box is rigid), however, can result in tensile stress in the maximum principal stress direction around the borehole, producing tensile fractures (Figure 5.2.4).
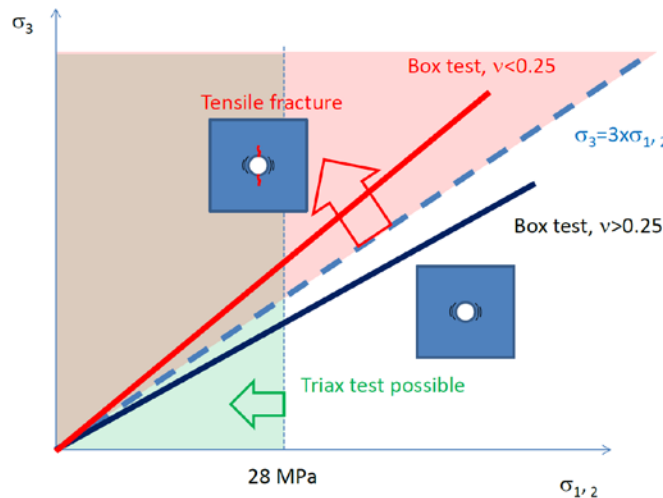
Figure 5.2.4. Stress regimes in the "triax" and "box" tests. For the triax test, the three principal stresses can be controlled independently, but only limited horizontal (borehole-perpendicular) stresses can be applied. For the box test, the horizontal stresses are the function of the rock's Poisson ratio, which may result in tensile failure of the rock if the Poisson's ratio is too low.

5.3   Preliminary Experiments

5.3.1   Strength measurement (Uniaxial Compression Tests)

Published data on the strength of novaculite are very scarce and the only data we could find was the dynamic tensile strength (67–88 MPa) (Cohn and Ahrens, 1981). This high tensile strength indicates that the compression strength is very high. We conducted a series of uniaxial compression tests on small subcores (diameter 0.56 inches x length 1.25 inches) taken from one of the cube samples obtained from the same quarry as the other samples. The experiments were conducted under undrained conditions at room temperature. The average density of room-dry samples was 2.646 g/cm^3, which is very close to the density of α-quartz (2.648 g/cm^3). To assess the water content and/or permeability of the sample, we measured the apparent density of a cylindrical, originally room-dry (as received from a commercial rock cutting service company) core (1.00" diameter, 1.00" length) within a drying oven over time at 60$^{\mathrm{o}}$C (Figure 5.3.1). The very small reductions in the density indicate that the rock has either extremely small porosity or permeability.
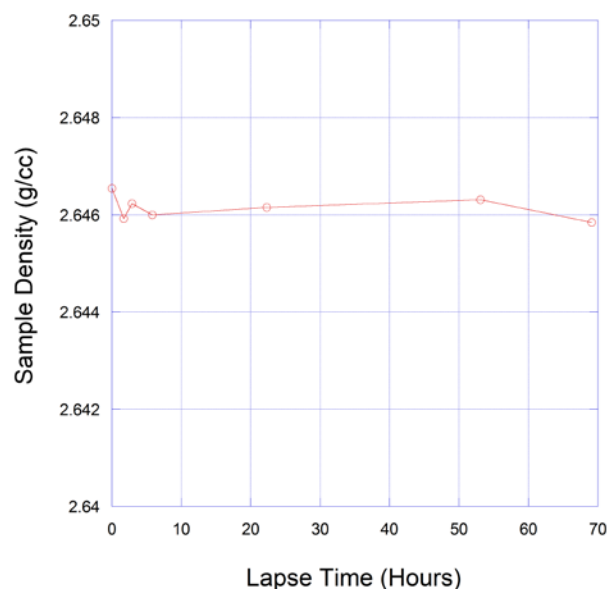
Figure 5.3.1. Measured density changes of novaculite core from the original room-dried state.

The compression tests were conducted at an approximate strain rate of 0.01%/minute. In the first test, the ultimate strength of the sample exceeded 425 MPa (at this stress the experiment was terminated). The other two tests also resulted in very high ultimate strength exceeding 370 MPa (Figure 5.3.2). These results indicated that the load required to produce borehole breakout in the rock will not be achievable using our equipment. To reduce the strength, two cases of heat treatment were considered, where the samples were placed in a furnace at 800°C for 12 hours and at 1,000°C for 24 hours, respectively. Although the strength of the sample still exceeded 300 MPa for both heat-treated samples, there were significant reductions, which may allow us to induce borehole breakout. The sample density also decreased to 2.577 g/cm^3 (800°C 12 hours) and 2.566 g/cm^3 (1,000$^{\mathrm{o}}$C for 24 hours), respectively, indicating a loss of fluid from the sample, possibly through newly opened microcracks.

As the stress-strain relationships in Figure 5.3.2 show, there are multiple, discrete stress drops with small changes in the elastic moduli (from the slope of the curves) for all of the samples. These are caused by prominent, vertical slabbing of the samples, resulting from the very brittle nature of the rock. Figure 5.3.3 shows the photographs of the samples before and after the experiment. The sample from the experiment terminated before the ultimate failure was reached exhibits two distinct fractures, corresponding to the

two stress drops (or "saw teeth") in the stress-strain curve in Figure 5.3.2. For the failed sample, the rock was completely fragmented. X-ray CT images of the failed samples (which reached the ultimate failure) reveal that multiple near-vertical fractures are prevalent within the samples, while the buckling of the columns between the fractures and some crushing of the core at the ends seem to have led to the ultimate failure (Figure 5.3.4). These observations indicate that within the novaculite used in our experiment, borehole-breakout-induced fractures will be subparallel to the borehole wall and can be densely spaced, in contrast to compaction and shear-types breakouts in highly porous and ductile rocks.
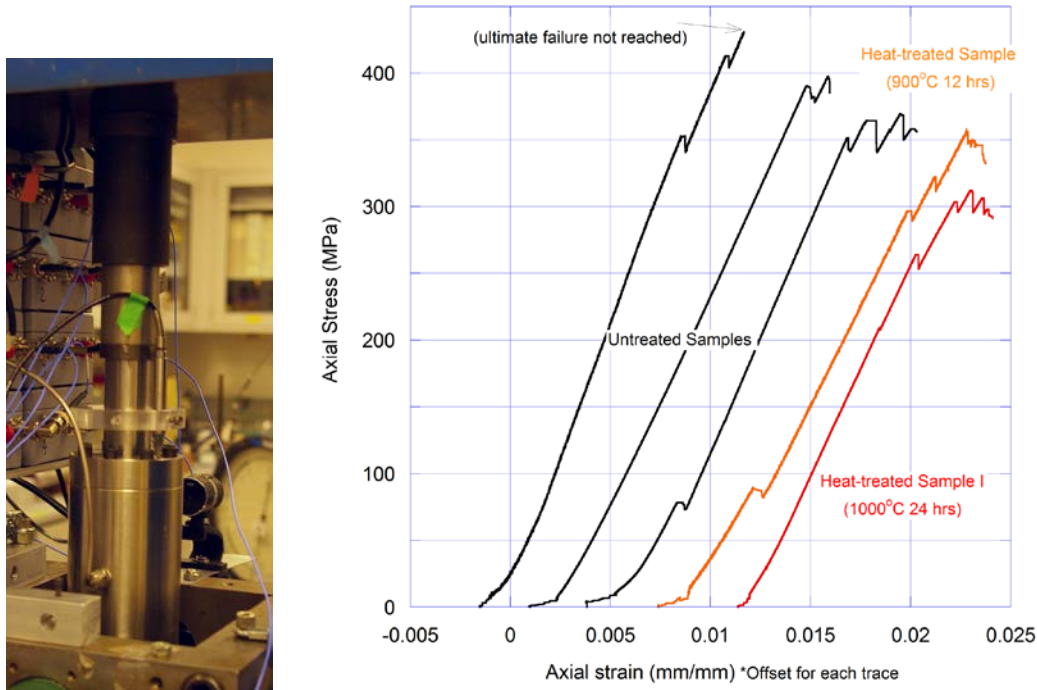
Figure 5.3.2. Uniaxial compression tests on five novaculite cores. The cores are 0.55 inches in diameter and 1.25 inches in length. Note that the axial strains were not corrected for the deformation of the metal end plugs and the sample-endplug interfaces. The "sawteeth" in each curve corresponds to formation of a vertical fracture within a core.
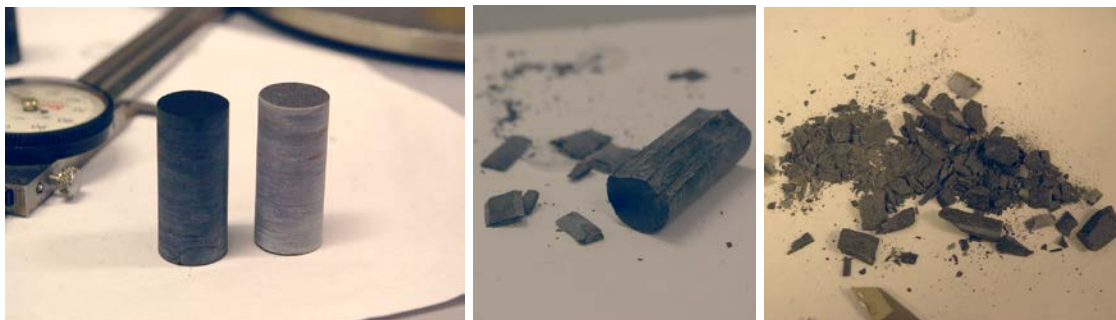
(a) Intact samples   (b) Core-parallel fracturing (c) Complete disintegration

Figure 5.3.3. Photographs of novaculite cores before and after the experiment. A sample for which the experiment was terminated prematurely shows distinct, core-parallel fractures corresponding to the sawteeth in the stress-strain curves (b). Upon failure, the sample disintegrated into small pieces (c).
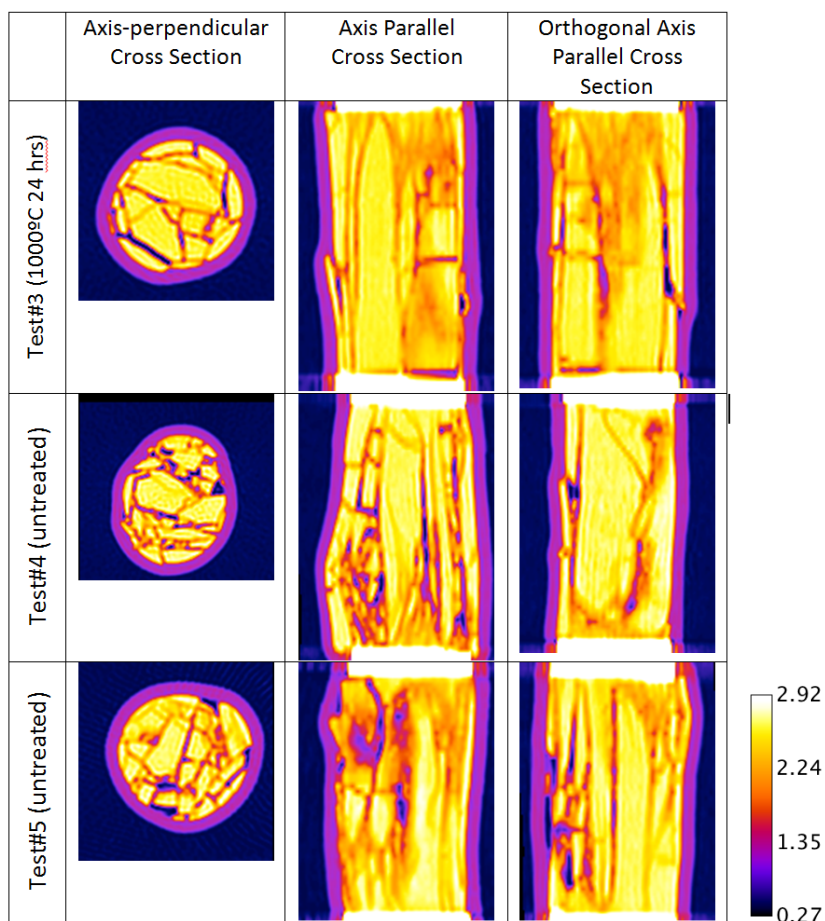
Figure 5.3.4. Post-test X-ray computed tomography scans of cylindrical 0.56 in diameter novaculite cores (after ultimate failure). Pervasive core-parallel fracturing is evident. Also, buckling of the columns/slabs between the fractures, which we consider is responsible for the ultimate loss of the strength, is also clearly visible. The scans are calibrated to show density, with lighter colors indicating higher density (see lower right scale bar). Unfractured novaculite density is very uniform, and voxels containing fractures show lower density. The surgical rubber sleeve shows as purple here.

CT scans of the post-test samples show resulting fragments oriented parallel to the load axis. The 3-D image data file can be considered as being composed of a number of slices along an axis. The Feret's diameter (the longest distance between any two points along a particle boundary) of each particle in each slice is compared to the Feret's angle (angle of Feret's diameter, with 0 being along the left-to-right axis, and 90 being along the bottom–to-top axis) (see, for example, Ferreira and Rasband, ImageJ User Guide). For the core axis-perpendicular cross sections (first column of Figure 5.3.4), the Feret's diameters (Figure 5.3.5 (a)) are short and their angles show some order, as is expected from observing the images, but in general they are not along the bottom-to-top axis. For the axis-parallel cross sections, however, the particle lengths are much longer and tend to center around 90 degrees showing the vertical orientation (Figure 5.3.5 (b)).
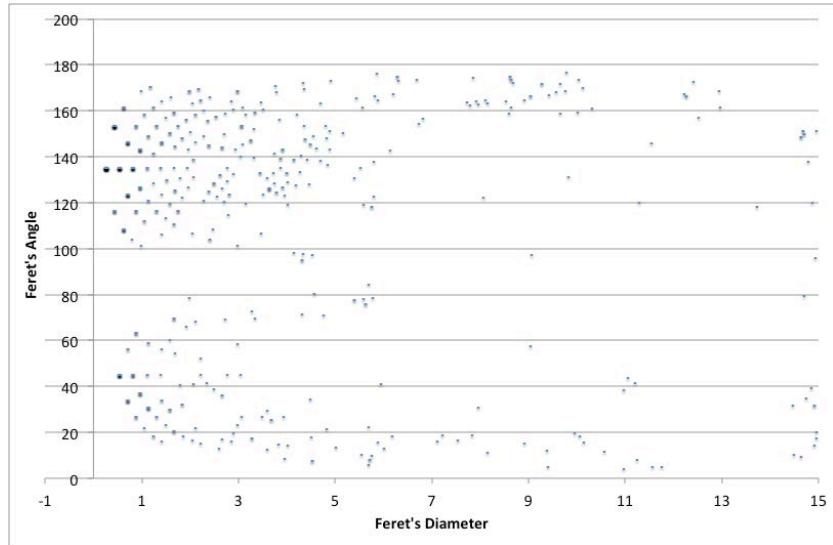
(a) Axis-perpendicular cross sections
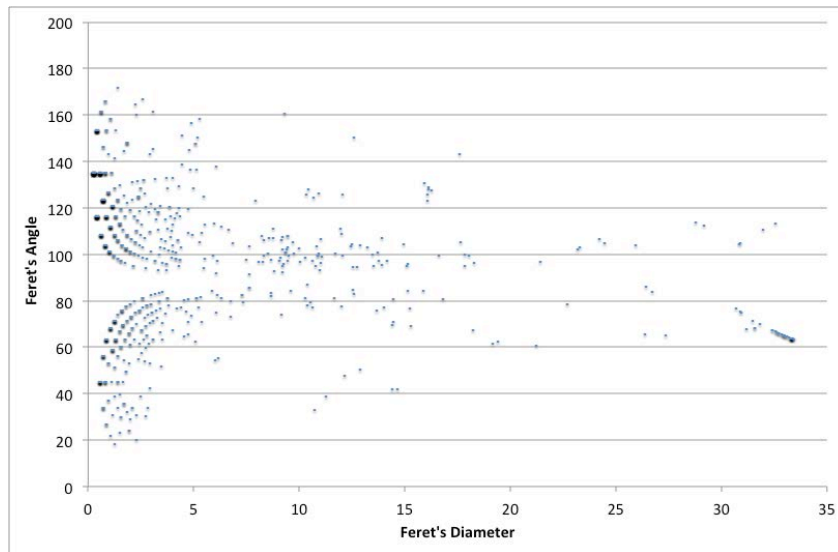
(b) Axis Parallel Cross Sections

Figure 5.3.5. Preferred fracture orientation analysis on X-ray CT image slices using the Feret's method. Concentration and symmetry of the "Feret particle" distribution along the 90-degree angle in the axis-parallel cross sections confirms vertical fracturing in the samples.

Moduli measurement (Ultrasonic velocity measurements): Elastic moduli of the samples were determined using ultrasonic wave velocities on room dry (untreated) samples and heat-treated (dried) samples. The results of the velocity measurements are presented in Figure 5.3.6. From the average P and S wave velocities and the density of the samples, the Young's and shear moduli are 93.4 GPa and 42.3 GPa (Poisson ratio 0.11), respectively. For untreated samples, the velocities indicated that the samples were nearly isotropic and homogeneous. In contrast, the heat-treated samples showed reductions in the seismic velocities (and therefore moduli). Figure 5.3.7 shows velocities measured in the small core samples used for the uniaxial compression tests. The velocities were measured along the axis of the core.
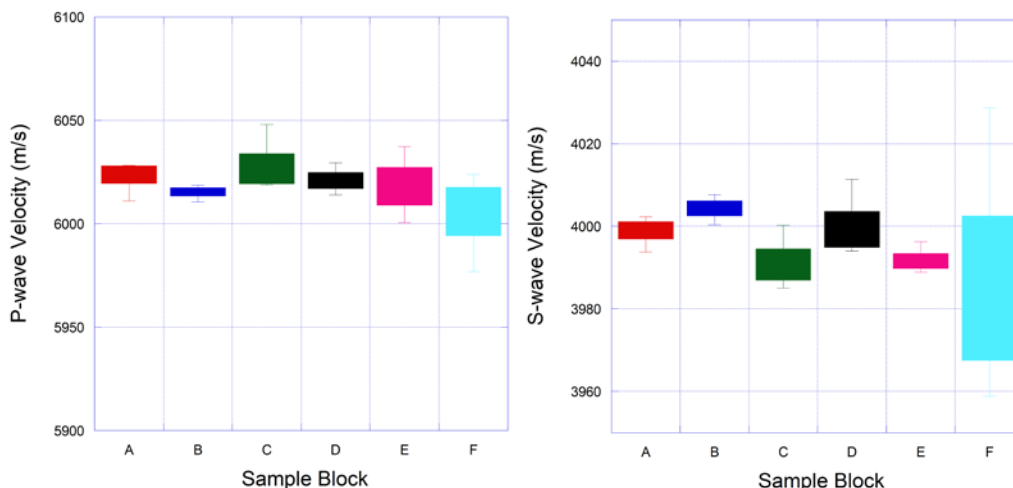
Figure 5.3.6. P and S-wave velocities measured for six, untreated 2-inch novaculite cubes. The measurements were made along the three perpendicular directions across the faces of the cubes. Except for cube F, both velocities vary very little between different directions and samples. Including cube F, the average P and S-wave velocities and standard deviations are 6,018±18 m/s and 3,996±15 m/s, respectively.
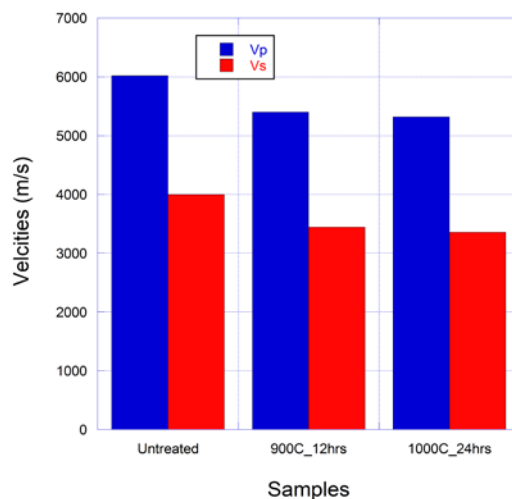
Figure 5.3.7. P and S-wave velocity changes due to heat treatment of the uniaxial compression test cores. Note that all these cores were taken from the same block, and were aligned in the same orientation.

In addition to the decreasing velocities, heat-treated samples also exhibited seismic anisotropy. In the 1-inch diameter, 1-inch tall core sample used for the permeability measurements in the following section, a heat-treated sample at 1,000ºC for 24 hours showed fast and slow P-wave velocities of 5,390 m/s and 4,900 m/s, and fast and slow S-wave velocities of 3,526 m/s and 3,371 m/s, respectively. The orientations of the fast and slow P waves and the polarization directions of the fast and slow S waves indicated the development of microcracks preferentially aligned parallel to a plane along a core axis. Because the velocity changes can be related to the degree of heat treatment via the impact of increasing microcracks in the rock, the seismic velocities (or moduli) and their anisotropy can be used to assess the impact of heat treatment on the rock strength.

5.3.2   Permeability measurement (Pressure-decay permeameter tests)

Permeability measurements of the novaculite samples with and without the heat treatment are underway using the pressure decay permeameter shown in Figure 5.3.8 (Finsterle and Persoff, 1997). In this technique, a well-defined volume of compressed gas is allowed to flow through the sample and into a well-defined downstream reservoir. The cylindrical sample is encapsulated on the round sides by a rubber sleeve through which the confining pressure is applied outside the sleeve, and steel endpieces are set against the flat sides. Each of the steel endpieces has a flow distribution pattern milled into it and is connected to the reservoir by a needle-like tube. The pressures of both reservoirs are monitored over time, with the upstream pressure decreasing and the downstream pressure increasing. The data are evaluated numerically using iTOUGH, to estimate the permeability, the Klinkenberg parameter, and other sinks like sorption or possible leaks. Since the reservoir volumes are small, even small leaks may result in large errors.
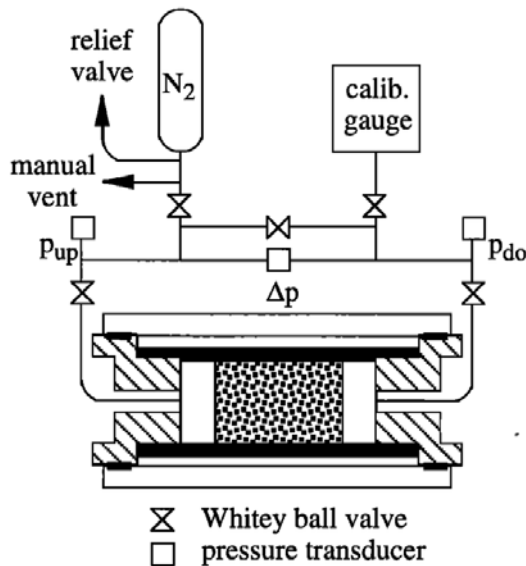
Figure 5.3.8. Pressure decay permeameter schematic and photo. Photo shows Enerpac jack used to apply confining pressure in front of the Hassler cell that holds the sample. The left gage is used to observe confining pressure. Pressure transducers (Transamerica-Delaval CEC 1000 - similar to Omegadyne PX1004) are used to measure upstream and downstream pressures, recorded by the data logger on the far right.

Two samples are being investigated initially, both from the same source. One of the samples has been heat treated in an oven to induce microfractures (direct observation via SEM is planned) (Figure 5.3.9). The heat treatment was intended to weaken the very strong novaculite. A number of measurements (typically three or more) are needed on each sample to enable high quality Klinkenberg parameter and permeability estimates. To date, only about half of these measurements have been completed, and the parameters have not yet been estimated. In spite of that, it is clear from Figure 5.3.10 that the permeability of the heat-treated sample is significantly greater than the untreated sample, consistent with the presence of abundant treatment–related microfractures. The results are also optimistic for the future of our test, as the permeability of our deep-borehole host rock analog is quantifiable under both conditions, thus making measurements of permeability change under loading conditions will be more manageable.
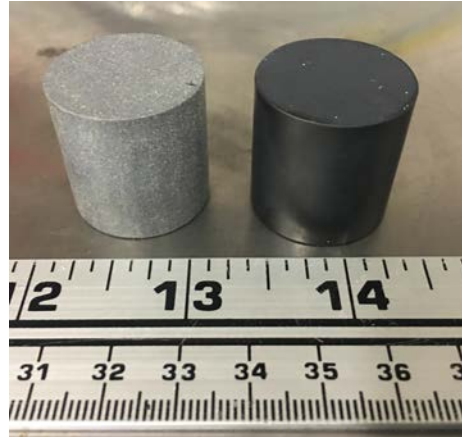
Figure 5.3.9. One-inch diameter novaculite samples. The left sample was heat treated after machining.
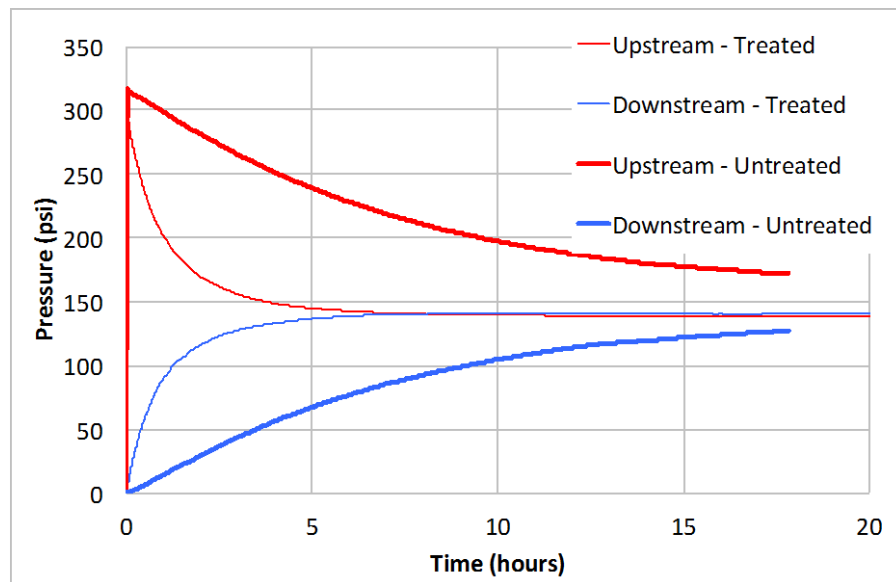
Figure 5.3.10. Raw data showing pressure decays of the two samples. Narrow lines are from the heat-treated sample, and heavy lines from the untreated sample. Some corrections are needed and slight room temperature effects are observed.

5.3.3   Borehole breakout experiment using a slab sample

Using the experimental setups described in Section 5.2, we conducted initial borehole breakout experiments on heat-treated novaculite samples. The block sample, however, fractured spontaneously during a 24-hour, $1,000^{\circ}$C treatment, possibly because of excessive thermal stress and heterogeneity within the sample (Figure 5.3.11 (a)). For this reason, we conducted the experiment using only a heat-treated slab sample (Figure 5.3.11 (b)).

The thin, slab sample was confined by the platen blocks shown in Figure 5.2.2 (a), and installed within the true-triaxial loading frame (Figure 5.3.12). In order to reduce friction at the sample-platen boundaries, 2-mil (~50-micron) thick PTFE sheets were placed at the interfaces. The platen blocks in contact with the wider (2 inches x 2 inches) faces of the sample contained grooves in which acoustic emission (AE) transducers can be installed. To reduce increased friction at the groove edges, additionally, 2-mil thick brass sheets with small windows for the AE transducers were also placed at the interfaces. A total of eight high-frequency, miniature AE transducers (Score Atlanta Inc., PICO Z sensors, frequency band 200kHz-800kHz)—four on each side of the slab—were used in this experiment. The AE data collection and processing was performed using an AMSY-6 acoustic emission measurement system (Vallen Systeme). The AE measurements were conducted continuously while the stress is applied to the sample so that the fracturing with the sample was monitored for its frequency, magnitude, and location.

During the experiment, the three principal stresses were applied independently, using syringe pumps (ISCO/Teledyne 260D and 500D) and hydraulic cylinders (Enerpac RSM1500 and Simplex R101). The stress history is shown in Figure 5.3.13. Initially, the stress was applied isotropically to the sample up to ~79 MPa. Subsequently, one of the horizontal stresses was increased further up to 116 MPa. From the Kirch solutions (2D elastostatic analysis, e.g., Jaeger et al. 2007), around a circular borehole, the maximum and minimum compressive stress should be 269 MPa and 121 MPa, respectively. Because no significant AEs were detected, the minimal principal stress was decreased first down to 39 MPa then to 0 MPa. This first reduction decreases the minimum compressive stress on the borehole wall predicted by the Kirch solution to zero, and the second step reduces it further to tensile.
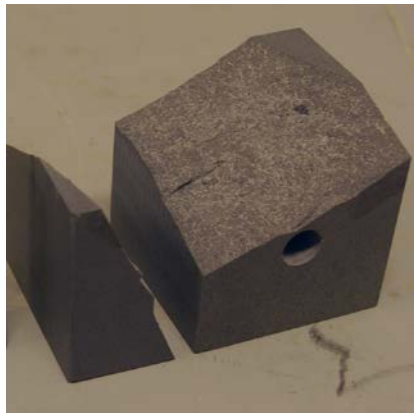
(a) Fractured, treated block sample   (b) Untreated (left) and treated (right) slab samples
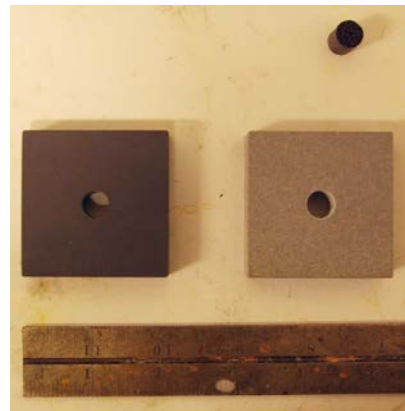
Figure 5.3.11. Thermally treated novaculite samples for laboratory borehole breakout experiment. The borehole diameter is 0.375 inches (~1 cm).
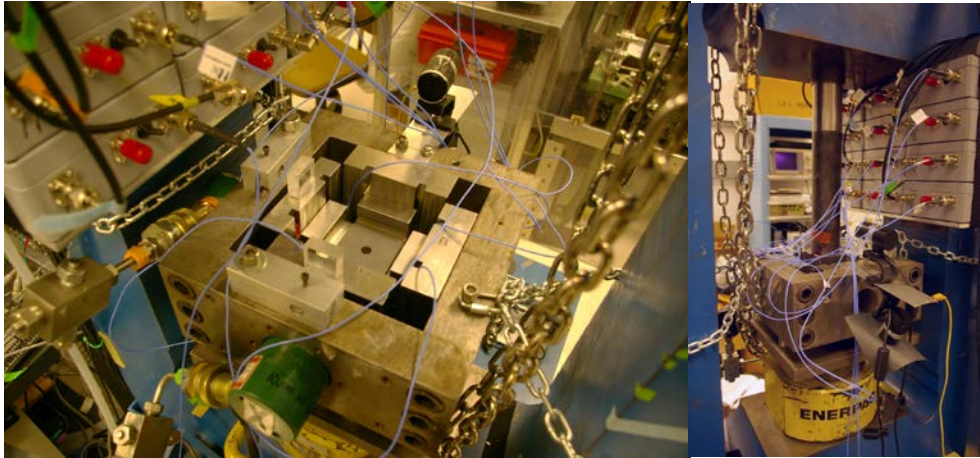
Figure 5.5.12. Installation of a slab sample (left) and assembled triaxial experiment (right). The blue wires are for acoustic emission sensors installed on the faces of the sample (right).
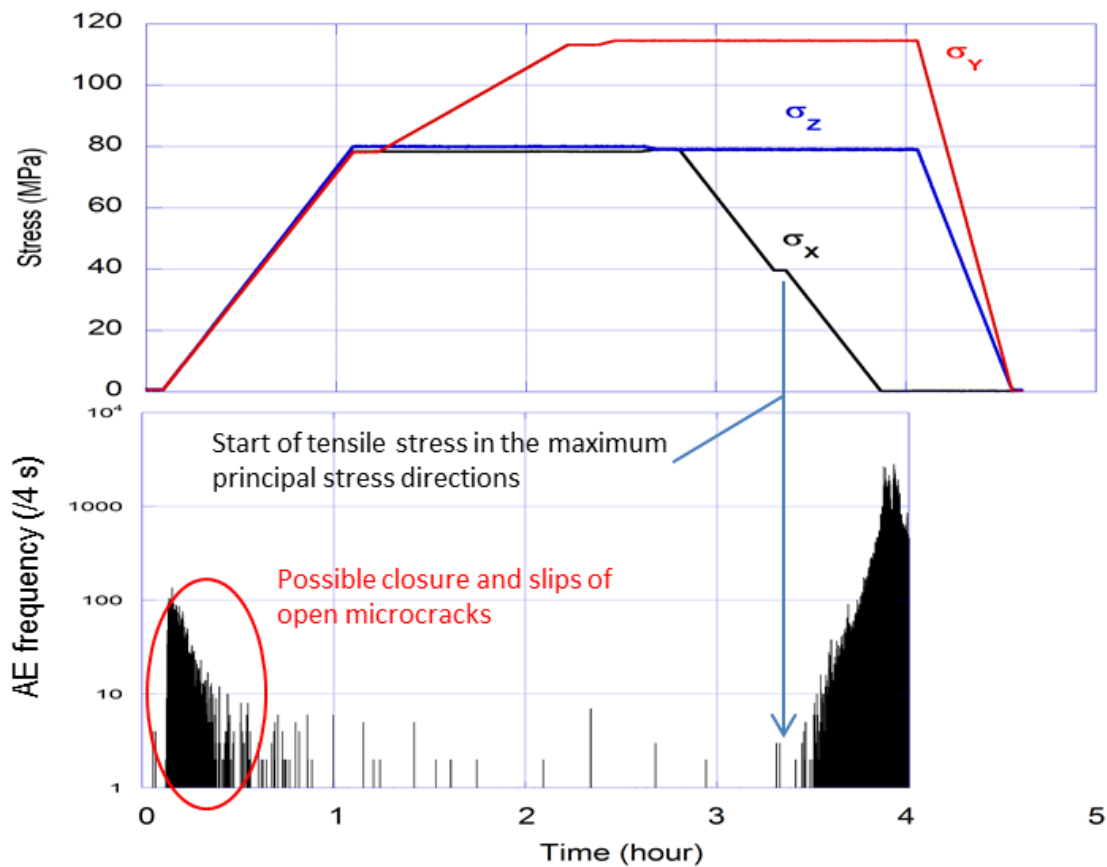
Figure 5.3.13. Stress history (top) and corresponding acoustic emissions (bottom) detected during the experiment.
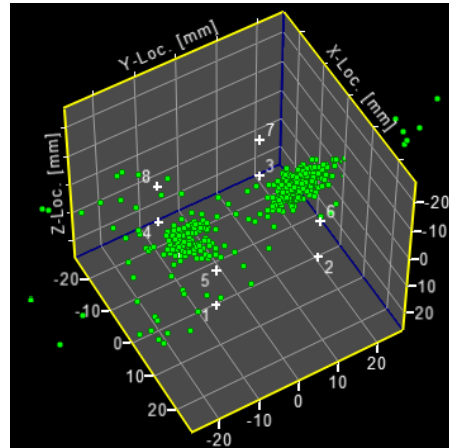
Figure 5.3.14. Acoustic emissions located for the entire duration shown in Figure 5.3.13. The locations of the two prominent AE 'clouds' correspond to the location of the tensile fractures around the analogue borehole (diameter ~1cm, located at the center [x=0mm, y=0mm], oriented in the vertical direction).
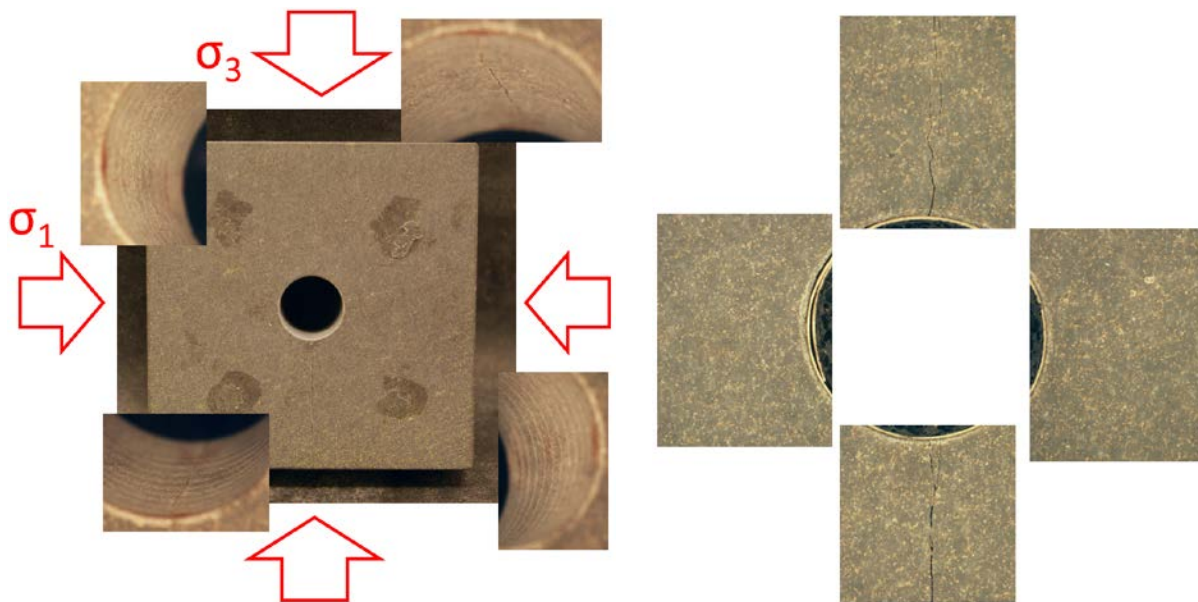
Figure 5.3.15. Post-experiment images of the slab sample and the borehole. Multiple tensile fractures are clearly visible in the maximum principal stress directions (σ_3) around the borehole. In contrast, for this experiment, no breakout was observed in the minimum principle stress directions (σ_1).

Figure 5.3.13 also presents AE frequency changes (number of AEs measured from eight sensors over 4-second intervals) corresponding to the stress history. The initial, medium-scale AE activity within 30 minutes from the start of the experiment is possibly caused by closure and slips of pre-existing, thermally-induced microcracks. Once the stress level exceeded ~50 MPa, the AE activity was almost nonexistent. Although the maximum stress on the borehole wall of 269 MPa appears to be sufficient for inducing fracturing (borehole breakout) in thermally treated novaculite based upon the results in Figure 5.3.2, the

presence of the intermediate stress (σ_z) and the curved borehole wall provide additional confinement to the rock adjacent to the borehole wall, increasing the rock strength. This strength increase becomes more evident when the minimum principal stress was reduced to near zero, and the maximum wall stress reached as high as $3\sigma_y=348$ MPa, but still with little AEs in the minimum principal stress directions around the borehole. Figure 5.3.14 shows AEs (indicated by the green dots) located within the slab sample throughout the experiment. The two prominent "clouds" correspond to the tensile fracturing which started once σ_x became smaller than 39 MPa, and the tensile stress was induced in the maximum principal stress directions. In the directions perpendicular to these features (where borehole breakout is expected), no AEs can be seen. A post-experiment examination of the slab sample (Figure 5.3.15) clearly showed tensile fractures corresponding to the locations of the observed AEs, while no breakout-related fractures were found.

5.4   Conclusion

We have developed experimental setups for examining the impact of drilling-induced damage (borehole breakout) around a deep borehole within a crystalline rock in the laboratory. Because uniform and homogeneous, ultra-fine-grain rock resulted selected for the laboratory experiment exhibited extremely high compressive strength, so far, we have not successfully induced breakout in our samples. Three possible solutions currently under consideration are (1) to reduce the rock strength further, by introducing water into the thermally induced microcracks, (2) to increase the maximum principal stress (around the borehole) by using the Z-axis loading frame in that direction, and (3) use the block sample to conduct the experiment. We will continue our borehole breakout experiment (together with other rock characterization experiments) by solving this issue, and will continue on to the planned, coupled hydrological, mechanical, and chemical experiments for investigating the seal integrity of deep boreholes.

5.5   References

Cohn, S.N. and Ahrens, T.J. 1981. Dynamic tensile strength of lunar rock types, J. Geophys. Res., 86(B3), 1794-1802.

Jaeger, J.C., Cook, N.G.W., and Zimmerman, R. 2007. *Fundamentals of Rock Mechanics*, 4th edition, Wiley-Blackwell, ISBN: 978-0-632-05759-7.

Ferreira, T., and Rasband, W.R., ImageJ User Guide, IJ1.46r, https://imagej.nih.gov/ij/docs/guide/user-guide.pdf

Finsterle, S. and Persoff, P. 1997. Determining permeability of tight rock samples using inverse modeling, Water Resources Research, **33**(8), 1803-1811.

THIS PAGE INTENTIONALLY LEFT BLANK

6.   DESIGN OF SITE CHARACTERIZATION AND MONITORING EFFORTS

6.1   Introduction

During this reporting period, research on the design of site characterization and monitoring methods and tools focused on seismic approaches for imaging and characterizing large-scale faults and fractured zones in deep crystalline rock. In the context of deep borehole waste disposal, the presence of these features is undesirable should they form high-permeability pathways for radionuclide transport to the shallow subsurface (Kuhlman et al. 2015).

Seismic methods for imaging and characterizing permeable fractures and faults are promising because of the sensitivity of seismic waves to mechanical weaknesses in rock. Fractures and faults that have sufficient connected porosity and permeability to support fluid flow and radionuclide transport represent structural weaknesses in a rock mass, and have a higher elastic compliance relative to the unfractured host rock. These features, despite their limited thickness, can give rise to a number of potentially diagnostic elastic wave phenomena, including reflections, conversions (e.g., from P-wave to S-wave) and interface waves. All of these wave phenomena can be shown to increase in magnitude with the frequency of the incident wave.

In this report, we will restrict our analysis of seismic approaches for imaging and characterizing fractures in deep crystalline rock to the boundary conditions of the Deep Borehole Field Test (DBFT) put forward by the DOE (Kotek, 2016), which excludes surface seismic and cross-well seismic approaches:

- "DOE has concluded that for the specific purposes of the DBFT, the likely value of information gained at depths of 3-5 km from surface-based techniques does not warrant the expense of surface-based geophysical investigations at the scale the NWTRB (Nuclear Waste Technical Review Board) envisions or recommends."
- "...the DBFT will include sampling and testing of formations in the crystalline basement to detect and characterize discontinuities that intersect the borehole if they are present. However, surface-based geophysics, multi-borehole studies, and extensive downhole testing to characterize larger-scale, distal discontinuities that may be present, are not planned."
- "DOE does not currently plan to use the characterization and field test boreholes to conduct cross-hole monitoring to provide information on the characteristics of the rock volume surrounding the boreholes."

Following these guidelines, we will consider only approaches where seismic sensors are located in the borehole, and at relatively close proximity (meters to 100's of meters) from the fractures and fault zones, i.e., "near-well" fracture detection and characterization. We consider two cases where the seismic source is located either on the surface, as in VSP (vertical seismic profiling) acquisition, or inside the borehole, as in single-well imaging. We use "fracture" as a general term for a plane of mechanical weakness and enhanced permeability which is taken to include permeable fault zones in crystalline rock. We review the main parameters that influence fracture imaging for these two acquisition geometries, and conclude these subsections by summarizing the current state of these technologies, as reported in the literature. Finally, we describe a new approach that may have potential for detecting and characterizing near-borehole fractures and faults. The approach, *near-field dynamic strain sensing*, seeks to probe the anisotropic properties of fractures and faults out to distances of meters to 10's of meters from a borehole. We outline the basic concept, and describe the first steps that were taken during this reporting period to build the computational framework for this approach for fractured rock characterization.

6.2   Near-Wellbore Detection & Characterization of Fractures and Faults

6.2.1   Geophysical Signatures & Sensitivity to Discrete Fractures

Over the last two decades, seismic methods have been used increasingly to estimate fracture orientation and density (e.g., for reviews, see Tsvankin & Lynn, 1999 and MacBeth & Lynn, 2000). These methods typically assume that the fracture spacing is small relative to the seismic wavelength, and employ effective medium theories to compute the (zero frequency) equivalent anisotropic properties of the fractured rock mass. Surface seismic methods for characterization of fractured rock utilize the predictions from these equivalent anisotropic models (e.g., non-hyperbolic normal moveout, split shear waves, direction-dependent amplitude versus azimuth) to obtain bulk estimates of fracture density and orientation in a reservoir with aligned fractures. Seismic acquisition methods that utilize borehole receivers are advantageous because of their proximity to the fractures and the ability to record higher frequency waves. These two factors have opened the possibility for imaging discrete fractures using VSP, cross-well, and single-well acquisition geometries (Meadows & Winterstein, 1994; Majer et al. 1997; Coates et al. 1998; Cosma et al. 2001; Place et al. 2011).

The necessary conditions for imaging of discrete fractures and fault zones are that the fracture or fault zone is: (1) sufficiently compliant to produce measurable converted waves or changes in the amplitude and phase of the transmitted wave, (2) of length greater than one quarter of the seismic wavelength (or equivalently, $kL > 1.5$, where $k = 2\pi/\lambda$ is the wavenumber, λ is the wavelength, and L is the fracture length), and (3) that the source and receiver are suitably oriented in relation to the fracture normal direction to allow transmitted or reflected waves to be recorded. These three conditions are illustrated in the numerical simulation shown in Figure 6.2.1.
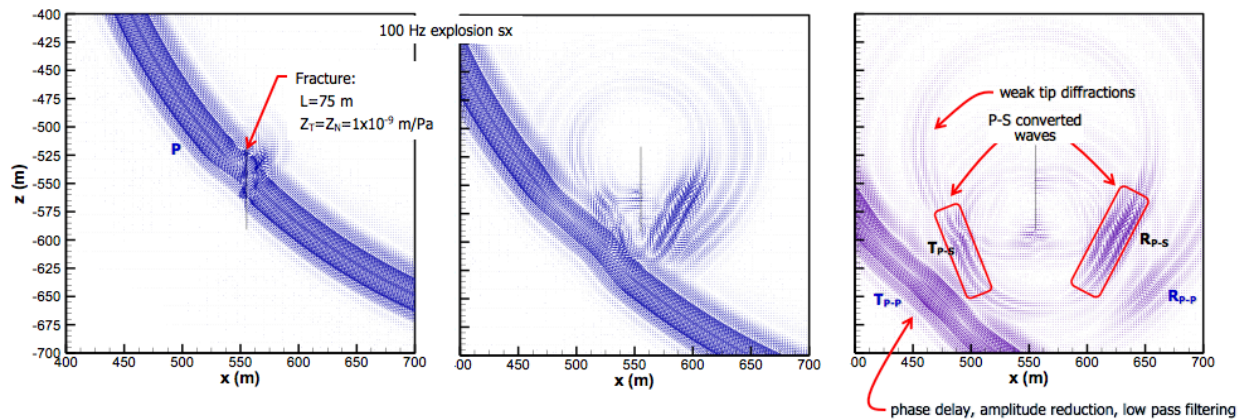
Figure 6.2.1. Elastic finite difference simulations of a single vertical fracture embedded in rock at three time steps. The figures display the particle velocity vectors for an incident P-wave and the various P- and S-waves generated by the fracture. The fracture is modeled as a thin compliant interface following the constitutive *linear slip* fracture model of Schoenberg (1980) and the equivalent medium modeling approach of Coates & Schoenberg (1995) and Schoenberg & Sayers (1995).

For a source located in the upper right hand corner and a single vertical fracture with fracture normal and shear compliances representative of a poorly-mated, dry fracture approximately two wavelengths in height (i.e., $kL = 13$), an incident P-wave interacts with the fracture to produce a number of potentially diagnostic wave phenomena. As labeled in the right subfigure in Figure 6.2.1, these include a transmitted P-wave (T_{P-P}) with a slight time delay and amplitude loss, a reflected P wave (R_{P-P}), P-S converted transmitted and reflected waves (T_{P-S} and R_{P-S}, respectively), fracture tip diffractions (circular wavefronts emerging from the two fracture tips), and a fracture interface wave (focused wave energy traveling along

the fracture). It should be noted all of these fracture-related wave effects are sensitive to the product of the fracture compliance and the wave frequency, with the magnitude of these effects increasing as this product increases. Haugen & Schoenberg (2000) capture this dependence in a parameter they labelled the "fracture equivalent thickness", $h_{eq} = Z / S$, where Z is the fracture compliance and S is the host rock compliance. Similar to the non-dimensional parameter kL that describes the impact of fracture length, kh_{eq} is the non-dimensional parameter that prescribes when the fracture equivalent thickness is on the order of the seismic wavelength, and the seismic wave of that particular frequency will start to be affected by the fracture. This dependence can be computed for incident P-plane wave using the boundary conditions on displacement and stress for the linear slip fracture model (Schoenberg 1980), as shown in Figure 6.2.2 (Gu et al. 1996; Nihei et al. 2001).
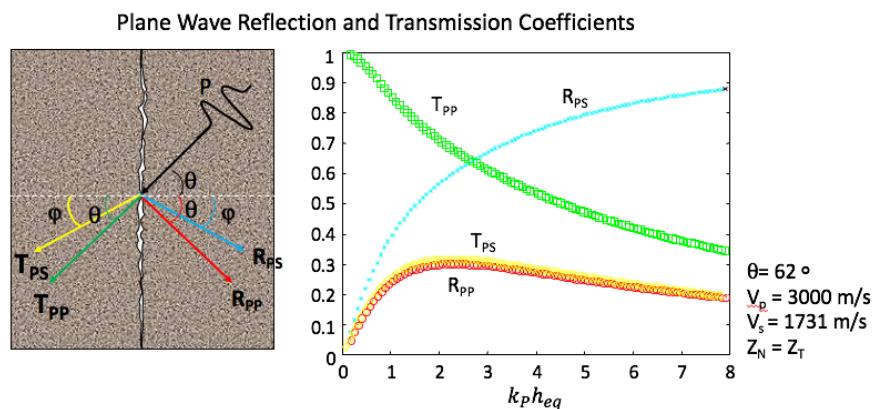
Figure 6.2.2. Plane wave transmission and reflection of an incident P-wave from a single vertical fracture (assumed infinite in length). (left) Illustration of the incident, transmitted, and reflected waves. (right) Plane wave transmission and reflection coefficients as a function of the (non-dimensional) product of the P-wave wavenumber k_P and fracture equivalent thickness h_{eq}.

A VSP with receivers in a vertical borehole located to the left of the fracture has the potential to record the converted transmitted P-S wave (T_{P-S}), which would be absent without the fracture. A VSP with receivers in a vertical borehole located to right of the fracture will record the reflected P-P wave (R_{P-P}) and reflected P-S wave (R_{P-S}), which also would be absent without the fracture. The latter configuration is also relevant for the single-well imaging geometry, where both source and receiver are located in the same borehole and only reflected waves from vertical fractures can be recorded.

The transmitted and reflected waves that develop as a result of interactions of the incident wave with a planar fracture are postulated to be well-described by the rules of geometrical optics and plane wave theory. This postulate is based on the lack of evidence that fractures have sufficient heterogeneity in their compliances or surface topography to generate non-specular waves (i.e., diffracted waves). An exception would be the diffracted waves generated at the tips of the fractures. However, it is presently unclear what the mechanical properties near the fracture edges are, and if they present strong sources of diffracted waves. If we limit our attention to specular waves, then a requirement for recording fracture generated transmitted and reflected waves (assuming an approximately constant velocity medium) is that the line formed by connecting the source and receiver and the fracture normal vector intersect to form a plane that contains the waves arrivals. This condition ensures that the specular transmitted or reflected wave will arrive at the receiver.

This geometrical optics argument for fracture imaging with VSP and single-well acquisition geometries are illustrated schematically in Figure 6.2.3. The main takeaway from this analysis is the recognition that VSP fracture imaging can image only those fractures that are optimally-oriented with respect to the

source and receiver. Expanding this analysis to include multiple sources and receivers will improve the imaging potential. While the locations of the receivers are constrained to the borehole, diversity in the source location can potentially improve the ability of VSP to image fractures. Because single-well imaging sources are constrained to the borehole, diversity on source location is more limited. In this analysis we have focused only on reflected waves, but similar arguments can be used to analyze the transmitted waves. This simplified analysis has assumed a constant velocity. In practice a spatially varying velocity will modify the conditions for fracture imaging, but the basic concept will be similar. For the next reporting period, we will develop a wave-based (rather than geometrical optics-based) approach for directly imaging fractures for general acquisition geometries, and for all transmitted and reflected wave types, including converted waves.
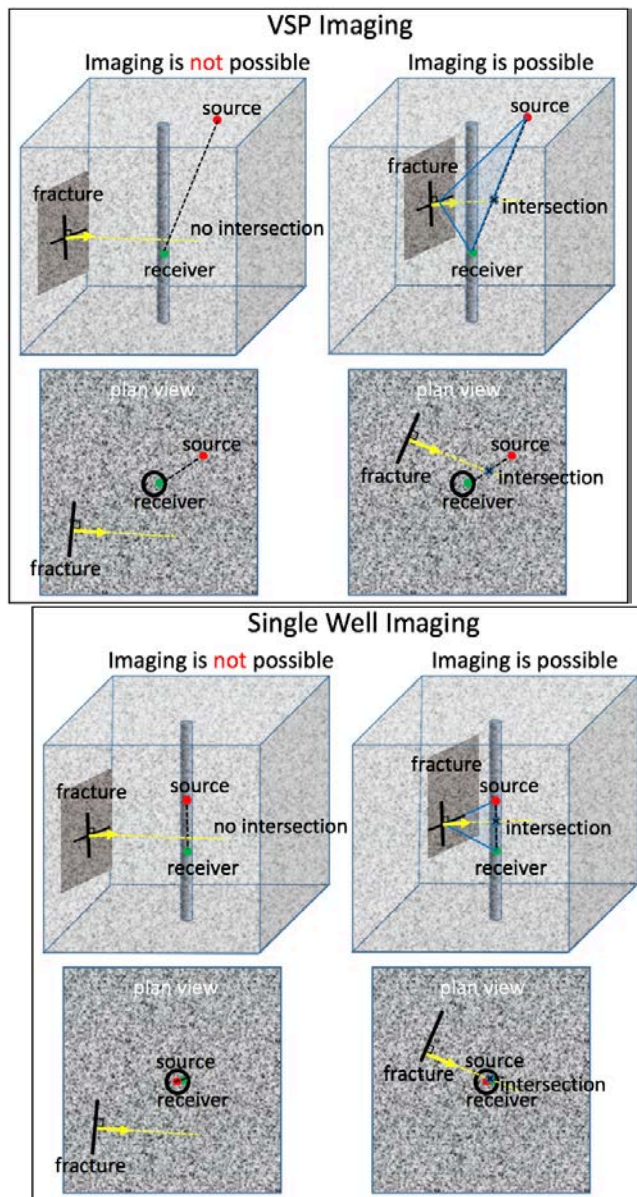
Figure 6.2.3. Geometrical conditions for fracture imaging for VSP (left) and single-well (right) acquisition geometries assuming a rock mass with a uniform velocity.

6.2.2   Near-Field Dynamic Strain Sensing

As discussed in the previous subsection, the ability of borehole seismic methods for performing discrete fracture imaging is controlled by the geometry of the source-fracture-receiver system. It would be desirable to have a borehole-based method for characterizing fractures located meters to 10's of meters from the borehole that does not suffer from this restriction.

Here, we describe a new approach for estimating the elastic properties of the volume of rock surrounding the borehole using the source energy generated in the *near-field*. The near-field refers the region around the source, typically no more than one wavelength, where *evanescent* waves are present. Evanescent waves decay rapidly away from the source. The classic point source solution for an infinite elastic medium contains an evanescent wave term that decays as $1/r^2$ away from the source, as compared to the $1/r$ decay of the P- and S-waves that propagate into the far-field (Aki & Richards 1980). The principal advantage of performing measurements in the near-field of the source is the possibility of using the evanescent waves to achieve resolution that is significantly higher than that for propagating waves (resolution limit is $\lambda/2$ for propagating waves) as a result of the increased localization of the elastic energy in this region. In the field of nano-optics, near-field imaging has been utilized to achieve super-resolution in optical imaging (Novotny & Hecht 2012). In geophysics, there have been only a limited number of attempts to perform near-field imaging. The recent work by Schuster et al. (2012) is particularly noteworthy, where $\lambda/19$ spatial resolution was achieved in imaging inclusions near a tunnel face using 60 receivers and a hammer source.

The basic concept under investigation seeks to characterize the fractured rock mass surrounding the borehole with seismic waves of frequency 50 Hz to 1000 Hz. Assuming a P-wave velocity of crystalline rock of 5000 m/s, the near-field region would extend from about 5 m out to 100 m from the borehole for this frequency range. Rather than carrying out classical reflection fracture imaging that would be limited by the geometrical considerations described in the previous subsection, we would like to perform a volumetric measurement that provides the anisotropic elastic properties of the near-field. To achieve this, we are developing an inversion framework analogous to full waveform inversion (Tarantola 1984; Virieux & Operto 2009), but adapted to more complex sources and receivers. In particular, we would like to use a family of sources that produces particle motions that isolate individual elastic constants or distinct combinations of elastic constants (Figure 6.2.4), and record the resulting deformation with multiple three-component sensors located along the borehole circumference.

^Acoustic sources. Three types of acoustic sources are used in well logging: monopole (*top*), dipole (*center*) and quadrupole (*bottom*). Monopole sources generate sound waves that radiate from the tool and travel through the formation as compressional waves. Dipole sources generate directional flexural waves. Cross-dipole sources emit two flexural waves that are oriented 90° apart. Quadrupole sources generate complex waveforms that are frequency dependent. At very low frequencies, they travel at velocities that approximate the velocity of shear waves. The blue stars represent the approximate location along the borehole of the wave represented in the cross section.

Figure 6.2.4. Deformation in the rock surrounding a borehole generated by 3 types of acoustic multipole sources: monopole source (top), dipole sources (middle), and quadrapole source (bottom) (from Alford et al. 2012). Note that the top source excites volumetric deformation, and the bottom source pure shear deformation.

Our efforts are in developing the forward modeling and inversion code base that we can use to test and further develop this near-field approach for fracture characterization from a borehole. This code base presently utilizes high-order time and space accurate, anisotropic, viscoelastic FDTD (finite difference time domain) forward modeling and an adjoint state nonlinear conjugate gradient inversion scheme. Because we would like to accurately model borehole guided waves and the deformation of the cylindrical borehole walls, we are using polar-cylindrical coordinates. Progress on these efforts will be reported in a future report.

6.3   Conclusions

In this report, we have outlined the foundation, including strengths and potential limitations, for imaging discrete fractures using borehole seismic methods. We are in the process of developing a computational framework for discrete fracture imaging which including forward modeling, imaging, and analysis capabilities for general borehole acquisition geometries, including VSP and single-well. The goal is to use these tools to determine the feasibility and performance of state-of-the-art borehole discrete fracture imaging technologies. We have also described a new approach that may hold promise for characterizing fractures that will use near-field measurements to probe a rock mass for fractures located meters to 10's of meters from the borehole.

6.4   References

Aki, K. and Richards, P.G. 1980. *Quantitative Seismology*, Volume I, Freeman, San Francisco.

Alford, J., Blyth, M., Tollefson, E., Crowe, J., Loreto, J., Mohammed, S., Pistre, V. and Rodriguez-Herrera, A. 2012. Sonic logging while drilling – Shear answers, *Schlumberger Oilfield Review*, 24:1-15.

Coates, R.T. and Schoenberg, M 1995. Finite-difference modeling of faults and fractures, *Geophys.*, 60:1514-1526.

Coates, R., Kane, M., Chang, C., Hoyle, D., Watanabe, S., Dodds, K., Esmersoy, C. and Foreman, J. 1998. Localized maps of the subsurface, *Schlumberger Oilfield Review,* 10:56-66.

Cosma, C., Heikkinen, P., Keskinen, J., and Enescu, N. 2001. VSP in crystalline rocks – from downhole velocity profiling to 3-D fracture mapping, *Int. J. Rock Mech. & Min. Sci.*, 38:843-850.

Gu, B.L., Suarez-Rivera, R., Nihei, K.T., and Myer, L.R. 1996. Incidence of plane waves upon a fracture, *J. Geophys. Res.*, 101:25337-25346.

Haugen, G.U. and Schoenberg, M.A. 2000. The echo of a fault or fracture, *Geophys.,* 65:176-189.

Kotek, J.F. 2016. DOE's Summarized Response to the NWTRB Report on the DOE Deep Borehole Disposal Research and Development Program, *Letter to U.S. Nuclear Waste Technical Review Board*, June 9, 2016.

Kuhlman, K.L., Arnold, B.W., Brady, P.V., Sassani, D.C., Freeze, G.A., and Hardin, E.L., 2015. Site characterization for a deep borehole field test, *IHLRWM*, Charleston, 624-631.

MacBeth, C. and Lynn, H.B., 2000. Fracture-related reflectivity, in *Applied Seismic Anisotropy: Theory, Background, and Field Studies*, Soc. Expl. Geophys*.,* Geophysics Reprint Series No. 20:233-235.

Majer, E.L., Peterson, J.E., Daley, T.M., Kaelin, B., Myer, L., Queen, J., D'Onfro, P. and Rizer, W. 1997. Fracture detection using crosswell and singlewell surveys, *Geophys.,* 62:495-504.

Meadows, M.A. and Winterstein, D.F., 1994. Seismic detection of a hydraulic fracture from shear-wave VSP data at Lost Hills, California, *Geophys.*, 59:11-26.

Nihei, K.T., Nakagawa, S., and Myer, L.R., 2001. Fracture imaging with converted elastic waves, *Proc. 38th US Rock Mechanics Symposium*, Elsworth, Tinucci & Heasley (eds), Balkema, July 2001, 1305-1311.

Novotny, L. and Hecht, B. 2012. *Principles of Nano-Optics*, Cambridge University Press, Cambridge.

Place, J., Sausse, J., Marthelot, J.-M., Diraison, M., Geraud, Y. and Naville, C., 2011. 3-D mapping of permeable structures affecting deep granite basement using isotropic 3C VSP data, *Geophys. J. Int.*, 186:245-263.

Schoenberg, M. 1980. Elastic wave behavior across linear slip interfaces, *J. Acoust. Soc. Am.*, 68:1516-1521.

Schoenberg, M. and Sayers, C.M., 1995. Seismic anisotropy of fractured rock, *Geophys.,* 60:204-211.

Schuster, G.T., Hanafy, S. & Huang, Y. 2012. Theory and feasibility tests for a scanning tunnelling macroscope, *Geophys. J. Int.*, 190:1593-1606.

Tarantola, A. 1984. Inversion of seismic reflection data in the acoustic approximation, *Geophys.*, 49:1259–1266.

Tsvankin, I. and Lynn, H.B. 1999. Special section on azimuthal dependence of P-wave seismic signatures – Introduction, *Geophys.*, 64:1139-1142.

Virieux, J. and Operto, S., 2009. An overview of full-waveform inversion in exploration geophysics, *Geophys.*, 74:WCC127-WCC152.

THIS PAGE INTENTIONALLY LEFT BLANK

7. SUMMARY

During FY16, LBNL scientists conducted a number of research studies to support the UFD Deep Borehole Field Test effort. This work consists of five main tasks: (1) providing support for the LANL geologic framework model for the proposed deep borehole site; (2) conducting an analog study using an extensive suite of geoscience data and samples from a deep (2.5 km) research borehole in Sweden; (3) conducting coupled process modeling related to borehole damage zones and seals; (4) designing and carrying out laboratory experiments related to borehole seals and; (5) developing a suite of potential techniques that could be applied to the characterization and monitoring of the deep borehole environment.

FY16 efforts related to supporting the LANL geologic framework model were limited, as the characterization borehole site was not finalized. Our team did collect relevant subsurface geoscience data for the initial proposed site near Rugby, ND, and is prepared to provide similar assistance to LANL in FY17 once a new drill site is selected and approved.

We developed an extremely productive collaboration with members of the science team of the "Collisional Orogeny in the Scandinavian Caledonides" (COSC) project, which drilled and characterized a 2.5 km scientific borehole (COSC-1) in central Sweden, to obtain key insights on deep borehole characterization techniques. The COSC project provides an excellent opportunity for the DOE Deep Borehole Field Test project to glean key insights regarding the characterization of basement rocks intersected by a deep borehole through geophysical surveys and downhole logging, lithologic descriptions of core, and structural studies (deformation, stress measurements, fracture orientations). During FY16, our team conducted and analyzed the results of FFEC logging, which identified eight hydraulically conductive zones, each associated with open fractures in the associated core, and performed numerical modeling and laboratory experiments to characterize the transmissivity and salinity of these fluid entry zones. We worked with the COSC researchers to obtain a suite of downhole water samples collected using two different techniques, looking at variations in fluid chemistry and associated microbial communities with depth. Follow-up work in FY17 could include examining borehole breakout data, downhole seismic logs and core lithology and XRF chemistry data (all of which have been collected by the COSC science team), and see how these correlate with the observed permeable fracture zones and variations in fluid chemistry. If possible, fluid sampling using a downhole packer assembly would permit better characterization of the inflow water from the discrete fracture zones that were identified.

Another important component of the LBNL deep borehole field test research was coupled process modeling associated with borehole damage zones and seals. This work reviewed field observations on stress and permeability at depth and observations of damaged and disturbed zone around existing tunnels and boreholes. Our team also performed initial thermal-hydrological (TH) modeling of deep borehole disposal focusing on thermally driven fluid pressurization and potential upflow along an assumed disturbed zone. Proposed FY17 activities include THM and THMC analysis of the deep borehole system, with a focus on the performance of seals and plugs within the borehole.

In tandem with the borehole seal modeling work, a series of laboratory experiments were designed and conducted to evaluate the impact of drilling on borehole integrity in a deep borehole environment. Our team developed experimental setups for examining the impact of drilling-induced damage (borehole breakout) around a deep borehole within a crystalline rock in the laboratory. An ultra-fine-grain rock (novaculite), which has uniform and homogeneous properties, was selected for the laboratory experiments. This rock exhibited extremely high compressive strength; as a result, we were not successful in inducing breakout in our samples thus far, even after thermal weakening of the samples. Our team has proposed three follow-up experiments for FY17 based on the FY16 results: (1) reducing the rock strength further by introducing water into the thermally induced microcracks, (2) increasing the maximum

principal stress (around the borehole) by using the Z-axis loading frame in that direction, and (3) using a block sample to conduct the experiment.

Our final activity in FY16 in support of the Deep Borehole Field Test involved designing a suite of characterization and modeling techniques for the deep borehole environment. This task focused on the near-well geophysical detection and characterization of fractures using a variety of techniques, including vertical seismic profiling (VSP), single well seismic imaging, and near-field strain sensing. Another approach that will be developed in FY17 is the LBNL deep borehole multilevel characterization system, which would include fluid flow testing, *in situ* pressure and temperature measurements, integrated fiber optics for VSP and DTS measurements, and a U-tube fluid sampler for tracer testing and geochemical sampling. Continued work in FY17 on techniques used to detect and characterize fractures in the near-wellbore environment will involve evaluating these methods using synthetic and analog datasets.

8. ACKNOWLEDGMENTS

THIS PAGE INTENTIONALLY LEFT BLANK

Appendix A

A Summary of an Informal COSC-1 Workshop at LBNL

December 17, 2015

Pat Dobson, LBNL

Chris Juhlin, Uppsala University

January, 2016

A-1 A Summary of an Informal COSC-1 Workshop at LBNL

Taking advantage of the gathering of geoscientists at the AGU meeting in San Francisco in December 2015, an informal workshop on scientific work being done with the COSC-1 data and cores was held at the Lawrence Berkeley National Laboratory (LBNL). Besides reports from COSC-1 scientists from Sweden, Germany, Switzerland and Canada, LBNL scientists also presented their work on COSC-1 core measurements, water sample chemical and microbiological analyses, and numerical and analytical analysis of flowing fluid electric conductivity logs.

Below are the agenda and attendance list of the Workshop, followed by brief summaries and lessons learned for each talk. Each of these presentations can be found on the COSC Google Drive folder. Please contact the authors if there are any questions or suggestions (pfdobson@lbl.gov or christopher.juhlin@geo.uu.se).

Agenda – Collisional Orogeny in the Scandinavian Caledonides (COSC) Workshop

Date: December 17, 2015 10:00 am – 3:30 pm
Location: Lawrence Berkeley National Laboratory, Building 74, Room 104

Attendees:
Chin-Fu Tsang (Uppsala University/LBNL)
Patrick Dobson (LBNL)
Chris Juhlin (Uppsala University)
Christophe Pascal (Ruhr-University Bochum)
Bjarne Almqvist (Uppsala University)
María García Juanatey (Uppsala University)
Wenning Quinn (ETH)
Yvette Piceno (LBNL)
Gary Andersen (LBNL)
Sharon Borglin (LBNL)
Christine Doughty (LBNL)
Doug Schmitt (U. Alberta)
Jens Birkholzer (LBNL)

Schedule

10:00 – 10:10	Welcome by Jens Birkholzer (with coffee and snacks)
10:10 – 10:40	Chris Juhlin – Overview of the COSC-1 Project
10:40 – 10:55	Pat Dobson – Role of COSC-1 studies in DOE Deep Borehole Program
10:55 – 11:15	Chin-Fu Tsang – FFEC logging and water sampling at COSC-1
11:15 – 11:30	Christine Doughty – Initial modeling analysis of FFEC results
11:30 – 11:45	Christophe Pascal – COSC-1 geothermal research, present status
11:45 – 12:00	Wenning Quinn – Borehole stress measurements and fractures in COSC-1
12:00 – 1:00	Lunch break (lunch served in meeting room)
1:00 – 1:15	Sharon Borglin – Fracture flow in permeable cores – experimental design and testing
1:15 – 1:30	Bjarne Almqvist – Structural geology of the COSC-1 setting
1:30 – 1:45	Pat Dobson – Variations in water chemistry from COSC-1
1:45 – 2:00	Yvette Piceno – Bacterial community profiling of COSC-1 water samples: A preliminary assessment
2:00 – 2:15	María García Juanatey – MT studies on COSC-1
2:15 – 2:30	Doug Schmitt – Stress and anisotropy at COSC -1
2:30 – 3:30	Open discussion and ideas for future cooperation

Photo of some of the participants of the informal COSC workshop in Berkeley, next to the Advanced Light Source facility, Lawrence Berkeley National Laboratory.

BRIEF SUMMARIES OF PRESENTATIONS

1. Jens Birkolzer – Subsurface energy resources R&D at LBNL

Jens gave a brief overview of Lawrence Berkeley Lab, its user facilities, and the research that is conducted by the Earth and Environmental Sciences Area. This group has about 450 staff members in 5 departments (geochemistry, geophysics, hydrogeology, ecology, and climate), and has a mission to create new knowledge and capabilities needed to sustain stewardship of critical environmental systems and judicious use of the Earth's subsurface energy resources.

2. Chris Juhlin – Overview of the COSC Project: Exploration of the Caledonian Mountain Belt in Scandinavia by deep drilling.

The motivation of this project is to gain insights into the tectonic evolution of the area, present and past deep fluid circulation patterns, current heat flow and climate modeling, the deep biosphere. Another objective of this project is to calibrate high quality surface geophysics through deep drilling. The COSC-1 borehole was drilled though the Seve Nappe, which contains high grade metamorphic rocks (mostly felsic gneisses) indicative of deep (100 km) crustal levels. HQ core was collected from 102 m to 1616 m, and NQ core was obtained from 1616 m to the bottom hole depth of 2496 m; core recovery was excellent. Extensive core and borehole geophysical studies have been combined with surface geophysical measurements to better understand the thermotectonic history of this nappe. The main objective of the proposed COSC-2 borehole is to penetrate the décollement and characterize the deformation history of the basement.

3. Pat Dobson – Role of COSC-1 studies in DOE Deep Borehole

The DOE Deep Borehole Disposal concept involves the disposal of waste canisters within a deep (5 km) borehole drilled into crystalline basement rocks. These rocks typically have low permeability and are hydrologically isolated from overlying aquifers. Borehole seals would be engineered to maintain a barrier over the period of thermally-induced upward flow. Technical siting guidelines include: a) Less than 2 km depth to crystalline basement; b) Not near urban areas or known natural resources; c) Geothermal heat flux less than 75 mW/m^2; d) Away from seismic and volcanic hazards; e) No known major crystalline basement shear zones or major tectonic features; f) Hydraulic isolation of deep crystalline zone.

DOE is in the process of selecting a site for a field test of this disposal concept. The initial 5 km deep characterization hole would be drilled with a bottom hole diameter of 8.5 inches, and will be used to test the ability to drill deep, wide and straight in crystalline rocks, characterize bedrock via geophysics, conduct in situ tests (such as flow and tracer tests) in basement, and obtain geochemical profiles. If the first borehole is successful, then a second larger-diameter (17 inch) borehole would be drilled to the same depth to test emplacing and retrieving test waste packages. Possible insights from the COSC project include characterization of basement rocks through geophysical surveys and downhole logging, lithologic descriptions of core, structural studies (deformation, stress measurements, fracture orientations), and hydrologic characterization of this environment through flowing fracture identification and modeling, fluid chemistry variations with depth, and microbial community characterization.

4. Chin-Fu Tsang – FFEC logging and water sampling at COSC-1

Flowing Fluid Electric Conductivity (FFEC) logging was conducted in 2014 during and shortly following drilling, and again in 2015. For the initial suite of tests, these logging runs took advantage of the day off

from drilling to flush the well, then run an electrical conductivity tool in the well to detect inflow zones that had contrasts in fluid salinity from the wellbore fluid. The 2014 tests ranged in duration from 8 hours to a day, and had well drawdowns varying from 33 to 70 m. The logging runs conducted in 2015 had encountered some difficulties in replacing the wellbore fluid, so the borehole background FEC remained high. Two pumping rates resulted in different drawdowns; the first was – 50 m (3 logs taken), and the second had -10 m drawdown (10 logs taken). The low drawdown from the second test resulted in minimal fracture fluid flow, as most of the fractures have negative head. From these logs, the depth of hydraulically active fractures can be determined, as well as their transmissivity, fluid salinity, and initial pressure head. Core samples with fractures have been identified for each of these flow zones, and have been sent to LBNL for laboratory studies and analyses. Only a few percent of all of the fractures detected in the borehole are conductive.

Two sets of downhole water samples were collected in 2015 – one using the tube sampling method (GTK), and the other using a conventional downhole sampler (Lund). These waters, collected at depths corresponding with the inflow zones identified by the FFEC logging, are being studied for their chemical and microbiological compositions.

5. Christine Doughty – Initial modeling analysis of FFEC results

The FFEC logging during drilling tests Lund 1 and Lund 2 produced key information about the hydraulically conductive features intercepting COSC-1 borehole between 250 m and 2000 m depth. Seven hydraulically conductive zones were identified, each localized over a small depth zone, suggesting that they are individual fractures. All the inferred fracture properties determined from modeling – flow rate, salinity, transmissivity, and hydraulic head – varied greatly among the fractures, as is typical of a poorly connected fracture network in low-permeability rock. Salinity values are relatively low and hydraulic head variability suggests downward groundwater flow; both features are consistent with the mountainous setting of the COSC-1 borehole.

Several important lessons were obtained from the FFEC logs and modeling work. Most of the fluid entries identified in COSC-1 had negative hydraulic head, which meant that these fractures would only flow into the wellbore if there was sufficient drawdown in the well. Drawdown cannot exceed the casing depth (100 m), so it cannot be increased significantly, so the flow rate from the fractures cannot be increased, but potentially the duration of logging could be lengthened. Under optimal operational conditions, it should be possible to collect four or five profiles within a 24-hour period. Also, washing out the borehole prior to FFEC logging is not as well-controlled an operation as recirculation, which has two potential adverse consequences. First, the borehole fluid may enter the flow zones during washing out; it returns to the borehole during logging while pumping, thus early-time logs will not represent formation fluid compositions. Second, the baseline profile will not reflect internal flow in the borehole under non-pumped conditions. Another limitation is that with the small inflow rates, peaks in the FFEC logs will be small and symmetric, exhibiting little or no peak skewing up the borehole in the short time available for logging. This means that it will be difficult to determine inflow rate q and flow zone salinity C for each peak independently. Our overall conclusion is that with careful planning and thoughtful execution, useful information can be obtained from FFEC logging, even when logging is conducted during drilling.

6. Christophe Pascal – COSC-1 geothermal research, present

The primary objectives of the geothermics research at COSC are: a) to contribute to basic knowledge about the thermal regime of Palaeozoic orogenic belts, ancient shield areas and highly heat-producing plutons; b) to refine knowledge on climate change at high latitudes (i.e. Scandinavia), including historical global changes, recent palaeoclimate development (since the last ice age) and expected future trends; c) to

determine the vertical variation of the geothermal gradient, heat flow and thermal properties down to 2.5 km, and to determine the required corrections for shallow (< 1 km) heat flow data; d) to explore the geothermal potential of the Åre-Järpen area; e) to explore to what degree the conductive heat transfer is affected by groundwater flow-driven advective heat transfer in the uppermost crust; f) to evaluate the heat generation input and impact from the basement and the Alum shales. These goals are achieved through making repeated T-log measurements to determine pristine (equilibrated) gradients, measuring rock thermal properties on core material, determining the amount of heat generated by natural radioactivity, calculating heat flow profiles from the ground surface down to TD and correcting them from eventual perturbations, isolating transient thermal signals and modeling their respective causes (i.e. fluid flow, paleoclimatic changes), and constructing 3D thermal models of the areas. The overall temperature profile exhibits a gradient of 20°C/km, with a bottom hole temperature of ~ 55°C. Shallow temperature gradients reflect changes in the long-term surface temperature associated with climate change, thus recording transient heat flow signals. 105 core samples from COSC-1 have been analyzed for thermal conductivity, thermal diffusivity, density, seismic velocity, radioactive element contents, porosity, and permeability.

7. Quinn Wenning – Stress field reconstruction in high-grade metamorphic rocks of Central Scandinavia

While the North Sea has many stress indicators (from the many oil wells in the region, continental Scandinavia has relatively few measurements, and COSC-1 provides the opportunity to study stresses in a deep borehole in a poorly characterized region. The orientation of in situ horizontal stress components can be determined from borehole breakouts, which are oriented perpendicular to S_{Hmax}. Seven distinct breakout zones were identified in the COSC-1 well (which was logged down to ~1600 m), defining an S_{Hmax} orientation of 123° ±16°. Hydraulically conductive fractures below 750 m are oriented along S_{Hmax}, indicating they formed under current stress conditions (shallower flowing fractures appear to have much more scattered orientations). Seismic velocity measurements indicate that the core has high rock strength, explaining why so few breakouts were observed. Additional logging is planned to image the lower part of the wellbore.

8. Sharon Borglin – Fracture flow in permeable cores

Sharon gave us a tour of the LBNL rock laboratory to examine the fractured COSC-1 core intervals and the laboratory apparatus under construction to measure fracture permeability in multiple orientations.

9. Pat Dobson – Variations in water chemistry from COSC-1

Two types of downhole sampling were conducted at COSC-1 in 2015: "tube" sampling of 100 m depth intervals for entire borehole using a 10 mm ID tube, and conventional downhole sampling at 6 depths. Water sampling was conducted prior to and after the FFEC logging. Preliminary water chemistry data are courtesy of Lasse Ahonen and Riikka Kietäväinen (GTK). For the tube samples, the tube was lowered down the borehole, and then the bottom was closed. The tube was progressively raised to the surface, and 100 m long sections were clamped off (eight 6 m long subsections were collected for the microbial studies). Gas samples were extracted from the tubing segments, and water samples were then drained to sampling bottles for analysis. Both electrical conductivity and pH were measured on site. Tube water samples analyzed by GTK, and downhole water samples analyzed by LBNL and UC Berkeley. Very good agreement was seen between the different sampling methods and analytical laboratories. There is a significant shift in water chemistry trends at ~1200-1300 m depth, corresponding to two of the main conductive fracture zones (1210 & 1250 m) and the microkarst zone observed between 1200 − 1320 m. The waters are generally calcium-sulfate-bicarbonate in composition. The bottommost samples (2350, 2426 m) have higher TDS than all other samples – these were collected near the two deepest fracture flow

zones and a change in lithology. There is a trend towards higher δD and $\delta^{18}O$ values for waters sampled from the deeper portion of the well. Interestingly, the deep water compositions are similar to surface water isotopic compositions. It would be helpful to characterize the water chemistry and stable isotopic composition of the water used during drilling operations and in flushing the wellbore prior to the FFEC logging runs to see if this water constitutes a significant component of the water that was sampled from the well.

10. Yvette Piceno – Bacterial community profiling of COSC-1 water samples: A preliminary assessment

Microbial communities were profiled using a high-density DNA microarray (PhyloChip G3) and iTag sequencing methods to determine if the analyses could differentiate flow zones within the borehole. Both analyses resulted in the delineation of upper and lower zones, and additional structure within the lower zone was discernable in both data sets and statistically supported in the PhyloChip data. Both data sets also revealed trends in organism abundance consistent with geochemical parameters measured (e.g., sulfate-reducing bacteria) and indicated numerous bacteria likely responsive to the thermal gradient through the 2.5 km deep borehole.

The sampling methodology appeared to have a large influence on the vertical profiles, primarily due to sediment load in the bottle-collected samples compared with the tubing-collected samples. PhyloChip and iTaq sequencing results showed a clear separation of samples based on collection method, though there were other confounding factors that differed between the sample sets, so some differences could be related to borehole flushing rather than sediment load. If using inflatable packers to isolate a region of the borehole is feasible (e.g., Nyysonen et al. 2012), it would be the preferred method. Anticipating that this will not always be feasible, especially at great depth, the tubing method yielded samples that appeared representative of the variable microbial communities throughout the borehole. One potential drawback of the tube sampling is that the sample depth intervals submitted for microbial characterization were not at the exact location of the fractures, but instead at the end of the 100 m tubing section that included the fracture interval. This may result in a sample that is either diluted or is not representative of the fracture zone. In addition, the negative hydraulic head associated with most of the fracture zones may require significant lowering of the well water level to initiate inflow from these fractures into the wellbore.

Nyyssönenn, M., Bomberg, M., Kapanen, A., Nousiainen, A., Pitkänen, P., & Itävaara, M. (2012) Methanogenic and Sulphate-Reducing Microbial Communities in Deep Groundwater of Crystalline Rock Fractures in Olkiluoto, Finland, *Geomicrobiology Journal*, 29:10, 863-878.

11. María García Juanatey – MT studies on COSC-1

The Cambrian Alum shales have very low resistivity values (0.1 – 1 Ωm), making them an ideal marker for electromagnetic methods. They are found in the lower Allochthon sequence. In contrast, the gneisses and amphibolites of the Seve Nappe complex of the middle Allochthon are much more resistive units. In addition to regional MT measurements, several types of resistivity logs were run in the COSC-1 well, with different depths of penetration into the host rock. MT profiles were created from 2D inversions of the data, either with the COSC-1 borehole constraints, or without the borehole resistivity data. In addition, 1D inversions of single station data were conducted, which allow for better constraint of depths to layer interfaces; these results correlate well with the 2D inversion models.

The 2D MT profile was combined with the seismic profile through the area, indicating that Seve Nappe complex both highly resistive and reflective, the Silurian turbidites at 26 km along the profile are more resistive than the Ordovician turbidites, the Alum shales occur at shallower depths (350-1000 m depth at

L2) than originally thought, and the exact location of the detachment is not well constrained yet. Future work includes a 3D inversion of the MT data, a 2D inversion constrained using seismic data, and additional constraints using resistivity logs from the proposed COSC-2 borehole.

12. Bjarne Almqvist – Structural geology around the COSC-1 borehole

The Scandinavian Caledonides consists of a fold and thrust belt in Norway and western Sweden. The upper allochthon consists Laurentian and Iapatus terranes, the middle allochthon is comprised by a sequence of nappes with high grade gneisses, dike swarms, and mylonitic granites, while the lower allochthon consists of molasse and flysch sediments that were deposited in a foreland basin. Tectonic models of this area need to take into account episodes of thrusting, extension, and folding. One of the objectives of the COSC project is to decipher the deep crustal structure beneath the central Scandinavian Caledonides. Two locations are being considered for the COSC-2 well, whose primary objective is to penetrate the décollement into the underlying basement. Structural studies from the COSC-1 well include evaluation of foliation and fracture orientations, determination of horizontal stress orientations from borehole breakout data, and determination of quartz deformation textures.

13. Doug Schmitt – The Hunt Well: Geophysical investigations of a deep borehole in the crystalline basement

A petroleum exploration well was drilled deep into the Canadian Shield basement complex in NE Alberta to test the theory of oil generation from mantle sources. A deep seismic reflection line was acquired in 1993, and initial drilling to 1654m was completed in 1994. The Mesozoic and Paleozoic cover extends to a depth of 541.3 m. The well was deepened in 2003-2004 to 2363 m, and the upper 1000 m of the well was cased. Downhole temperature measurements were made in 2007-2008, and the Helmholtz-Alberta initiative was granted access to the well for scientific study.

These studies include an extensive suite of borehole logs, surface and VSP seismic, and detailed studies of core samples from the well. The basement rocks consist of foliated granite, which has a porosity of ~1%. Dipping reflectors identified in the basement sequence of the 2D seismic profile may be associated with fracture zones or mafic bodies. Localized fracture zones may have conductive mineral fillings. Differences in seismic velocities between VSP and sonic logs may indicate damage zones near the wellbore. Anisotropy observed in the VSP data may be due to structural or compositional layering, the presence of fractures, or the presence of foliation or anisotropic minerals. Future work opportunities include improving the seismic imaging of the crystalline basement, reprocessing the walk-away VSP data to better image dipping seismic event, perform hydraulic tests to identify potential fluid loss zones within the borehole, and evaluate the implications of low pore pressures and/or low permeability in the basement rocks.